Experimental study of single-tip optical fiber probing in dispersed gas-liquid two-phase flow and micro-processing of the optical fiber probe using the femtosecond pulse laser

静岡大学　博士論文

Experimental study of single-tip optical fiber probing in dispersed gas-liquid two-phase flow and micro-processing of the optical fiber probe using the femtosecond pulse laser

単一光ファイバープローブを用いた気液分散流計測，
ならびにフェムト秒レーザーによる
光ファイバー微細加工に関する実験的研究

2015 年 12 月
大学院　自然科学系教育部
環境・エネルギーシステム専攻
水嶋　祐基

Contents

Shizuoka University

1. Introduction

Gas–liquid two-phase flows exist in many industrial settings such as chemical and power plants, fuel injection in gasoline/diesel engines, decontamination in healthcare environments, surface cleaning processes, and hot metal cooling. Improving their performance is essential to reducing the discharge of greenhouse gases. For this specific purpose, a deep understanding of the dispersed flow is needed. In hot metal cooling processes, for instance, the flow of cooling water through a control valve is a dense dispersed spray with rapidly changing spatial and temporal characteristics. To characterize the dispersed two-phase flows, several laser-based techniques, such as Phase Doppler Anemometry (PDA)[1] and Interferometric laser imaging (ILIDS)[2, 3] have been developed to measure the bubble/droplet sizes, velocities and number density. Since the 1960s, local phase detection techniques—including electrical probes[4], hot-film/wire probes[5] and optical fiber probes (OFPs)[6]—have been rapidly developed. All conventional probes deliver ON/OFF phase-dependent signals, i.e. impedance probes detect increases/decreases in electric conductivity, hot-film/wire probes detect increases/decreases in thermal conductivity and OFPs detect increases/decreases in the refractive index. The probe developers have achieved phase detection (detecting which phase, gas or liquid, covers the tip of the probe) from two-state signals by using thresholds. Although the probe methods are intrusive forms of measurement, they enable the measurement of bubbles/droplets in flows where PDA, ILIDS and the other non-intrusive techniques cannot work well, because the incident laser beams of PDA or ILIDS

are easily interrupted by a thick bubble layer or liquid films with disordered wavy surfaces. In particular, the OFP measurement system is both simple and sophisticated for phase detection. Because of its intrusion, the OFP can successfully measure bubbles/droplets even in the case of high number density.

OFPs are used extensively in bubbly flows[7-13]. Saito and his group have reported their original OFP performance in the simultaneous measurement of size, velocity and local number density of bubbles/droplets: a Four-Tip Optical fiber Probe (F-TOP[11, 14-17]); a Two-Tip Optical fiber Probe (T-TOP[18]), a Single-Tip Optical fiber Probe with a wedge-shaped tip (S-TOP[19-22]); a femtosecond-laser-fabricated Single-Tip Optical-fiber Probe (Fs-TOP[19]) and a Photoelectric Optical Fiber Probe (POFP[18, 23]). In addition, they recently reported the simultaneous measurement of the local CO_2 concentration in the wake of a CO_2 bubble by using the bubble velocity and chord length via the POFP. Due to the simple structure and good design with deep consideration of optical characteristics, the S-TOP and the Fs-TOP are suitable for measuring sub-millimeter- or micrometer-order bubbles/droplets (the S-TOP shows satisfactory performance in measuring a bubble/droplet at a velocity of up to 15 m/s in a typical photomultiplier and water–air two-phase flows). However, the advantage of using a single tip inevitably creates a bottleneck in the form of an unknown touch position between the probe and the bubble/droplet. Since the 1980s, the problem of the unknown touch position has frequently led to controversy over probe measurements. A pierced chord length is obtained with the residence time in the bubble/droplet. The length depends on the touch position. When the probe penetrates the central region of the bubble/droplet, the chord length is measured at nearly the full length of its minor axis, and when it penetrates the outer region

of the bubble/droplet, the measured pierced chord length is shorter than its minor axis. The difference inevitably lowers the probe measurement accuracy. Although Clark and his group [24, 25] dealt with this problem by using a statistical method, a challenging uncertainty remains.

In this thesis, I confront this problem and propose a new method for detecting the touch position between the S-TOP and a bubble/droplet. Cartellier and his group [26-28] first demonstrated bubble measurements by using a mono-tip optical fiber probe equipped with an optimized sensing tip. They explored the applicability of the mono-tip optical fiber probe for measuring bubbly flows by scrutinizing the optical signals. However, optical fiber probe signals include useful and unknown potential. Hence, an analysis of the probe signal considering the dynamical and optical probe–bubble interaction is needed. I will propose a pre-signal/post-signal threshold method to detect the touch position. Such spike signals appear when the beams discharged from the wedge-shaped tip of the S-TOP in liquid are reflected at the interface and re-enter the S-TOP. The amplitude of the spike depends on the bubble/droplet orientation for the S-TOP. Consequently, using its intensity, we can discriminate where and how the S-TOP has touched the bubble/droplet. Although previous researchers noted the occurrence of such spike signals, none of them was able to extract those excellent potential for detecting the touch position/angle of the optical fiber probe, because spike signal was noisy and unpredictable. Some researchers concluded that it was impossible to control or foresee the appearances of the "spike-noise", but the S-TOP with a wedge-shaped tip can draw a highly reproducible.

In the chapter 2, the optic signal of the OFP is studied. The signal is simulated by using 3D ray tracing simulator then the properties of the spike signal is investigated. In the chapter

3 and 4, the results are confirmed in experiments then the relation between pre-signal/post-signal intensity and touch position/angle is deeply studied. On the basis of these relations, I propose the pre-signal/post-signal threshold method for correctly measuring the bubble/droplet size and velocity via the S-TOP.

The accuracy of the S-TOP measurement can be improved by above method, however, the S-TOP has a spatial limit, especially for droplet measurement, owing to its measurement principle. The Fs-TOP successfully overcomes this limit, therefore in the chapter 5, femtosecond (fs) pulse laser processing for optical fiber is studied. The Fs-TOP is developed by Saito and his group, and more optimization for processing is needed to measure fine-droplets (few dozen micrometers droplets). The fs-laser induced physics are widely studied recently, and its high performance for readily controlled processing with nonthermal effect fascinates many researchers. However, the reports about processing of the optical fiber is quite few. The fs-pulse induced bubble formation in liquid is studied in order to reveal the interaction of the fs-pulse and transparent materials. Fine-time-resolved measurement methods are well-organized and conducted for the bubble formation. As a result, the bubble formation is dominantly caused by a nonlinear effect along the optic axis of the fs-pulse. I also found that one of the dominant factors for this phenomena is type of liquid. Based on the results, fs-laser processing in different atmosphere is extensively studied in the chapter 6.

2. Basis of the single-tip optical fiber probing for bubble/droplet measurement

For any probe-techniques employed for gas-liquid two-phase flow, a two-state signal is obtained because the phase surrounds a sensing part of the tip by taking advantage of a specific phase-dependent physical phenomenon existing at this part. According to Cartellier[29], k-phase indicator Ψ_k is described as

$$\psi_k\left(x,t\right) = \begin{cases} 1 \left(\text{if } x \text{ is in phase } k \text{ at time } t\right) \\ 0 \left(\text{otherwise}\right) \end{cases} \tag{2.1}$$

where x is the position of the sensing tip of the probe (Figure 2.1).
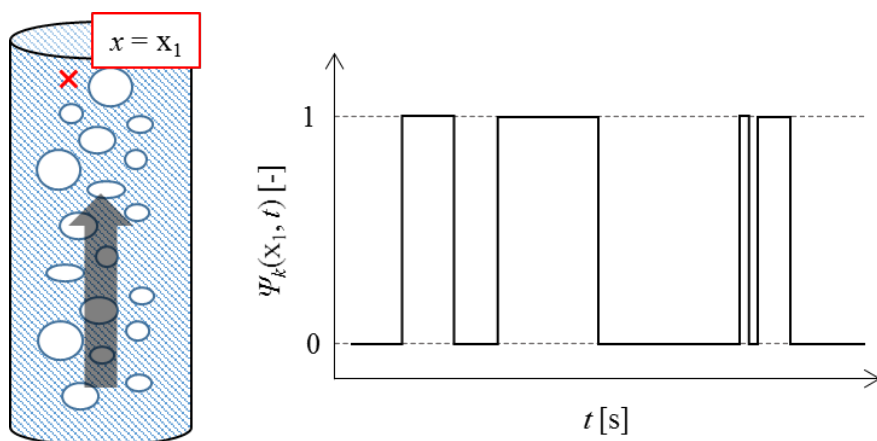
Figure 2.1: Schematic of a phase indicator Ψ of probe measurement.

The ensemble average of Ψ_k is the void fraction in a bubbly flow, and is the holdup in a droplet flow. Usually, this value is not directly relates to the signal produced by a limited number of probes; however, when the ergodic theorem is valid in the target flow, local volume fraction A_k can be calculated by the time average of Ψ_k over a "long enough" measurement time,

$$A_k(x) = \lim_{T \to \infty} \int_{t-T}^{t} \psi_k(x,t') dt' / T_{tot} = \lim_{T \to \infty} \sum_j T_{k,j} / T_{tot} \qquad (2.2)$$

where $T_{k,j}$ is the jth k-phase residence time and T_{tot} is the time during that the signal is studied. A mean velocity of the gas-liquid interface $\bar{U}_{int}$ is usually measured with a transient time τ and given distance of two probes l,

$$\bar{U}_{int} = l/\bar{\tau} \qquad (2.3)$$

If the bubbles/droplets have a constant velocity, it is possible to obtain their chord lengths, L, pierced length by the probe,

$$L = T_{k,j} \times \bar{U}_{int} \qquad (2.4)$$

As for optical fiber probe (OFP), Ψ_k is obtained by the refractive index n_k of the k-phase as the specific phase-dependent factor. In this chapter, the measurement theory of the OFP is

6

introduced, then the measurement principle of Single-Tip Optical fiber Probe (S-TOP) is discussed by experiment. At last, the S-TOP signal is analyzed through our 3D ray tracing simulation.

2.1 Theory

Classic theory   For simplicity, ideal 2D conical probe tip is assumed in order to describe how to detect phase (Figure 2.2). When the tip is positioned in a single phase, the refraction at the tip is expressed by using the Snell-Descartes law,

$$i_{crit} = \sin^{-1}\left(n_k / n_f\right) \quad \text{for} \ n_k < n_f$$
$$\left(\because \ n_f \sin i = n_k \sin r\right) \tag{2.5}$$

where n_f is the refractive index of the fiber core, i and r is the incident and refract angles of the light on the tip surface, and i_{crit} is the critical angle for total reflection.
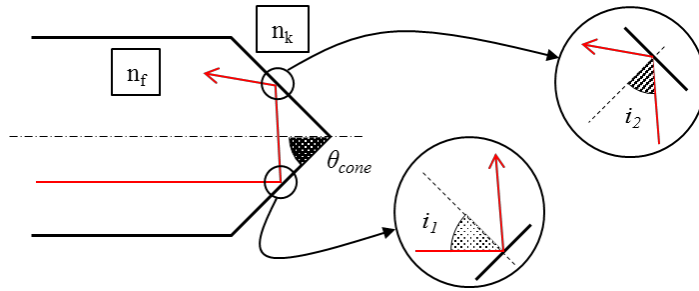
Figure 2.2: Schematic of a 2D conical probe tip. When $i_1 = \pi/2 - \theta_{cone}$ and $i_2 = 3\theta_{cone} - \pi/2$ are larger than i_{crit}, rays return to the inlet tip by total reflection, then Eq. (2.6) is obtained.

The probe tip of θ_{cone} has no clad layer, the rays in the fiber are parallel to the fiber axis, and only the total reflected rays contribute to the phase detection. In this hypothesis, optimal θ_{cone} is implied by,

$$\frac{\pi}{6} + \frac{i_{crit}}{3} < \theta_{cone} < \frac{\pi}{2} - i_{crit} \qquad (2.6)$$

This range is shown in Figure 2.3 for $n_f = 1.46$ of our optical fiber. According to this limit, most of the light are effectively reflected when the tip of $44° < \theta_{cone} < 46°$ is positioned in the medium of $1.0 < n_k < 1.02$ (air, water vapor, or other gases). The refractive index of the objective phase should be over 1.02 (intersection point of Fig. 2.3) in this condition, then the phases can be discriminated clearly.
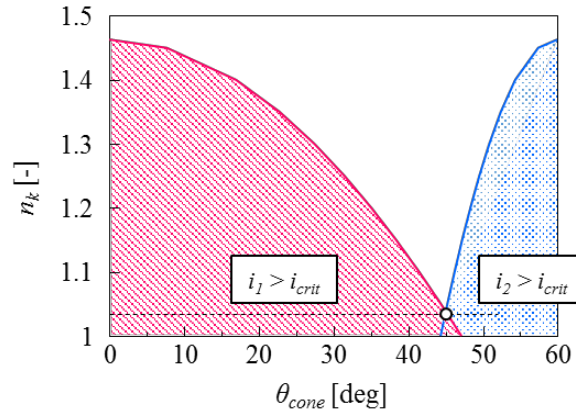
Figure 2.3: Optimization of θ_{cone}. The area where $\left[i_1 > i_{crit}\right] \cap \left[i_2 > i_{crit}\right]$ is good for θ_{cone}.

8

For example, the phase detection from air (n =1.0) to water (n = 1.33) is easily discriminated, however, that from water to paraffin oil (n = 1.45) is difficult. Anyway, the two-state optical signal from OFP sensing tip is thus performed. Those optical technique is almost free of electrical noise and intrinsic response time limitations during phase detection compared to other techniques (resistance, capacitance, and thermal probes)[29].

Note that above theoretical approach is not practical for rigorous analysis of the OFP signal. In particular, numerous patterns of rays' paths in the optical fiber are not fully-considered due to the simplified 2D theory.

Qualitative description For any types of the OFP, researchers use photodetectors to convert the lights returned from the tip into electric signals, and distinguish the phase (gas or liquid) with which the tips are covered. Therefore, the difference in the intensity of the returned beams between the phases is very important. In nature incident light in the optical fiber do not return; therefore, knowing how to obtain intensive returned beams from the sensing tip is vital to all OFP methods. The intensity of the returned beams depends on the refractive indices of the optical fiber, the gas and liquid phases, the shape of the OFP tip, and the optical smoothness of the tip surface. In particular, the shape of the OFP tip directly contributes to the intensity of the returned beams. The refractive indices of the above substances and the critical angles are summarized in Table 2.1. To obtain the intensive returned beams directly from the tip surface, several types of tip shapes such as the U-shaped tip[30], the stretched cone-shaped tip[31] and the cylindrical tip[32] were designed. The returned beams from the tip are the result of scattering caused by the total reflection of the propagated beams at the tip surface. Therefore, the tip should be of a shape that best utilizes the characteristics of the total reflection on the tip surface, and this is the wedge shape. Although

9

the chemically processed cone-shape tip is suitable for gas–liquid phase detection, the inextricable uncertainty due to the probe–bubble interaction remains.

A wedge-shaped tip is firstly proposed by Saito[14] and his group[17-23]. Figure 2.4 illustrates its phase detection principle. The change of the total reflection areas on the OFP tip is drawn. It is assumed that the amount of this change directly relates to the intensity of the return light.

Table 2.1: Refractive indices of the medium and critical angles.

Phase (refractive index)	Optical fiber (refractive index)	Critical angle [deg]
Air (1.00)	Core (1.46)	43
	Clad (1.44)	44
Water (1.33)	Core (1.46)	65
	Clad (1.44)	68
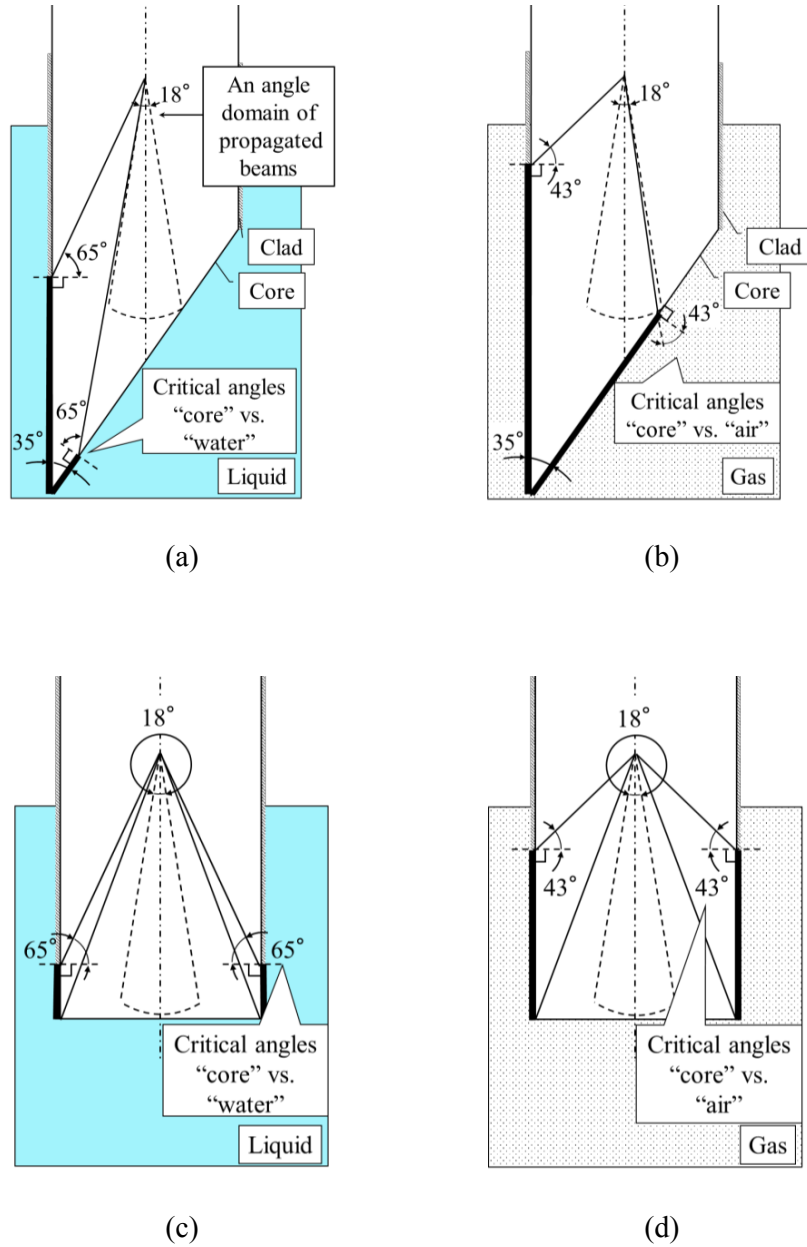
Figure 2.4: Schematics of the phase detection of the wedge-shaped and cylindrical tips: the core is exposed at the ground surface (sensing tip) only. The bold line depicts the total reflection area which contributes to the intensity of the returned beams from the sensing tip.

The fan-shaped area, depicted as dotted lines, is an angle domain of the beams propagated in the fiber core and is determined by the refractive indices of the core and clad optical fibers. The pivot and cross-section surface represent the most dominant area in the wedge-shaped-tip region for the reflection at the interface of the core and the clad and the interface of the clad and the surrounding phase. The bold lines, drawn along the tip surface, indicate the all total reflection areas against the pivot and are determined by the wedge angle, the position of the pivot, and the refractive indices between the fiber core and liquid/gas. When the propagation areas are not included in the total reflection areas at the tip surface, the beams in the fiber core are discharged to the outside. As a result, the intensity of the returned beams decreases. When the propagation areas are included in the total reflection areas, some of the beams are reflected and return into the core. Consequently, the intensity of the returned beams increases. In Figure 2.4(a), the tip is positioned in the water phase. Almost all beams are emitted into the water through the fiber–water boundary, and hence, the intensity of the beams returned from the tip is low. In Figure 2.4(b), the tip is positioned in the air phase. Most of the beams are reflected and return into the fiber, and therefore, the intensity of the returned beams is high. According to this qualitative analysis, the difference in the intensity of the returned beams between the tip positions in the water and air phases is the highest when the wedge angle is around 35°. On the other hand, as seen in Figures 2.4(c) and (d), the returned beams are almost the same, regardless of the phase covering the tip, when the tip is cylindrical. In this case, the signal/noise (S/N) ratio for the gas-liquid detection is very small. In the wedge-shaped tip, almost all propagated beams in the fiber are used for sensing phases, allowing researchers to obtain two-state signals. Moreover, the optic signal from the wedge-shaped tip includes a very informative signal (pre-signal/post-signal). This

12

phenomenon allows us to solve the challenging problem encountered in all previous OFP measurement systems.

Velocity measurement of a Single-Tip Optical fiber Probe In general, the interface velocity U_{int} is measured by the longitudinal correlation or separation between two-probes (Eq. [2.3]), however, the OFP with wedge-shaped tip can measure U_{int} only single fiber, which is very important advantage over the other probe methods. The single type of the OFP with wedge-shaped tip is mentioned as a Single-Tip Optical fiber Probe (S-TOP) in this thesis. Here, the velocity of the gas-liquid interface can be measured by using the rate of change of the S-TOP signal during its penetration of the interface.

When the S-TOP tip touches the gas-liquid interface, the surface of the tip is gradually exposed to the other phase. Then the intensity of the returned beams changes and thus the output of the photodetector, V_{pf}, changes. We calculate V_{pf} as the intensity of the returned beams. The increase/decrease in the returned-beam intensity is indicated as the sum of I, the light energy of the returned beams, which is distributed on the exposed area S, and thus,

$$V_{pf} = \int_S I(h)\,dS \qquad (2.7)$$

where I is the intensity, $h = H'$ (the length from the S-TOP tip to the interface on the S-TOP tip surface)/H (the length of the wedge), and S is the area of the S-TOP tip surface exposed to the other phase (Figure 2.5). To calculate this, we consider the distribution of I on the S-TOP tip surface on the basis of the following assumptions: 1) the beam-intensity distribution in the fiber is greatest at the center of the fiber and is normally distributed. 2) The tip surface

is optically rough to scatter the beams inward, and thus, some beams are returned (the intensity of the scattered beams corresponds to the intensity of the reflected beams; hence, we calculate the intensity of the reflected beams as I with the Fresnel equation). 3) The beams are unpolarized. Figure 2.6 shows I in each phase (the solid line indicates that the tip is positioned in water and the dotted line indicates that the tip is positioned in gas), evaluated with the Fresnel equation over the reflection area along the tip surface (Figures 2.4 (a) and (b) and the assumptions).
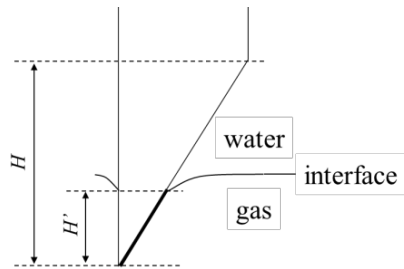
Figure 2.5: Definition of *h*. The bold line indicates the length of the wedge exposed to the

gas phase.
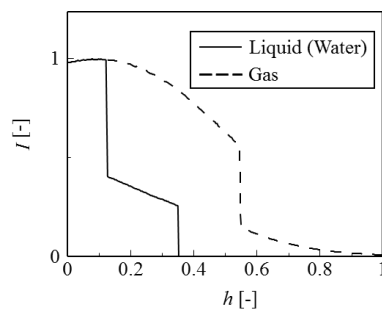
Figure 2.6: Distribution of the returned beam energy.
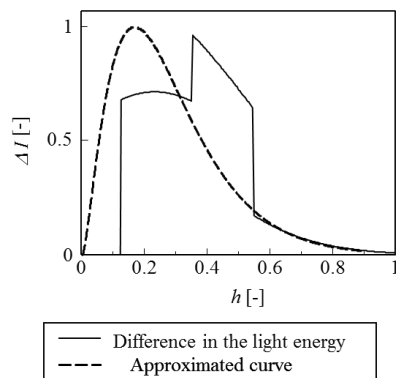
Figure 2.7: Difference in the light energy of the returned beam between gas and water.

The upslope/downslope of the S-TOP signal during its penetration of the interface is determined by the difference in the returned-beam intensity in each phase. Then,

$$V_{pf} = \int_S \Delta I(h)\, dS = \int_S I_{gas}(h)\, dS - \int_S I_{liquid}(h)\, dS \qquad (2.8)$$

where ΔI is the difference in the light energy of the returned beam between the gas (I_{gas}) and liquid (I_{liquid}) phases, as shown in Figure 2.7. We assumed that ΔI is given as a chi-squared distribution. The three-dimensional reflection/refraction of the beams which is neglected in Fig. 2.4 brings about the difference in ΔI. According to Figure 2.7, and considering the areas exposed to the other phase as a function of h (Figure 2.8), Eq. (2.7) is transformed to

$$V_{pf} = \int_S \Delta I(h)\, dS = \begin{cases} \beta h & \text{(from Gas to Liquid)} \\ (1-\beta)h & \text{(vice versa)} \end{cases} \qquad (2.9)$$

where β is a non-constant proportionality coefficient between h and V_{pf}. β indicates the intensity of the returned beams at the S-TOP tip surface. Consequently, V_{pf} is determined by the wedge angle of the tip and the refractive indices of the fiber, gas and liquid. The upslope of V_{pf} and the cumulative of ΔI are described in Figure 2.9 for instance.
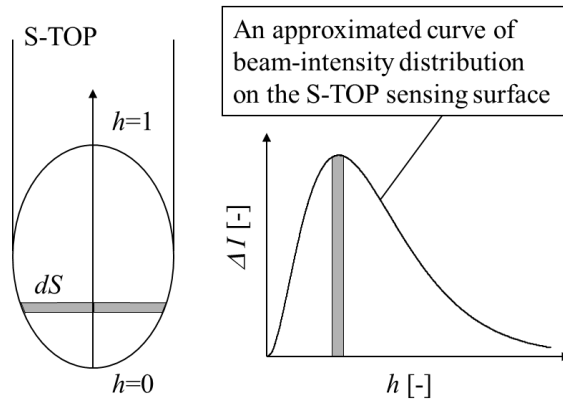
Figure 2.8: Sensing area on the S-TOP surface.
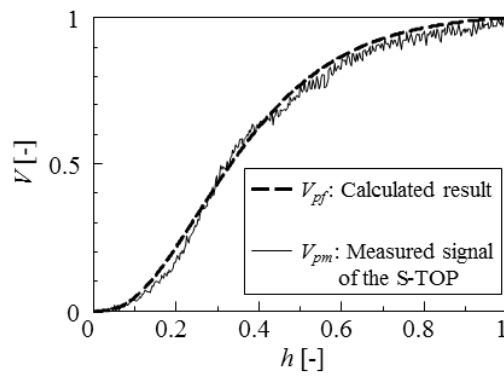
Figure 2.9: Relation between the calculated curve V_{pf} and the measured signal V_{pm}.

Assuming that i) the gas–liquid interface velocity is constant for a short time during the penetration of the interface and ii) the interface remains planar during the penetration,

$$h = \frac{H'}{H} = \frac{U_{int}t}{H} \tag{2.10}$$

where t is time and U_{int} is interface velocity. Therefore,

$$V_{pf} = \begin{cases} \beta h = \dfrac{\beta}{H} U_{int}t & \text{(from Gas to Liquid)} \\[2ex] (1-\beta)h = \dfrac{(1-\beta)}{H} U_{int}t & \text{(vice versa)} \end{cases} \tag{2.11}$$

Hence,

$$U_{int} = \alpha_k \frac{dV_{pf}}{dt} \tag{2.12}$$

where α_k is a proportionality coefficient between "the rate-of-change of the gradient" and "the velocity of an ideal (flat and undeformable) interface pierced by the S-TOP in the k-phase (gas or liquid)". The accuracy of the velocity measurement by using wedge-shaped tip is simply organized in Eq. (2.12), the precision of α_k and dV_{pf}/dt.

18

2.2 Experiment

Structure of the S-TOP   The schematic and a micrograph of the S-TOP are shown in Figures 2.10 and 2.11, respectively. The S-TOP is made from a plain optical fiber (Large core fiber [jacketed] S-series, Fujikura Ltd.: step index type with a core diameter of 190 μm and a clad thickness of 5 μm). The optical fiber is fine-drawn with a micropipette puller (P-2000, Sutter instrument Co.), then the needle-like tip is smoothly ground by a micropipette beveller (BV-10, Sutter instrument Co.) into a wedge and a few dozen of micrometers in diameter. The fiber is fixed in a stainless steel capillary (Terumo hypodermic needle 26G, Terumo medical products) with epoxy (EPO-TEK 360, Epoxy Technology Inc.), and the S-TOP and capillary are installed in a reinforcement tube of stainless steel (SUS304, 1 mm ID and 3 mm OD).
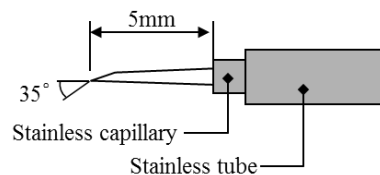
Figure 2.10: Detail of the S-TOP.
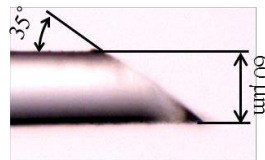
Figure 2.11: Micrograph of the wedge-shaped tip of the S-TOP.

Optics The optical system used in the S-TOP measurement is illustrated in Figure 2.12. A laser diode (1) (3 mW power, 635 nm wavelength) is used as the light source of the S-TOP. The laser beams pass through a beam splitter (2) and are focused by an objective lens (3). The focused laser beams enter an optical fiber and reach the S-TOP sensing tip (4). The laser beams reaching the tip surface are returned/emitted to/from the tip following Snell's law. The returned beams enter a photomultiplier (6) through a polarizer to eliminate unwanted beams (the beams scattered by the lens or beam splitter) (5). Hence, we obtain the electrical signal output from the photomultiplier. In succession, we analyzed the raw signals and simultaneously obtained the velocities, diameters and number densities of the bubbles.
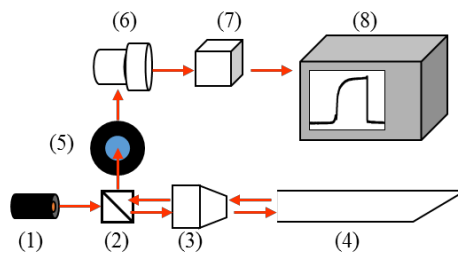
Figure 2.12: S-TOP optical system. (1)Laser diode, (2) Beam splitter, (3) Objective lens, (4) S-TOP, (5) Polarizer, (6) Photo multiplier, (7) Amplifier, and (8) Digital oscilloscope.

Quasi-piercing experiment by S-TOP   A typical S-TOP signal of quasi-piercing experiment is plotted in Figure 2.13. First, the S-TOP tip is positioned in liquid/gas at Fig. 2.13(ii) (1), and thus, the output voltage is low/high. Second, piercing the interface at Fig. 2.13(ii) (2), the S-TOP tip is in the gas/liquid at Fig. 2.13(ii) (3), and thus, the output voltage increases/decreases. The rate-of-change of the upslope/downslope, g_{rd}, is calculated as follows:

$$g_{rd} = \frac{dV}{dt} \times \frac{1}{V_{Gas} - V_{Liquid}} \qquad (2.13)$$

where V_{Gas} and V_{Liquid} are output levels of the S-TOP positioned in the gas and liquid phases. $1/(V_{Gas} - V_{Liquid})$ corrects individual variability of the S-TOP, because g_{rd} varies slightly with each S-TOP. The relationship of g_{rd} and U'_{int} (quasi-velocity of the gas-liquid interface or moving velocity of the S-TOP) is shown in Figure 2.14. U'_{int} is calculated based on Eq. (2.12),

$$U'_{int} = \alpha'_k \times g_{rd} \qquad (2.14)$$

α'_k is defined in the same as α_k, but includes the effects of wettability on the S-TOP surface. Here α'_k represents the latency length[26, 29, 33], L^*, which means the spatial resolution of the sensor working as an interface detector. L^* characterizes the penetration depth of the

21

probe tip inside the gas phase to ensure a signal increase of 80% between liquid levels. Cartellier and his group reported that the small L^* can detects undisturbed interface locations and identifies steeper transitions more easily and accurately. Here, α'_{Liquid} of our S-TOP is about 35 μm, and this value is enough to obtain g_{rd} with low disturbance. The detection time, also introduced by Cartellier, for the interface is about 10 μs when the bubble velocity is 300 mm/s. This value is superior to the other OFPs; 520 μs (a U-shaped tip), 240 μs (Abuaf's conical tip), less than 50 μs (Cartellier's conical tip)[7, 29, 33].
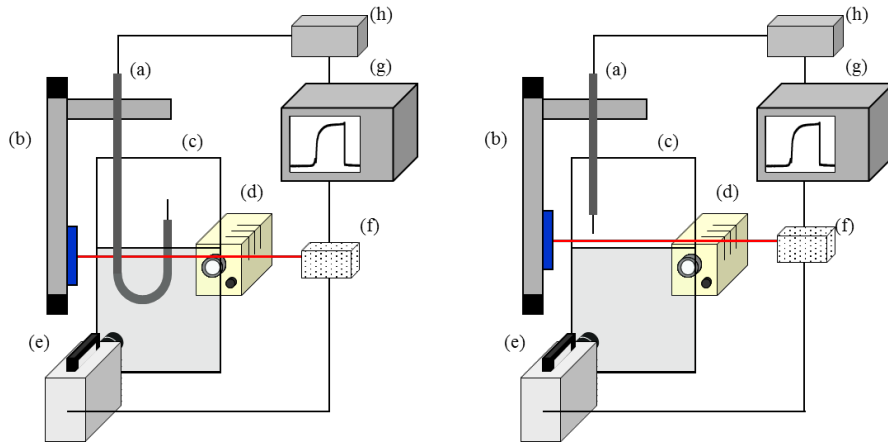
(i) Experimental setup for obtaining α'_k (left: k = Liquid, right: k = Gas) under normal

impact to a flat interface. (a) S-TOP, (b) Servo actuator, (c) Acrylic water vessel, (d)

Halogen light source, (e) High-speed video camera, (f) Synchronizer, (g) Recorder, and (h)

Optics.
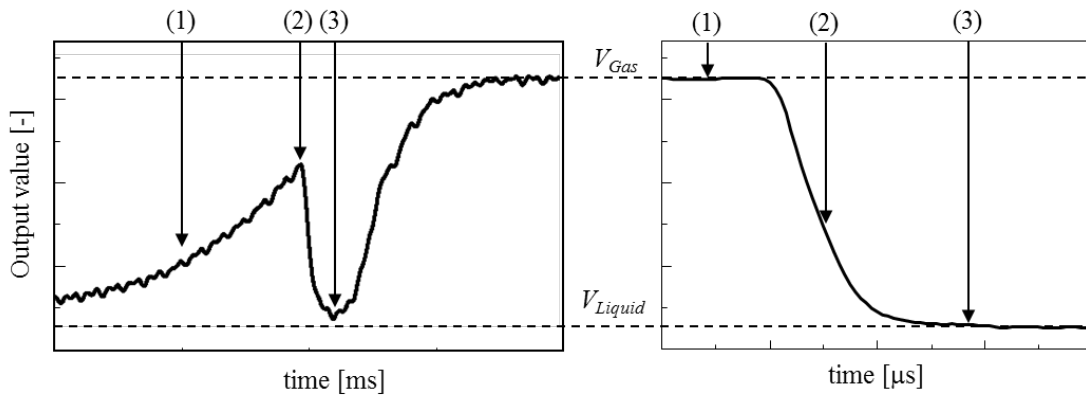
(ii) Typical output signals during the S-TOP piercing a flat interface from water-to-air (left)

and air-to-water (right).

Figure 2.13: Procedure of the quasi-piercing experiment and its typical results.
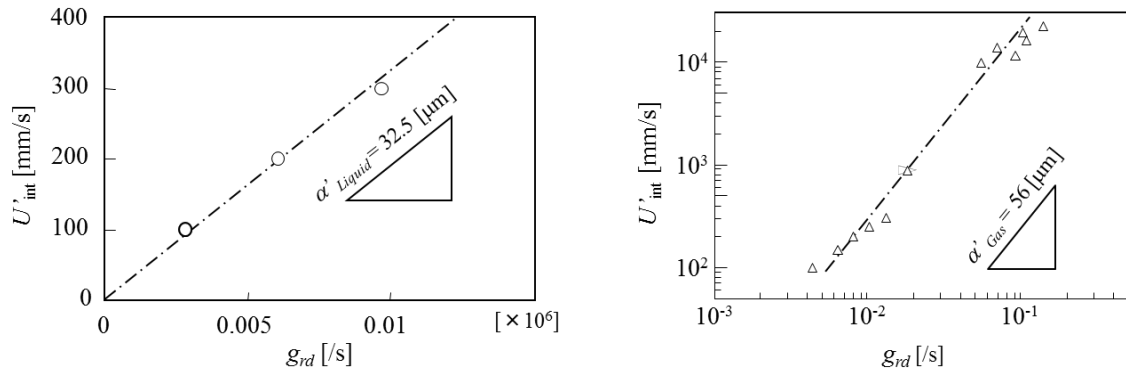
Figure 2.14: Relationship between g_{rd} vs. U'_{int} for α'_{Liquid} *(left)* and α'_{Gas} *(right)*.

2.3 Simulation

Outline of ray tracing simulation for the S-TOP A simulation for the OFP measurement is essential to carry out correct signal-processing, i.e., precise decision for g_{rd} because practical signals of the OFP include various noise due to scattering-light on the optics, fiber-entrance, and gas-liquid interface. Cartellier and Barrau[27, 28] conducted 2D ray-tracing simulation for optimizing the sensing tip of a mono-fiber optical probe firstly. This method can determine reasonable shape of the sensing tip, however, calculated signal still depart from "the reality of the wave propagation in multimode fibers". In order to overcome this, Sakamoto and Saito[34-36] developed 3D ray-tracing simulation for analyzing signals of the S-TOP, and this simulator was in good accord with experiment results. In addition, it is found that the non-axial symmetry of the S-TOP invoked very hopeful and unique phenomena. Ray tracing is a technique for rendering images with computers. The idea behind ray tracing is that physically correct images are composed by light, and that light will usually come from a light source and bounce around (reflect) as light rays in a scene before hitting our eyes or a camera. The probe signal is also led by reflection. By reproducing in a computer simulation the path followed from a light source to a photo multiplier, we are able to produce physically relevant meanings of the signal. Following descriptions of the way of the 3D ray tracing simulation are excerpted from the PhD thesis by Sakamoto[37].

A light wave propagating in the fiber was simplified as discrete ray segments. Conditions of the target optical setup of the S-TOP are: that there be no magnetized object; that the step-index optical fiber be homogeneous and lossless; and, that the probe diameter (inlet tip: 230 μm, sensing tip: 60 μm) be a sufficient amount larger than the source light wavelength (635 nm). The path and energy of the rays were calculated by considering the incident angles and

refractive indices of the mediums.

The path of a reflecting/refracting ray was calculated as a vector in consideration of a reflection/refraction angle. The reflection angle is the same as the incident angle. The refraction angle is given by Snell's law,

$$\frac{\sin \theta_t}{\sin \theta_i} = \frac{n_i}{n_t}$$

(2.15)

where θ_i, θ_t, n_i, n_t are the incident angle, the refracting angle, the refractive index of the incoming media, and the refractive index of the transmitting media, respectively. The energy of a reflecting/refracting ray was calculated from the reflectivity/transmissivity governed by Fresnel's equation,

$$R_P = \frac{\tan^2 \left(\theta_i - |\theta_t| \right)}{\tan^2 \left(\theta_i + |\theta_t| \right)}$$

(2.16)

$$R_S = \frac{\sin^2 \left(\theta_i - |\theta_t| \right)}{\sin^2 \left(\theta_i + |\theta_t| \right)}$$

(2.17)

where R_P and R_S are reflectivities of parallel and perpendicular polarization, respectively; for transmissivity,

$$T_P = \frac{\sin(2\theta_i)\sin(2|\theta_t|)}{\sin^2(\theta_i + |\theta_t|)\cos^2(\theta_i - |\theta_t|)} \tag{2.18}$$

$$T_S = \frac{\sin(2\theta_i)\sin(2|\theta_t|)}{\sin^2(\theta_i + |\theta_t|)} \tag{2.19}$$

where T_P and T_S are the transmissivities of parallel and perpendicular polarization, respectively. Here, we assume that the interfaces are optically smooth enough to neglect random reflection. All the ray energy that returns from the sensing tip was summed up as the output voltage.

Figure 2.15 is a flow chart of this computation. The objects of the computation were categorized and rendered into three primitive types: BODY, SURFACE, and RAY. Every object possessed particular information that corresponded to the optical phenomena of the S-TOP system and was needed for the ray-tracing calculation; i.e., a BODY had a homogeneous refractive index, a SURFACE had its 3D shape information, and a RAY had its root point and direction. Owing to good linkage among the objects, the computational cost was successfully lowered. Moreover, we were able to easily track the history of every light path and energy in the fiber.
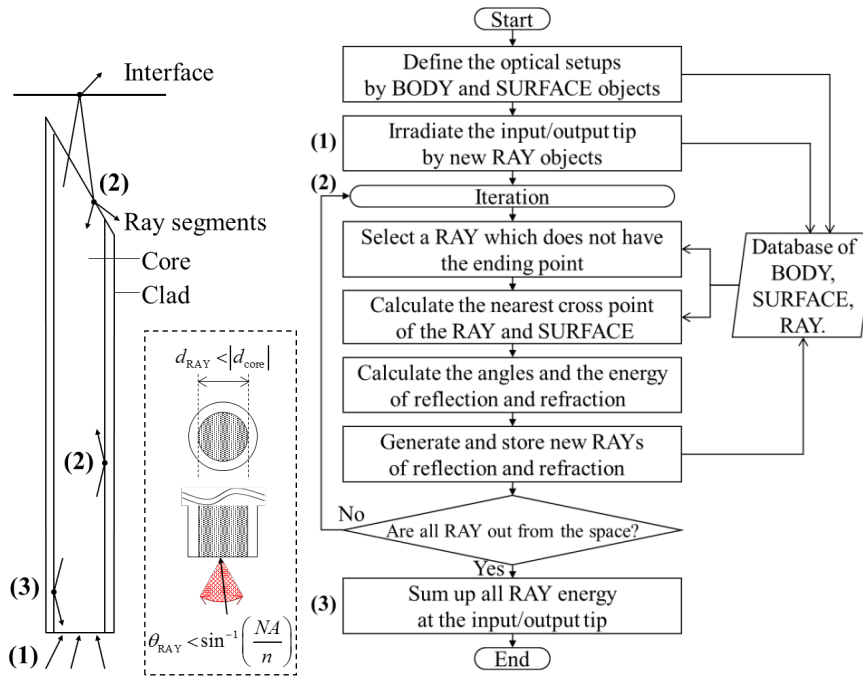
Figure 2.15: Flow chart of the 3D ray-tracing simulation

A typical computation result of the S-TOP signal is shown in Figure 2.16. (i) is a calculated signal of the S-TOP during penetration of the interface. At (b), a small spike shows a short peak, as in the experiment shown. In tracking the history of the light path contributing to the signal, the S-TOP signal can be classified into the on/off signal (Fig. 2.16[ii]) and the spike signal (Fig. 2.16[iii]). The former is the reflected light at the sensing tip and the latter is reflected light at the gas-liquid interface near the S-TOP. Each signal is introduced in a simulated fashion below.

On/off signal (phase detection signal) As is the case with experiment, some rays reaching the S-TOP tip reflect and return due to the large difference in the refractive indices of the fiber core (1.46) and air (1.0) when the S-TOP is in the air. The output voltage of V_{Gas} must reach a certain level. If the S-TOP is in the water, almost all of the rays are discharged into the water due to small difference in refractive indices of fiber core and water (1.33); as a result, the output level of V_{Liquid} becomes almost zero. Thus, an on/off signal is obtained as a phase detection. Figure 2.17 is the relationship of the wedge-angle θ_w and a ratio R of the signal intensity of each phase ($\sim V_{Gas}/V_{Liquid}$). Three peaks in Fig. 2.17 is indicated as the effective angles at 30˚, 45˚, and 90˚ at which a large number of the rays are reflected by the wedge-shaped tip. From the view point of the simulation, the return rays exists in any part of the fiber by means of reflection, refraction, and scattering; however, they usually leak out from the lateral side of the fiber because the critical angle of the optical fiber is very large. Those effective angles, therefore, lead the return rays "straightly" to the inlet tip of the S-TOP.

Small spike signal (surface detection signal) A small spike[22] is found just before the S-TOP pierces interface from water to air (Fig. 2.16[iii]). The interface is detected by the reflection of itself. The amount of the surface reflection is large when the light passes from water to air; the more the S-TOP approaches the interface, the more the reflected light re-enters the S-TOP; after its tip starts to pierce, the interface deforms with meniscus, which reduces the amount of the re-entrance; and the re-entrance becomes zero after the S-TOP finishes piercing. Hence the spike signal peaks before the penetration. The spike also detects the front/rear surface of the bubble/droplet before penetration at its peak. In other words, the peak of the spike signal indicates "the time at which the S-TOP tip touches the gas-liquid

interface". The spike signal accurately and objectively detects the interface position of the bubble/droplet. This fact is very simple yet important for the OFP signal processing because anyone has found the interface through the OFP signal so far.
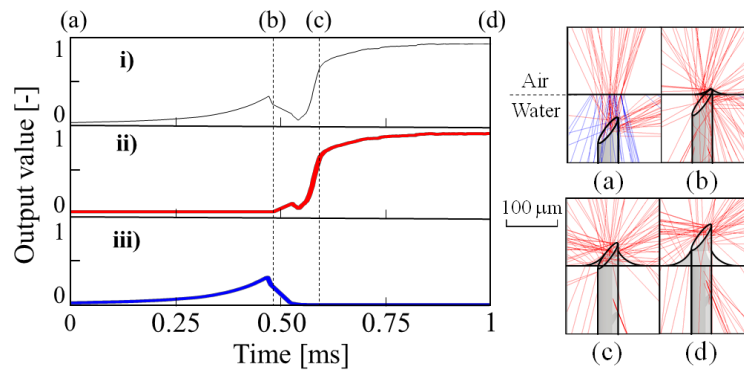
Figure 2.16: Simulation result of the S-TOP penetrating the gas-liquid interface.
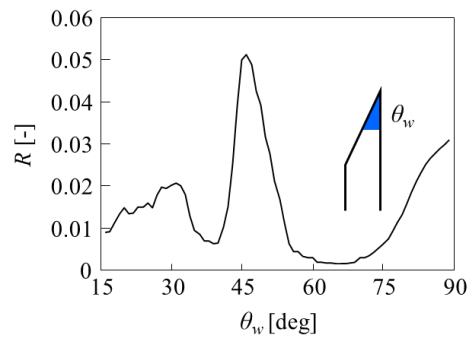
Figure 2.17: Consideration of the effective angle of the S-TOP. *R* means the ratio of the rays' intensity at the inlet tip of the S-TOP positioned in air or water.

In addition, the intensity of the spike signal (I_{spike}) derives from the eccentricity of the contact of a bubble/droplet. Figure 2.18 is a simulation result of I_{spike} at various angles. I_{spike} takes the largest value, when the S-TOP touches the interface normally, i.e., the spike signal can also detect the center region of the elliptic shape. Although such condition is not often, it is very informative to know where/how the S-TOP pierces the bubble/droplet through the signal. Those properties have been known as impossible to find and therefore treated as inevitable uncertainties of probe measurement. In this context, the spike signal is essential for improving the robustness and reliability of bubble/droplet measurement with OFP.

Based on the results, new measurement methods of the S-TOP for the bubble/droplet in the flow are developed in the next chapter. Here the spike signal is mentioned as a *pre-signal* for the bubble measurement and *post-signal* for the droplet measurement.
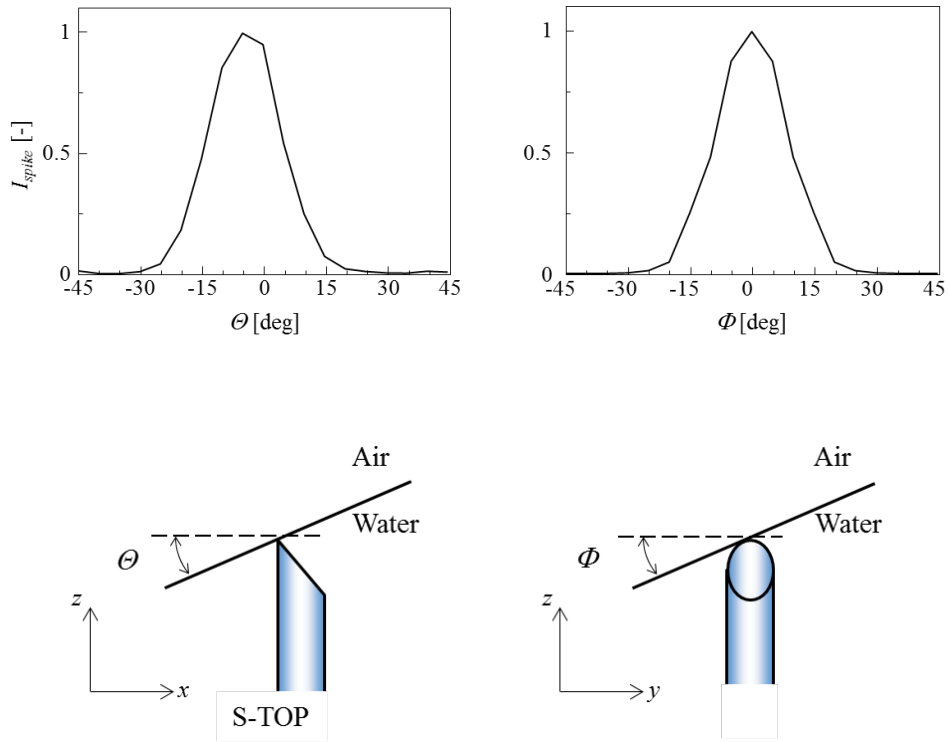
Figure 2.18: Intensity of the spike signal (I_{spike}) at various angles.

3. Pre-signal threshold method for bubble measurement

3.1 Signal processing for bubble measurement

A typical S-TOP signal in the single-bubble measurement (unitary signal) is plotted in Figure 3.1. First, the S-TOP tip is positioned in water, and the output voltage is low. Second, piercing the bubble, the S-TOP tip is in gas, and the output voltage increases. Finally, the piercing is finished, and the S-TOP tip is positioned in water again; hence, the output voltage decreases.

Signal processing is conducted by a biphasic method, our original approximation procedure for the OFP signal (Sakamoto and Saito, see Appendix B). The raw signal can be expressed in mathematical form $V_{BP}(t)$ (biphasic curve) as follows,

$$V_{BP}\left(t\right)=\xi_{Gas}+\frac{\xi_{Liquid1}-\xi_{Gas}}{1+\exp\left\{4g_{rd}\left(t-t_{1}\right)\right\}}+\frac{\xi_{Liquid2}-\xi_{Gas}}{1+\exp\left\{4g_{rd}'\left(t_{2}-t\right)\right\}} \qquad (3.1)$$

where ξ_{Gas}, ξ_{Liquid} are normalized V_{Gas} and V_{Liquid} in the S-TOP signal; g_{rd} and g_{rd}' are the gradients of upslope and downslope of the unitary signal; and t_1 and t_2 are midpoint of the slopes. According to Eq. (3.1) and an assumption that the local interface velocity is a representative of the velocity of the gravity center of the bubble (the bubble velocity, U_B),

$$U_B = \alpha'_{Liquid} \times g_{rd} \qquad\qquad (3.2)$$

where α'_{Liquid} is a proportionality coefficient (Figure 2.14). The pierced chord length is calculated as follows:

$$L_B = U_B \times (t_e - t_s) \qquad\qquad (3.3)$$

where $(t_e - t_s)$ is the residence time of the S-TOP tip covered completely by the bubble. t_e (the time at which the S-TOP is in contact with rear surface of the bubble) and t_s (the time at which the S-TOP starts to touch the bubble's frontal surface) are calculated formally,

$$t_e = t_2 - \frac{1}{2g'_{rd}} \qquad\qquad (3.4)$$

$$t_s = t_{s,BP} = t_1 - \frac{1}{2g_{rd}} \qquad\qquad (3.5)$$

t_s is also defined as "the peak-time of the spike (pre-signal) in the raw signal". The properties of the pre-signal including $t_{s,pre}$-definition will be introduced following section. In this thesis, t_s indicates $t_{s,pre}$, unless otherwise stated.
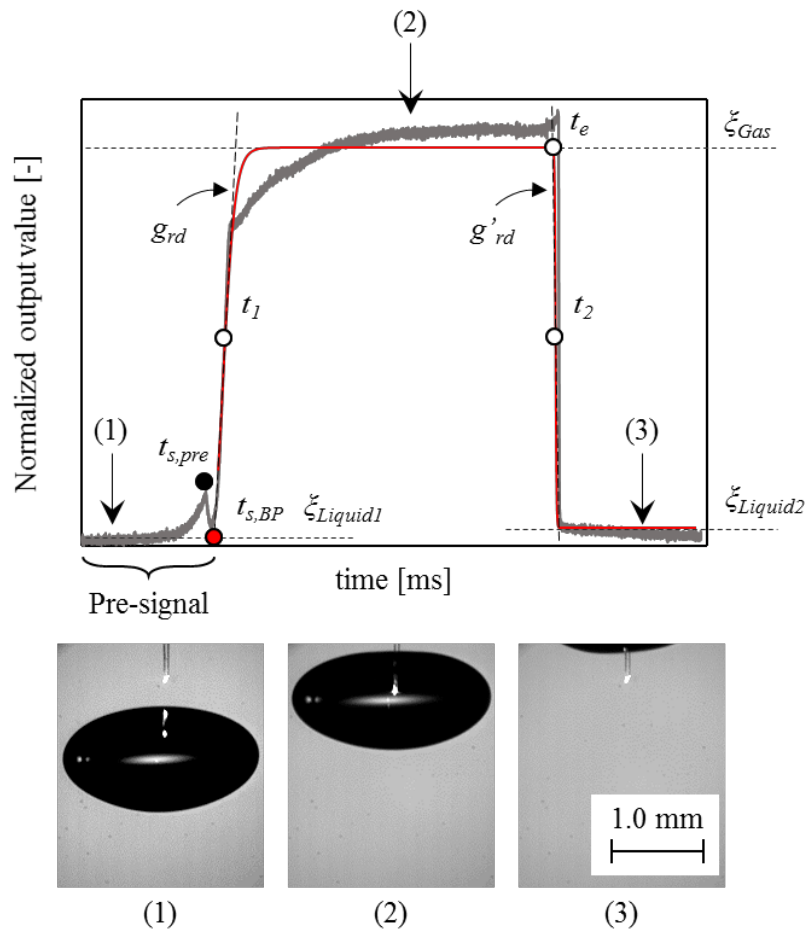
Figure 3.1: Typical output signal of the S-TOP in the single bubble measurement. Gray-colored line is the raw signal and red line is $V_{BP}(t)$.

3.2 Properties of the pre-signal (experiment)

Preface   The spike signal, which we refer to as the pre-signal, is observed just before the S-TOP pierces the bubble. According to the chapter 2, the time at the peak indicates t_s, the start time of the S-TOP tip touching the bubble frontal surface (touching the interface from water to air). Indeed, the spike is found clearly only by the S-TOP measurement. Laser beams in the wedge-shaped tip repeat the total reflection between the wedge-shaped surface and the opposite clad, then accumulate at the pointed end of the tip. Therefore, the beams discharged from the wedge-shaped tip in water results in a strong directivity compared to the other OFPs. The discharged beams are visualized by using YAG laser of 532 nm wavelength and fluorescent substance (Rhoadamine B, excitation: 532 nm, emission: 570 nm). The intensive beams discharged from the pointed end of the tip are observed in Figure 3.2 (a) marked with (A). The beams from the wedge-shaped tip distributes in the axial direction of the S-TOP. The discharged beams from the S-TOP are reflected at the bubble frontal surface (Figure 3.2 (b)), and detected as the pre-signal. Hence, in order to make an efficient collection of the surface reflection, rapidly, strong-beams should distribute just beneath the S-TOP tip. In this context, the wedge-shape is the most reasonable tip for the pre-signal detection.

     The pre-signal appears only when the S-TOP pierces a bubble vertically near its pole. That is, the pierced conditions (position/angle) can be objectively distinguished by the S-TOP signal, which has been considered as inevitable problems of the OFP measurements. Cartellier[26-29, 33] and other researchers[38, 39] reported the pre-signal by using an OFP, but no one discussed its detailed characteristics or how to use them for their OFP measurements. In this thesis, the pre-signal intensity is used for the measurement of bubbly flow (pre-signal threshold method). Here, its intensity is defined bellow:

$$V_P = (V_{Pmax} - V_{Liquid})/(V_{Gas} - V_{Liquid}) \qquad (3.6)$$
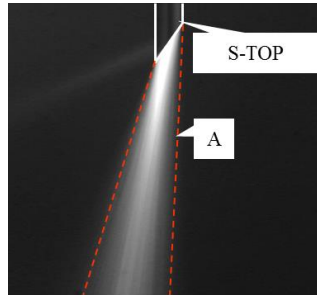
(a) Directional characteristic of discharged beams.
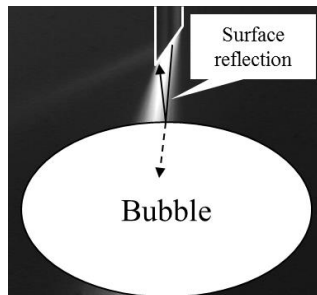
(b) Schematic of the pre-signal detection. Some of the discharged beams are reflected at the

bubble surface, which are collected as the pre-signal.

Figure 3.2: Visualization of the discharged beams from the S-TOP.

Pre-signal properties analysis by experiment   The experimental setup is illustrated in

Figure 3.3. A single bubble (Air: CO < 1 vol. ppm, CO_2 < 1 vol. ppm, THC < 1 vol.ppm) is

launched from a hypodermic needle (Terumo hypodermic needle 27G, Terumo medical

products) (g) into an acrylic vessel (f) of $150 \times 150 \times 300$ mm^3. It is filled with ion-exchanged and degassed tap water. The bubble ascends vertically and touches the S-TOP (a) fixed above the needle. The tip diameter and the wedge angle of the S-TOP are 60 μm and 35°, respectively.
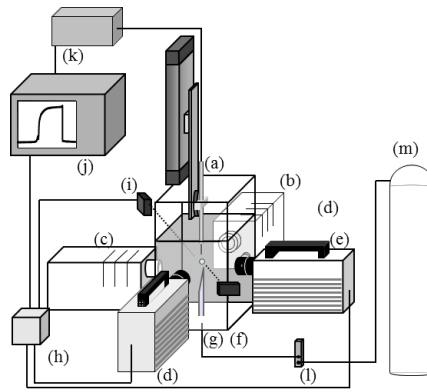
Figure 3.3: Experimental setup for single bubble measurement. (a) S-TOP, (b) (c) Halogen light sources, (d) (e) High-speed video cameras, (f) Acrylic water vessel, (g) Needle, (h) Electrical power supply, (i) Optical sensor, (j) Recorder, (k) Optics, (l) Flow meter, and (m) Cylinder

The S-TOP positioning conditions against the examined bubble is shown in Figure 3.4. We measured fifty times (bubbles) per condition. The percentage in this figure is $\Delta_{S\text{-}TOP}/L_m$ (touch position), where $\Delta_{S\text{-}TOP}$ is the distance between the bubble center and the S-TOP's touching point, and L_m is the major axis of the bubble. Hence, 0% corresponds to the center of the bubble. We varied the angle of touching (touch angle θ) at respective positions from −45° to 45° by 15°, and observed the influence of the touch angle on the pre-signal. To obtain

a quantitative relation between the measurement points and the pre-signal, we used two high-speed video cameras (FASTCAM SA1.1, Photron). The signal from the S-TOP and the cameras are synchronized using a function generator.
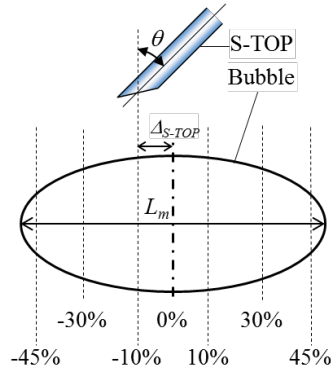
Figure 3.4: Experimental conditions of $\Delta_{S\text{-}TOP}$ and θ.

Figure 3.5 summarizes the typical output signals and snapshots of the S-TOP of touch angle $\theta = 0°$. In Case 1, the pre-signal occurs intensively and appears just before the S-TOP pierces the bubble frontal surface. The peak value of the pre-signal against the touch position is shown in Figure 3.6. The peak value is maximum at 0% (i.e. in Case 1, the probe touches the central region of the bubble). The value decreases with the shift of the touch position towards the outer edge of the bubble. Figure 3.7 shows the visualization of the discharged beams from the S-TOP tip at the single-bubble measurement by using a fluorescent material (Rhoadamine B). The reflected beams at the bubble surface head for directions other than that of the S-TOP axis, with the shift of the touch position towards the outer edge of the

bubble. As a result, the intensity of the beams returned to the probe decreases, and the pre-signal intensity at the edge of the bubbles is lower than that at the center.
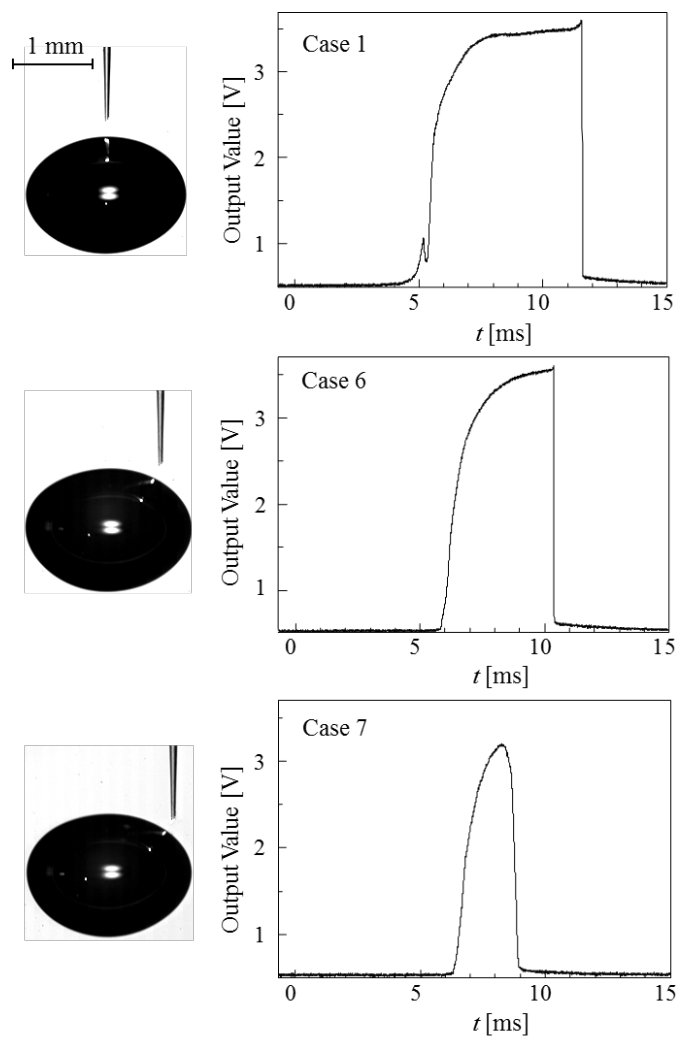
Figure 3.5: Output signals and corresponding snapshots of the S-TOP.
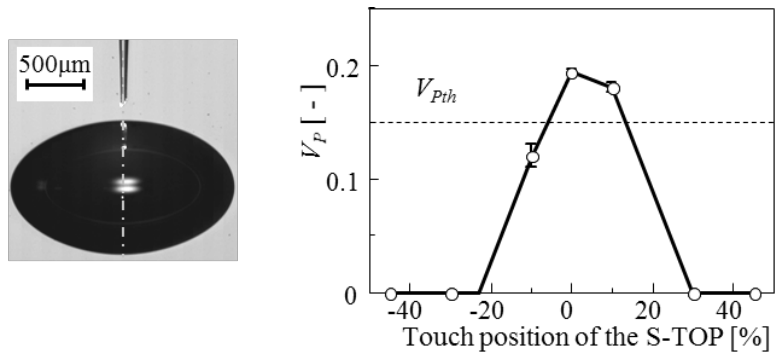
Figure 3.6: Relation between V_P and the touch position of the S-TOP.
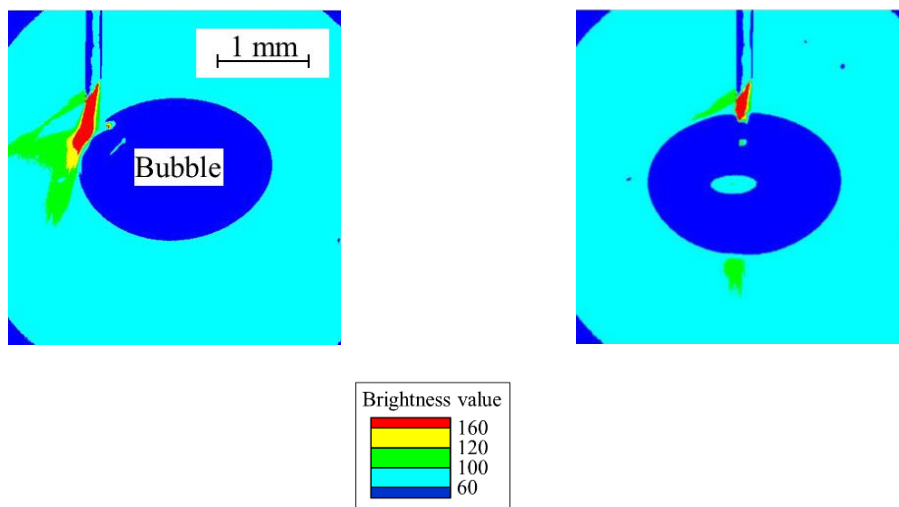
(a) $\Delta_{S\text{-}TOP}/L_m = -45\%$ (b) $\Delta_{S\text{-}TOP}/L_m = 0\%$

Figure 3.7: Visualization of the discharged beams from the S-TOP during the signale-bubble measurement (pseudo-colored images).

The peak values of the pre-signal against the touch positions at each touch angle are plotted in Figure 3.8. In each condition, the pre-signal intensity depends on the touch position of the S-TOP. However, the position in which the pre-signal takes the maximum value tends to shift away from the center (Table 3(a)). In addition, the maximum value is much smaller than that at $\theta = 0°$.
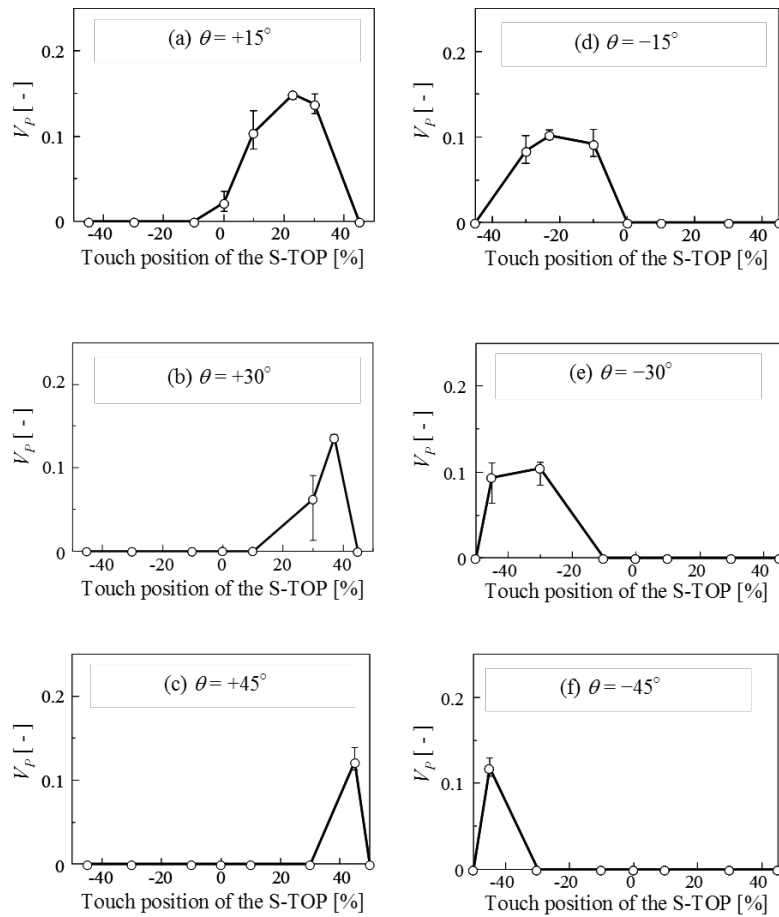
Figure 3.8: Shift of the pre-signal peak against θ.

The shift of the pre-signal peak position is attributed to the high sensitivity of the pre-signal to the angle ϕ of the impact on the local interface (Figure 3.9). The pre-signal takes the maximum value at $\phi = 0°$. In the θ range of 15–45°, the points that satisfy the condition $\phi = 0°$ also tend to shift towards the edge of the bubbles, as shown in Table 3.1 (b). The calculation of the touch position is based on the experimental data, and is performed as follows. First, draw a line tangent to the bubble contour and then a line normal to the tangent. Second, if the S-TOP axis (inclined at θ) coincides with the vertical line ($\phi = 0$), the point of the tangent is regarded as the calculated touch position. Therefore, the position in which the pre-signal takes the maximum value tends to shift away from the center. In fact, the values of Table 3.1 (a) are much similar to those of Table 3.1 (b).
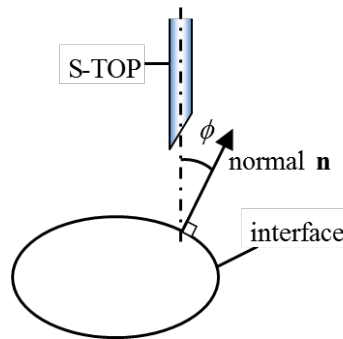
Figure 3.9: Angle ϕ in the S-TOP-interface interaction ($\theta = 0°$).

The decrease in the maximum value is attributed to the local interface curvature of the bubbles. The bubbles examined in this study are ellipsoidal, so the local interface curvature increases towards their edges. The difference in curvature induces a difference in diffusion

of the reflected light on the interface. Consequently, as long as the local interface curvature is large, some of the reflected beams at the bubble surface head in directions other than that along the axis of the S-TOP even when $\phi = 0°$. The results for negative touch angles of the S-TOP are similar to these results. Thus, the maximum value is smaller than that at $\theta = 0°$.

Table 3.1: Pre-signal peak points.

(a) Experimental results

θ [deg]	Pre-signal's peak point [%]
15	23
30	37
45	45

(b) Calculation results

θ [deg]	Calculated point [%]
15	21
30	35
45	43

Introduction of a pre-signal threshold method   On the basis of the above results, we can detect the S-TOP's piercing position/angle with the pre-signal intensity, i.e. we can obtain significant information of whether the S-TOP pierces the center region of the bubble vertically. By using this newly developed detection method, we can discriminate where and how the S-TOP has touched the bubble in a flow (i.e. identifying whether the S-TOP pierces the center of the bubble parallel to its minor axis).

To improve the measurement accuracy of the S-TOP, we need to extract the signals when the S-TOP vertically pierces the center region of the bubble (hereafter 'true signals'). Table 3.2 lists the measurement results of the bubble chord length from the above experiment.

Table 3.2: Difference between S-TOP and the visualization results ($\theta = 0°$).

position [%]	L_B [mm]	minor axis [mm]	difference [%]
0	1.42		4.4
10	1.08	1.36	-20
30	0.8		-41
45	-		-

L_B is calculated by the S-TOP signal, and the minor axis is calculated from the visualization. The difference of the results increases when the touch position departs from the center. In the S-TOP measurement of a bubbly flow, such uncertainty is difficult to remove. Clark and Turton estimated the uncertainty of a chord length[24] owing to a position pierced by a probe. Vejražka and his group[40] discussed the measurement accuracy of the mono-fiber optical probe in a bubbly flow and proposed a method for correcting the uncertainty by focusing on the modified Weber number. We focus on the pre-signal intensity, which is the pre-signal threshold method, whose schematic is shown in Figure 3.10. We divide the serial data obtained from the S-TOP into unitary signals. Calculating the V_{Gas}, V_{liquid} and V_{Pmax}, we obtain V_P. The threshold for V_P is defined as $V_P > V_{Pth} = 0.15$, as described in Figure 3.6. Signal (1) in Fig. 3.10 includes the pre-signal of $V_P = 0.20$. This means that signal (1) is the candidate signal to be analysed as the true signal. On the other hand, signals (2) and (3) do not include any pre-signal. This means that the S-TOP has touched the outer region of the bubble, or the bubble has grazed the S-TOP tip; the penetration is imperfect. Hence, these

signals are not used or needed for calculating U_B and L_B. As a result, we select only signal (1).

Thus, only the true signals are collected, and we can discriminate the pierced position within

±10%. The flowchart of the newly developed signal process is summarized in Figure 3.11.
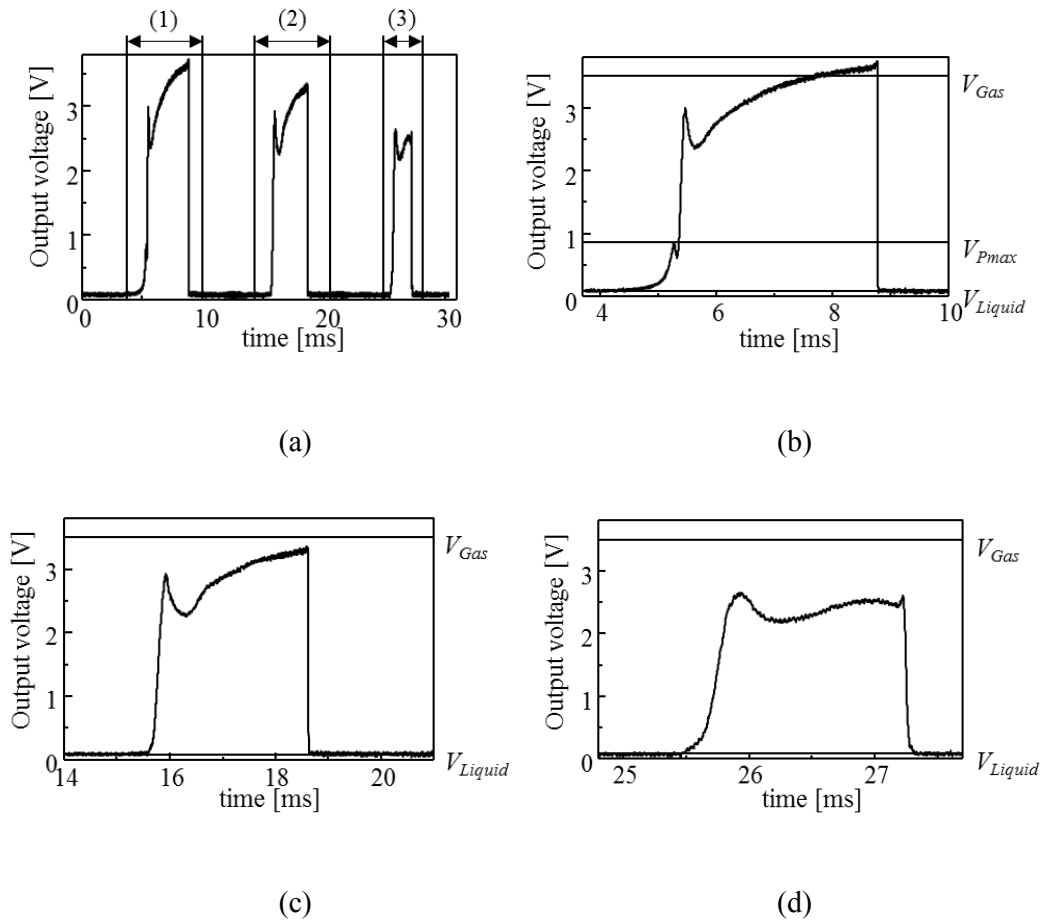
Figure 3.10: Schematic of the pre-signal threshold method. (a)Examples of serial signals delivered by the S-TOP, (b) Signal (1): $V_P = 0.20$ ($>V_{Pth} = 0.15$) ($V_{Gas} = 3.50$ [V], $V_{Liquid} = 0.10$ [V], $V_{Pmax} = 0.70$ [V]), (c) Signal (2): $V_P = 0$ ($<V_{Pth}$) ($V_{Gas} = 3.2$ [V], $V_{Liquid} = 0.10$ [V], $V_{Pmax} = 0$ [V]), and (d) Signal (3): $V_P = 0$ ($<V_{Pth}$) ($V_{Gas} = 2.5$ [V], $V_{Liquid} = 0$ [V], $V_{Pmax} = 0$ [V])

46
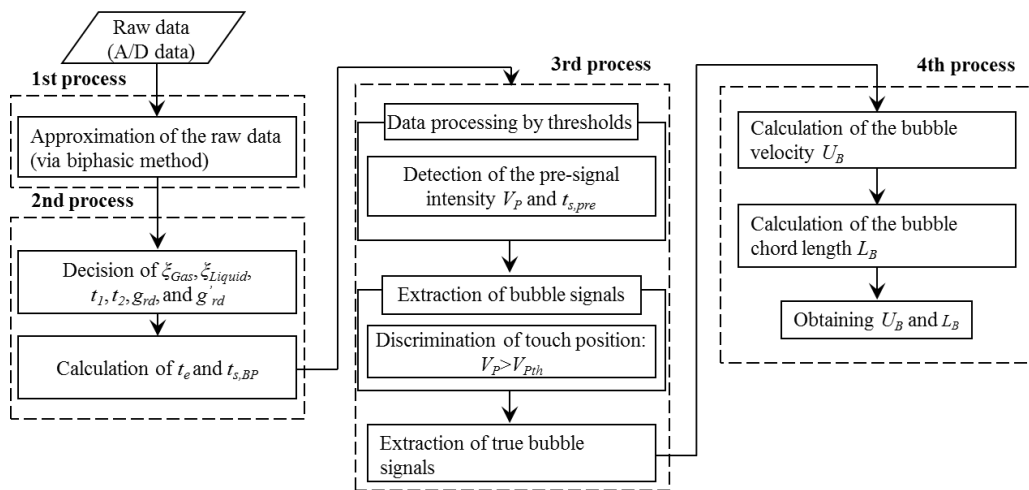
Figure 3.11: Flowchart of the newly developed signal processing.

3.3 Demonstration of the pre-signal threshold method

In this experiment, we demonstrated the effectiveness of the pre-signal threshold method. The experimental setup is illustrated in Figure 3.12. The vessel is made of an acrylic pipe (149 mm in inner diameter and 600 mm in height) covered with a rectangular acrylic water jacket to remove refraction and deformation of the image. The bubble swarms are grown and launched from hypodermic needles (Terumo hypodermic needle 23G, Terumo medical products) using a bubble launch device that forms repeatedly uniform bubbles at controllable launch timing[41-46]. The device consists of a function generator, which arbitrarily controls the bubble launch interval, and audio speakers. The S-TOP is fixed 200 mm above the needles. Thus, 1,000 bubbles of almost uniform size were measured via the S-TOP.

The bubble properties are listed in Table 3.3. These values are evaluated with a robust image processing method[41, 42]. The equivalent bubble diameter derived from this method was the same as that derived from the direct sampling method. The error was about 1% of an equivalent bubble diameter. The bubbles were captured after the launch. Using an LED as backlight, we obtained images with a strong contrast between the bubble contour and background (Figure 3.13). The center-of-gravity positions and the contours of the bubbles were obtained from a series of digital image processing (binarization, labelling, and so on). In addition, due to such strong contrast, the lighting method was very effective in observing the bubble behavior quantitatively. Further details on this method are given in the references.
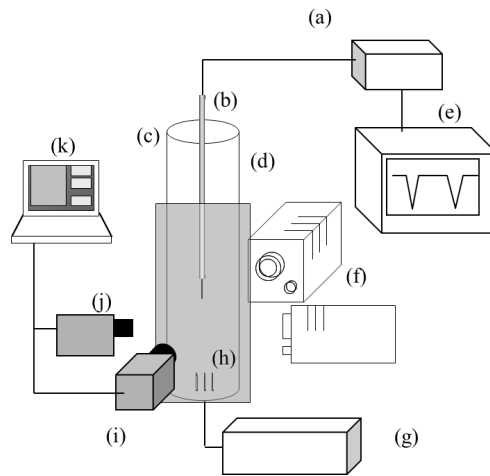
Figure 3.12: Experimental setup for the bubble-column measurement. (a) Optics, (b) S-TOP, (c) Cylindrical vessel, (d) Rectangular water jacket, (e) Recorder, (f) LED lights, (g) Bubble launch device, (h) Needles, (i)(j) High speed video cameras, and (k) PC.

Table 3.3: Bubble properties in the bubble column experiments.

Average bubble velocity	295 [mm/s]
Average aspect ratio	0.47 [-]
D_{eq}	2.64 [mm]
Re	770 [-]
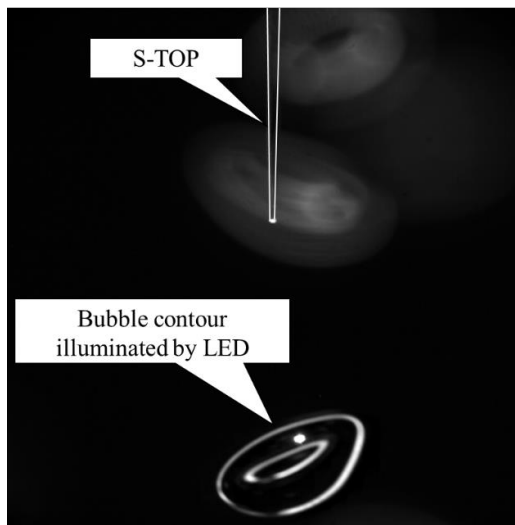
Figure 3.13: Captured image of the S-TOP and a bubble, which is illuminated by LED

backlight, in a bubbly flow.

Velocity measurement The results of the velocity measurements are shown in Figure 3.14. These figures prove the effectiveness of the pre-signal method. In Figure 3.14(a), the white bar indicates the probability density function (PDF) obtained from the visualization, and the black bar shows that obtained from the S-TOP (unprocessed by the pre-signal threshold method). The measurement results are summarized in Table 3.4. The PDF of the visualization has a peak only at 300 mm/s, whereas that of the S-TOP (unprocessed) has two peaks. The average velocity obtained from the visualization is 295 mm/s, whereas that from the S-TOP (unprocessed) is 258 mm/s. The difference in the average velocities is about 13%. The differences are caused by counting the signals of incomplete penetration of the S-TOP when the S-TOP touched the edge area of the bubbles or the S-TOP scratched the bubbles. It is very difficult to distinguish when the S-TOP touches a bubble, which is why usual signal processing cannot eliminate inappropriate signals. As a result, the values of the S-TOP (unprocessed) have a widespread distribution. To solve this serious problem in data processing, we employed the newly developed pre-signal method for processing the raw S-TOP signals. The gray bar in Figure 3.14(b) represents the PDF of the velocity obtained from the S-TOP (processed by the pre-signal threshold method). Obviously, the precision of the S-TOP is significantly improved. Furthermore, the average velocity is 319 mm/s, so the difference between the visualization and S-TOP results is also reduced to 8%.

51

(a)

(b)
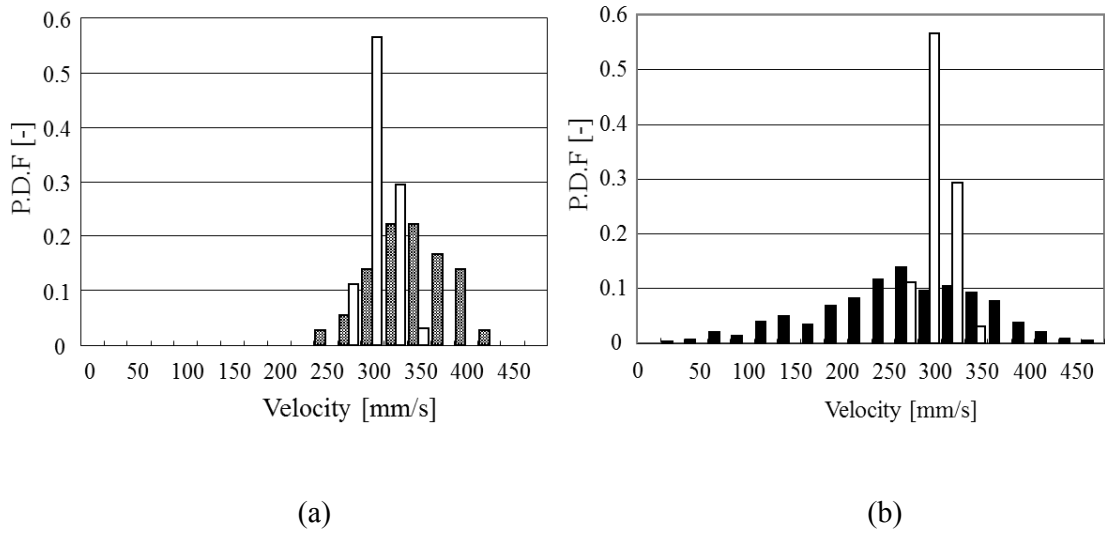
Figure 3.14: Results of the velocity measurement. (a) Visualization and S-TOP

(unprocessed) and (b) Visualization and S-TOP (processed)

Table 3.4: Velocity measurement results of S-TOP.

(a) Visualization vs. S-TOP (unprocessed)

Visualization [mm/s]	S-TOP (unprocessed) [mm/s]	Difference [%]
295	258	−13

(b) Visualization vs. S-TOP (processed)

Visualization [mm/s]	S-TOP (processed) [mm/s]	Difference [%]
295	319	8

Chord length measurement Figure 3.15 shows the differences of the chord length between the visualization and S-TOP (unprocessed/processed). Each average value is listed in Table 3.5. The pre-signal method remarkably improved the accuracy of the chord length measurement because the method successfully removed the inappropriate signals. The difference in the results of the visualization and S-TOP was significantly decreased from 42% to 16%. The pre-signal method is not only simple but also a powerful way to process S-TOP signals.

(a)   (b)
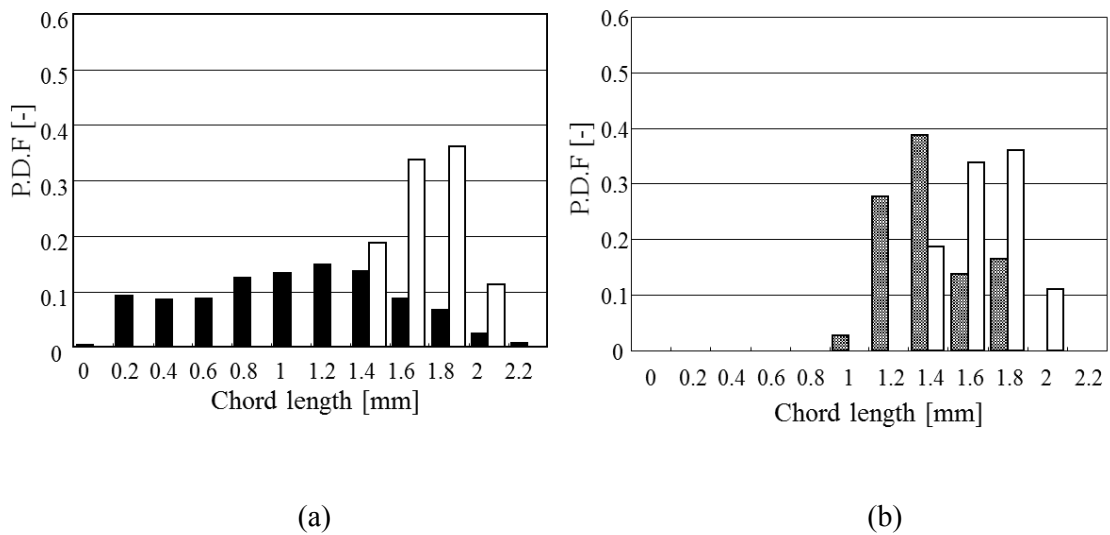
Figure 3.15: Results of the chord length measurement. (a) Visualization and S-TOP (unprocessed) and (b) Visualization and S-TOP (processed).

Table3.5: Chord length measurement results.

(a) Visualization vs. S-TOP (unprocessed)

Visualization [mm]	S-TOP (unprocessed) [mm]	Difference [%]
1.59	0.93	−42

(b) Visualization vs. S-TOP (processed)

Visualization [mm]	S-TOP (processed) [mm/s]	Difference [%]
1.59	1.33	−16

3.4 Uncertainty analysis

Uncertainty in the velocity measurement   The 8% difference in the velocity measurement between the S-TOP and visualization, caused by the deceleration of the bubble due to intrusion and the method for calculating velocity, remains. When the S-TOP penetrates a bubble near its pole (flat interface), the calculated velocity is underestimated by approximately 10% (bias value), owing to deceleration[40] derived from interface deformation (Figure 3.16); however, the velocity is overestimated in the bubbly flow measurement. This is because of another uncertainty in the S-TOP measurement. The bubble velocity is calculated by Eq. (3.2), where α'_{Liquid} is the coefficient of proportionality between g_{rd} and the velocity of the local interface. In addition, α'_{Liquid} is based on an assumption that the interface of the bubble is flat and not inclined; however, the actual bubble interface has a curvature. We discuss how this uncertainty affects the measurement results.

We employed $V_P = 0.15$ as the threshold to detect the pre-signals. This value corresponded to ±10% allowances in the touch position from 0 to +15° allowances in the touch angle. Conducting single bubble measurements, we investigated the differences resulting from these allowances. The difference in the velocities was estimated at about 10%. The maximum difference occurs at −10% (touch position) and 0° (touch angle) (Figure 3.17). The mechanism is explained as follows. The velocity detected by the S-TOP tip at the above condition is overestimated because the curved interface covers the S-TOP tip, as illustrated in Figure 3.18, faster than the flat interface. This unfavourable effect cannot be removed from the raw data, and thus, the velocity measurement results of the S-TOP are larger than those of the visualization.
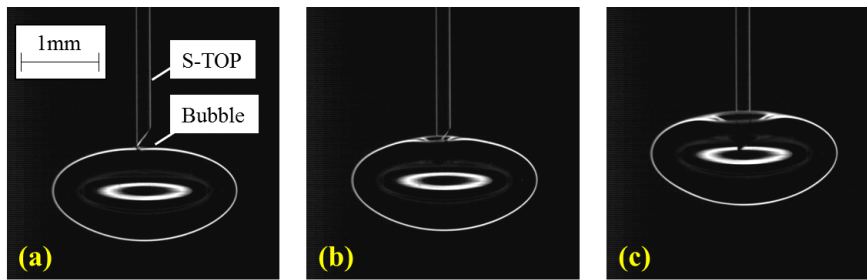
Figure 3.16: Deformation of the frontal surface of the bubble. (a) the S-TOP touches on the bubble, (b) the S-TOP starts to pierce the frontal surface, and (c) the S-TOP tip is in the bubble
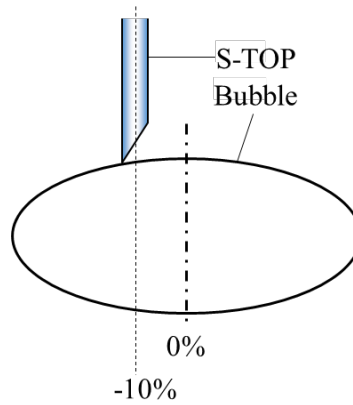
Figure 3.17: Critical condition in the velocity measurement of S-TOP.
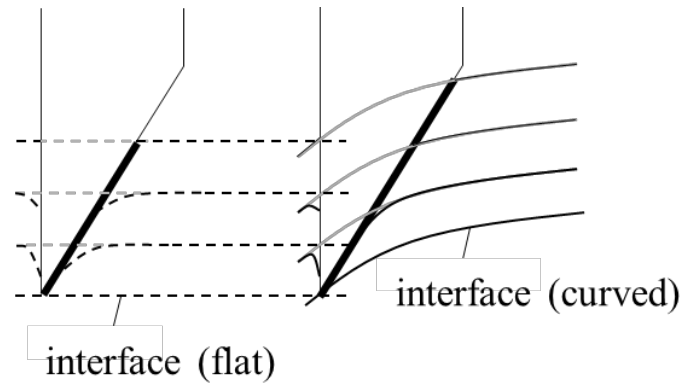
Figure 3.18: Comparison of the contact process in detecting the velocity at a pseudo-flat or curved interface by using the wedge-shaped tip

Uncertainty in the chord length measurement   The difference between L_B (measured chord length) and L_{minor} (length of the bubble minor axis from visualization) is 16% at maximum. Here the uncertainty of the t_s and t_e decision, one of the major uncertainties in the chord length measurement of the existing phase detection probes, is quite small. According to the pre-signal property, t_s indeed indicates the moment at which the S-TOP touched the bubble frontal surface. The detection error of t_e, the time of the end of the gas inclusion, is shorter than 30 μs[20]. The residence time obtained from the objective bubbles ($D_{eq} = 2 - 3$ [mm], volume-equivalent diameter) is about 5 ms. Hence, the effect due to the detection error of t_e is only less than 1% of the residence time. As a result, the calculation of the dwell time ($t_e - t_s$) is satisfactorily accurate.

The uncertainty in the measurement of L_B is caused by the following factors: a) the

57

uncertainty in the velocity calculation; b) the extended dwell time due to the deceleration owing to interface deformation; c) the randomness of the touch angle/position and d) the modulated bubble ascending motion after the penetration of the probe tip into the deformed interface in the bubbly flow.

a) The uncertainty of the velocity calculation is already discussed above.

b) The extended dwell time is due to deceleration. Vejražka[40] evaluated this effect. In our well-controlled bubbles ($D_{eq} = 2.6$ [mm], in stagnant water), the dwell time also increased by about 10%.

c) The randomness of the touch angle/position can be quantified using a 3D Monte Carlo method. As discussed in the previous section, the extracted pre-signals indicate that the S-TOP touches the bubbles at an area within a 10% radius from the center and at an angle range of within 15°. Figure 3.19 shows the schematic of the procedure. We performed random calculations of the chord lengths that the S-TOP can output in those ranges. First, the random angles θ_{MC1} and θ_{MC2} are given in the range between 0 and 15°. Second, the random positions L_{MC1}/L_m and L_{MC2}/L_m are given in the range from -10% to 10%, and finally, the chord length CL_{MC} is calculated geometrically. Comparing the maximum and minimum lengths, we see that the differences converge at 5%.

d) In the bubbly flow measurements, another uncertainty arises due to the particularly ascending motion of bubbles, even if an S-TOP pierces a bubble at the center of the bubble frontal surface. The ascending motions of the bubbles are zigzag/helix motion in the bubbly flow experiment shown in Figure 3.20. These motions bring more uncertain contact patterns to the S-TOP measurements, and this creates the inconsistency between L_B and L_{minor}. Figure

3.20 depicts the S-TOP signal and the corresponding snapshots visualized from two directions in the bubbly flow. According to this, although the touch position/angle is desirable for the chord length measurement, the bubble behaves unpredictably after the contact. Consequently, although the pre-signal intensity is indicated to be large, the piercing condition is not necessarily desirable. Obviously, $L_{minor} > L_B$.

The uncertainty d) was the most dominant uncertainty in the bubbly flow experiment. Andreotti[47] successfully measured the mono-dispersed bubbly flow via a mono-fibre optical probe; however, the experimental condition was $D_{eq} < 2$ [mm] and $Re = 20–30$ [-] with an upward flowing glycerine solution. In this case, at least, the uncertainty derived from the bubble motion shall have a small effect; hence, the S-TOP can accurately measure them as well. We think that our experimental conditions are closer to the actual conditions in bubbly flows.

Summarizing these considerations, the measurement uncertainties of the chord length in the bubbly flow are 'the velocity calculation error', 'the extended dwell time', 'the randomness of the touch angle/position' and 'the bubble motion'. To overcome these uncertainties, we need to further study the S-TOP signal.
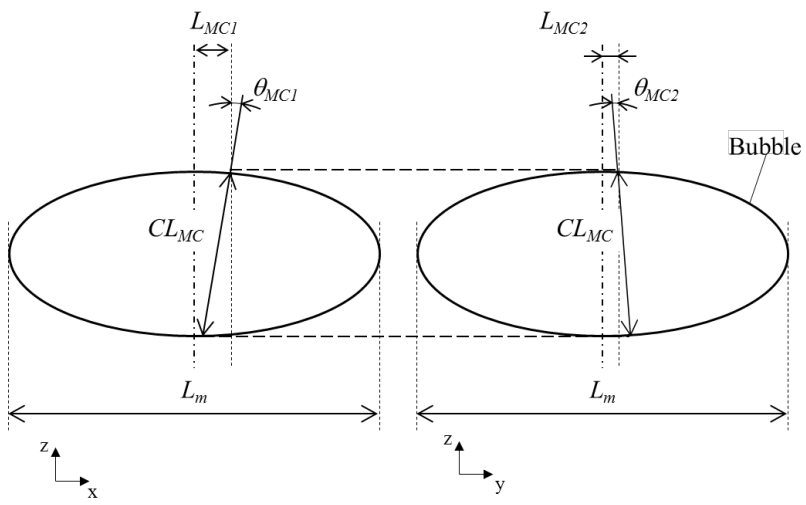
Figure 3.19: Parameters in the Monte Carlo scenario.
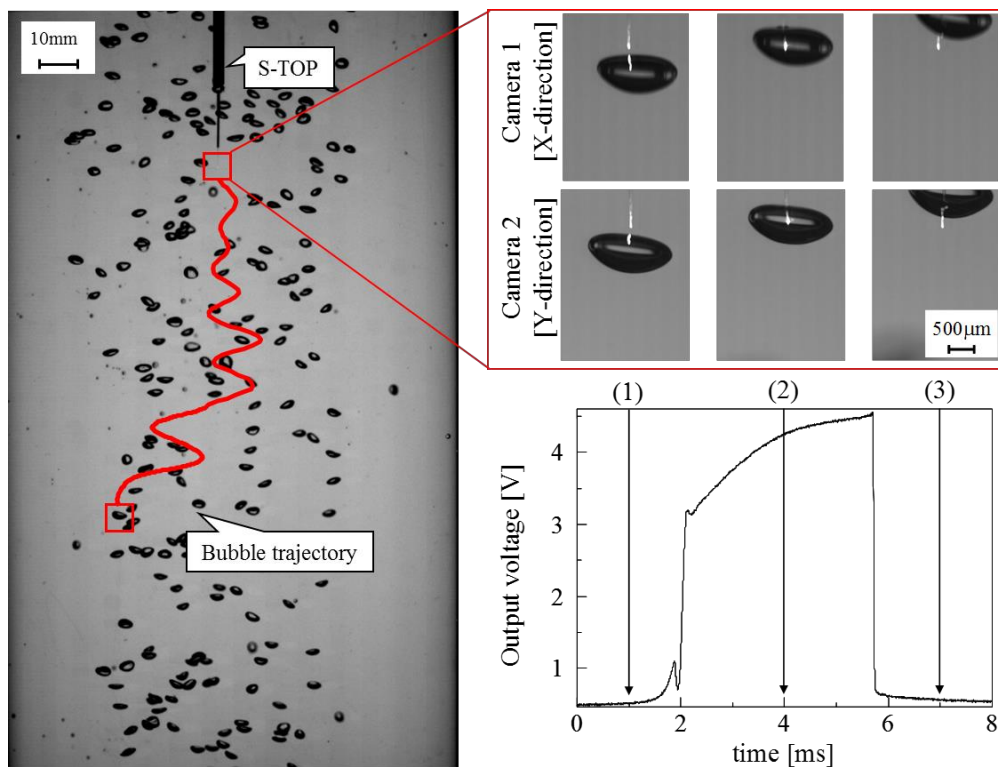
Figure 3.20: Bubbly flow measurement via the S-TOP, the corresponding 2D images and output signal. Although the pre-signal is intensive ($V_P > 0.15$), the bubble does not ascend vertically. As a result, the measured chord length is shorter than the minor axis of the bubble.

On the basis of these results, we can consider the advantages and limitations of the newly developed method. The pre-signal threshold method enables us to discriminate where and how the S-TOP has touched a bubble, with no statistical process involved. This issue is one of the controversies regarding the phase detection probe. When the pre-signal method is applied, the dispersion of the chord lengths is considerably improved. Figure 32 shows the

comparison of the standard deviations between the processed and unprocessed chord lengths. The parameter $\sigma_{Chord\ length}$ remarkably decreases from 0.8 [mm] (unprocessed) to 0.04 [mm] (processed).
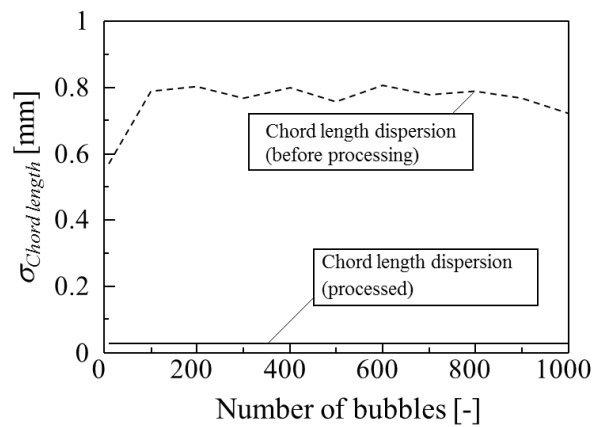
Figure 3.21: Comparison of the chord length dispersion.

The present investigation was conducted in the mono-dispersed bubbly flow, and the liquid was water. Hence, there are certain limitations in applying the pre-signal threshold method to an actual bubbly flow. The application range in bubble size for this method is 0.8–5 [mm] (volume-equivalent diameter). These values resulted from the experiments in the air–water two-phase flow. Moreover, the motion of the target bubbles should be moderate in the bubbly flow (liquid-phase superficial velocity is nearly equal to the bubble terminal velocity, e.g. chemical plant for phenol production).

The lower limit, 0.8 [mm], is the penetration limit of the S-TOP into the bubble, which

means that the S-TOP is unable to overcome the surface tension force of the bubble. In this case, the calculated velocity and chord length will have other uncertainties owing to deceleration by the intrusiveness of the probe. Vejražka and his group[40] reported that the influence is evaluated with a modified Weber number, which characterizes the bubble's ability to overcome the surface tension force arising from the contact with the probe tip. Moreover, the local interface curvature of a small bubble is larger than that of a large bubble near their pole. The difference of the interface curvature contributes to the difference of the pre-signal intensity. Therefore, in order to discuss the adaptability of the pre-signal method for bubbles smaller than 0.8 [mm], further investigation is needed.

The upper limit of 5 [mm] is due to the geometrical and path instability of the bubbles and liquid turbulence. Bubbles in motion are generally classified by their shape as spherical, oblate ellipsoidal and spherical/ellipsoidal cap. The actual shape depends on the relative magnitude of the relevant forces acting on the bubble[48]. Large bubbles considerably oscillate (geometrically unstable) since the inertia force is more dominant than surface tension. In addition, the ascending path of the bubbles changes depending on their size (aspect ratio). When the bubble size is larger than 2.33 [mm] (volume-equivalent diameter) in stagnant water, the bubble starts zigzag motion. The bubble motion is also susceptible to liquid turbulence. This instability causes the uncertainties in the chord length measurement. Depending on the magnitude of these factors, the upper limit decreases.

At least, the spherical bubbles have very small diameters for measuring through any optical fibre probe. In particular, bubbles with diameter of about 1–5 [mm] (volume-equivalent diameter) are suitable for conventional probe methods.

4. Droplet measurement and upcoming problem for the S-TOP

4.1 Signal processing for droplet measurement

Figure 4.1 shows a typical output signal of a single droplet measurement by the S-TOP. According to the biphasic method, the signal is expressed with the simple mathematical form,

$$V_{BP}(t) = \xi_{Liquid} + \frac{\xi_{Gas1} - \xi_{Liquid}}{1 + \exp\{4g'_{rd}(t_1 - t)\}} + \frac{\xi_{Gas2} - \xi_{Liquid}}{1 + \exp\{4g_{rd}(t - t_2)\}} \quad (4.1)$$

where ξ_{Gas}, ξ_{Liquid} are normalized V_{Gas} and V_{Liquid} in the S-TOP signal; g_{rd} and g'_{rd} are the gradients of upslope and downslope of the unitary signal; and t_1 and t_2 are midpoint of the slopes. The parameters (the droplet velocity U_D and pierced chord length L_D) of the droplet are calculated in a similar way of the bubble measurement,

$$U_D = \alpha'_{Gas} \times g'_{rd} \quad (4.2)$$

$$L_D = U_D \times (t_e - t_s) \quad (4.3)$$

$$t_s = t_1 - \frac{1}{2g'_{rd}} \quad (4.4)$$

64

$$t_e = t_{e,BP} = t_2 - \frac{1}{2g_{rd}} \qquad\qquad (4.5)$$

U_D is assumed that the local interface velocity is a representative of the velocity of the gravity center of the droplet. α'_{Gas} is the proportionality coefficient obtained by the preliminary experiment (Figure 2.13). Actually, the number of the reports about droplet measurement using OFP is quite few[50], because the uncertainty of the touch position in small-droplets flow is relatively larger than that in bubbly flow. The droplets should be precisely detected with the OFP signals. The spike signal is found around t_e (the time at which the S-TOP is in contact with rear surface of the droplet). In the droplet measurement, the spike is called as a post-signal and when the post-signal is detected, t_e can be "the peak-time of the post-signal in the raw signal". t_e indicates $t_{e,pos}$, unless otherwise stated further on.
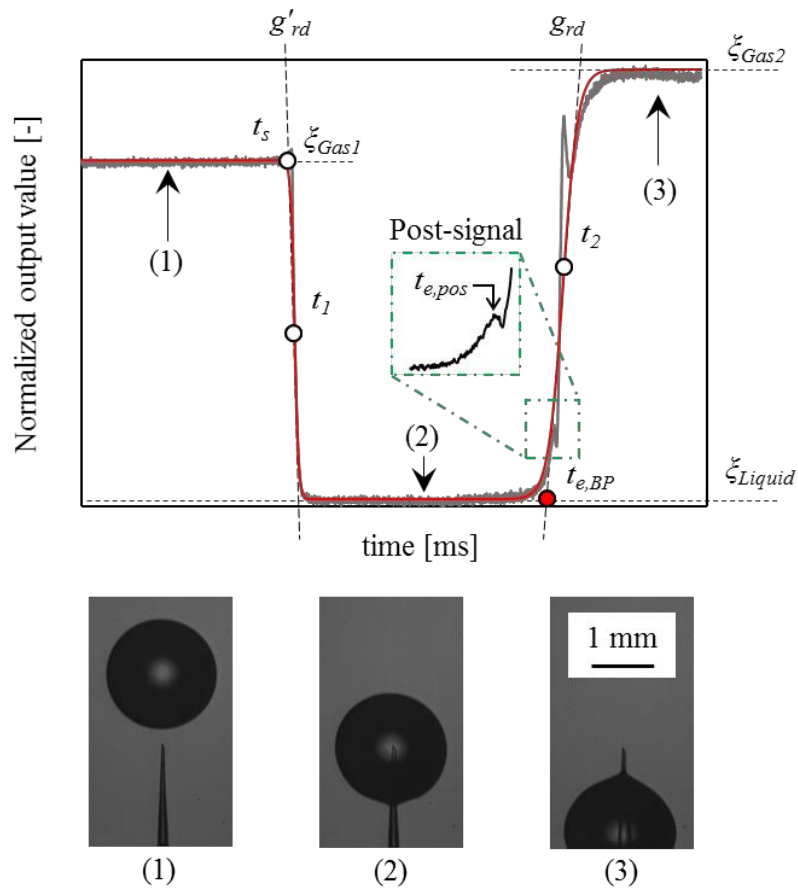
Figure 4.1: Typical output signal of the S-TOP in the single droplet measurement. Gray-colored line is the raw signal and red line is $V_{BP}(t)$.

4.2 Post-signal threshold method

The spike signal, i.e., the interface detection signal or pre-signal in the bubble measurement, is also found in droplet measurement before the S-TOP pierces the rear surface of the droplet. It gives us to detect $t_{e,pos}$ for correct chord length measurement and pierced position in the same manner of the pre-signal (see chapter 3). In this section, a post-signal threshold method is introduced and demonstrated to distinguish the pierced position.

Post-signal properties analysis by experiment   Figure 4.2 is a schematic diagram of the experimental setup. A large vessel filled with ion-exchanged water was placed where the water surface is at 25-cm higher than the micro capillary (140-µm inner diameter fabricated by micropipette puller [P-2000, Sutter Instrument Company]). The water was introduced through the capillary, then single droplets appeared and fell freely at the S-TOP (Figure 4.3) of 10-cm below. The average diameter and velocity were 1.92 mm and 1.03 m/s. We checked measure-to-measure reproducibility of these parameters including trajectory of whole experiments, and confirmed the values varied within ±1% in terms of 100 droplets. The S-TOP (tip diameter 50-µm, wedge angle 30˚, the same as Fig. 2) is fixed on a three-axis microstage (KS162 and KS362, Suruga Seiki co., ltd.), at controlled touch positions of $\varDelta_{S\text{-}TOP}/D$ = 0, 10, 30, 45%, respectively (Figure 4.4). We visualized the process of the droplets pierced by the S-TOP using a high-speed video cameras (frame rate 10000 fps, exposure time 50 µs, resolution 1024×512 pixels, and spatial resolution 8.33 µm/pixel) through shadowgraph.
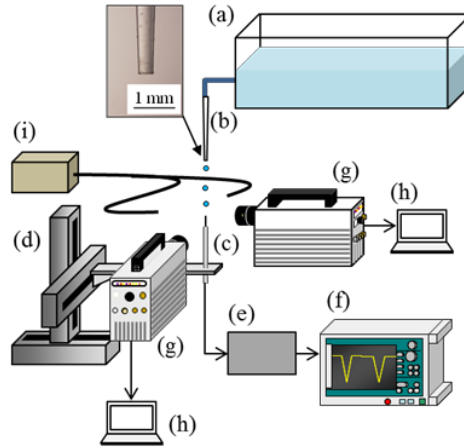
Figure 4.2: Experimental setup for droplet measurement. (a) Vessel, (b) Glass capillary, (c) S-TOP, (d) 3 axis stage, (e) Optics, (f) Data logger, (g) Camera, (h) PC, and (i) Fiber-coupled halogen light. The inset is a micrograph of the capillary tip.

(a) Overview

(b) Sensing tip

Figure 4.3: Micrograph of the S-TOP.
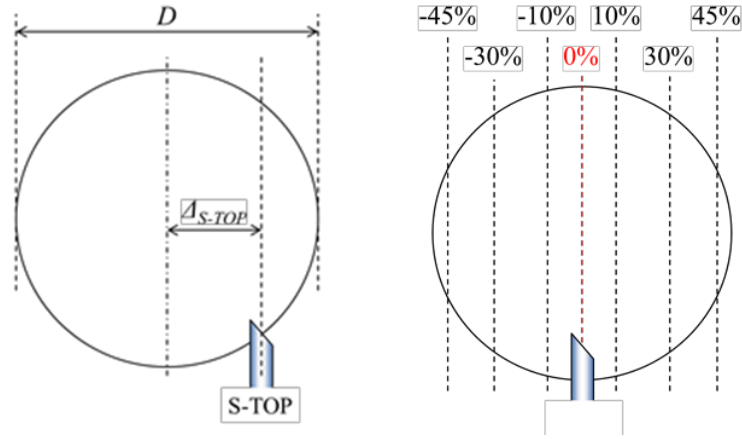
Figure 4.4: Conditions of the piercing position. The touch positions are defined as $\Delta_{S\text{-}TOP}/D$ ($\Delta_{S\text{-}TOP}$: the distance from the droplet's axis to the touch position, D: the droplet diameter).

Results of U_D and L_D   Figure 4.5 shows output signals obtained from the measurements and corresponding images. Table 4.1 lists the measurement results for droplet velocities and pierced chord lengths. These signals were similar; however, the measured chord lengths were very different. This is because of underestimation of U_D and residence time due to the eccentricity of piercing. U_D is calculated by Eq. (4.2), the product of α'_{Gas} and g'_{rd}. α'_{Gas} is obtained by the quasi-piercing experiment in Fig. 2.13, however, this experiment does not consider the angle of the interface against the S-TOP. That is, when the S-TOP pierces the interface inclined at certain angle (the S-TOP pierces outer region of the droplet), g'_{rd} is underestimated than it should be. According to Table 4.1, this effect causes over 50% underestimation of U_D when $\Delta_{S\text{-}TOP}/D > 30\%$. Moreover, $(t_{e,BP} - t_s)$ geometrically underestimates the residence time than it should be when the pierced position is away from

the center region. This uncertainty also causes over 20% underestimation (=[$\tau_{camera@0\%}$ - $\tau_{camera@30\%}$]/$\tau_{camera@0\%}$ in Table 4.1(c)) when $\Delta_{S\text{-}TOP}/D > 30\%$. The brackets in Table 4.1(b)(c) are corrected by $t_{e,pos}$. The results are in good agreement with visualization where the post-signal is obtained.
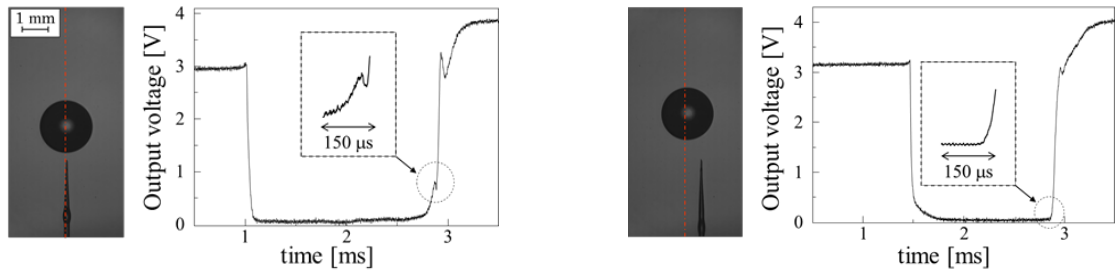
(a) Center region ($\Delta_{S\text{-}TOP}/D = 0\%$)   (b) Outer region ($\Delta_{S\text{-}TOP}/D = 30\%$)

Figure 4.5: Output signals in the experiment

Table 4.1: Difference in measurement results of the S-TOP and visualization

(a) Velocity measurements

Touch position [%]		0	5	10	30	45
Velocity [m/s]	S-TOP	1.03	1.03	0.93	0.46	0.32
	Camera			1.03		
Diff. [%]		< 1	< 1	10.1	55.6	68.6

(b) Size measurements

Touch position [%]		0	5	10	30	45
Pierced length [mm]	S-TOP	1.86 (1.91)	1.88 (1.92)	1.67	0.73	0.30
Minor axis length [mm]	Camera		1.92			
Diff. [%]		3 (< 1)	2 (< 1)	12.7	61.6	84.4

(c) Residence time τ. The values in brackets are ($t_{e,pos} - t_s$), otherwise ($t_{e,BP} - t_s$). τ_{camera} is obtained by the picture analysis (Vejrazka 2012)

Position	0	5	10	30	45
τ_{probe} [ms]	1.81 (1.86)	1.81 (1.85)	1.80	1.59	0.92
τ_{camera} [ms]	1.85	1.85	1.79	1.45	0.77
Diff. [%]	2 (< 0.1)	2 (< 0.1)	0.5	9.6	19.8

Post-signal threshold method   Experimental results of the relationship between the post-signal intensity and the touch position are plotted in Figure 4.6. The post-signal clearly reached a peak around the center region ($\Delta_{S\text{-}TOP} / D < 5\%$). Under the other conditions, post-signals were not detected. This fact accorded with the intensity distribution of post-signals numerically simulated (Figure 4.7). Apparently, the post-signal sharply peaks at the center region and decreases rapidly with shifts toward the outer region.
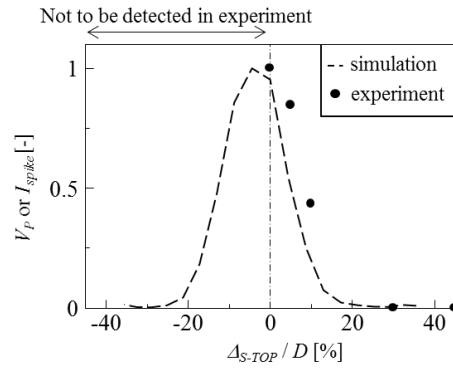
Figure 4.6: Relationship between the post-signal intensity and touch position (V_P is a normalized post-signal intensity).
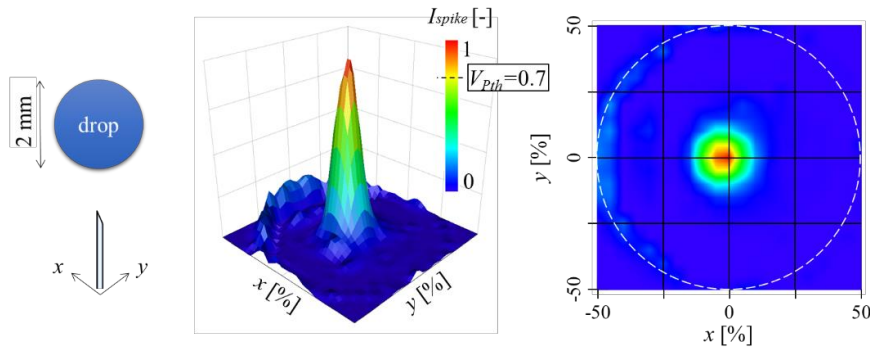
Figure 4.7: Intensity distribution of the post-signal using the 3D ray-tracing simulation.

The reason why the post-signal intensity appears only when the S-TOP touches the center region of a droplet is explained geometrically. Figure 4.8 (a) is a numerical result of the spatial distribution of light energy of discharged beams from the S-TOP tip to the surrounding water. The discharged beams have directional characteristics against the S-TOP axis. When the S-TOP touches a droplet interface almost perpendicularly, as shown in Figure

4.9 (b), beams reflected at the interface are effectively collected. On the other hand, the beams are immediately reflected off of the S-TOP axis when the interface inclines (i.e., the pierced position moves from the center region) (Figure 4.9 [c]). These tendencies can be applicable to spheroidal droplets.

(a)   (b)   (c)
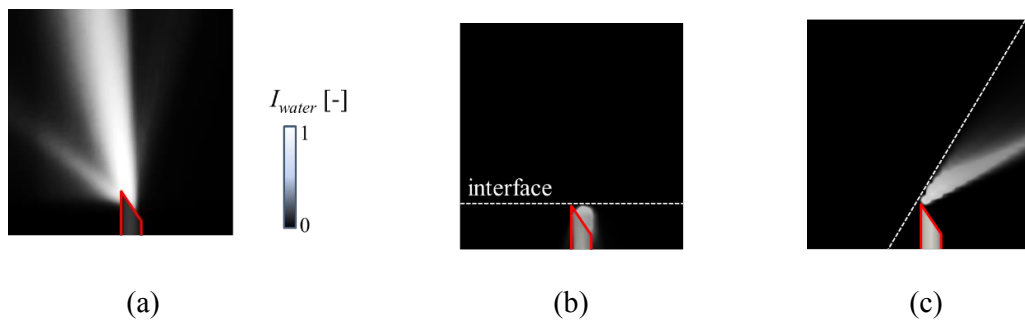
Figure 4.9: Intensity distribution of the discharged beams from the S-TOP tip to surrounding water (I_{water} is a normalized discharged beam intensity), and reflection off the inner interface of the droplet

The asymmetry of the I_{spike} (Fig. 4.6 and 4.7) distribution is due to the asymmetry of the discharged beams' direction. I_{spike} of experiment shows a good agreement with that of simulation in right-hand-side of Fig. 4.6. On the left-hand-side, any post-signals are not found in raw signals (Figure 4.10). It might be caused by the regional difference in surface deformation during penetration. Sakamoto has discussed the relationship of the form of the pre-signal and meniscus curvature around the S-TOP[37]. Once the S-TOP touches the interface from water to air normally, meniscus forms on the S-TOP tip uniformly. The discharged rays are scattered at the meniscus, then the amount of the return rays transiently decreases until the S-TOP staves the interface. When the surface hardly deforms (the interface is quickly

pierced), therefore, the amount of the return rays monotonically increase during the touching due to the surface reflection (Figure 4.11). The degree of the deformation must be the function of the impact angle on the local interface ϕ of Fig. 3.9.
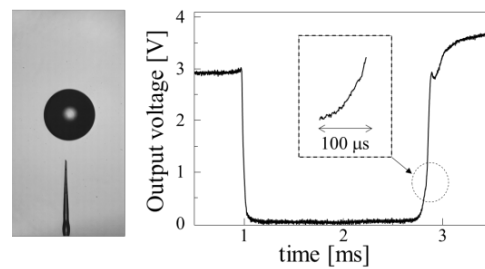
Figure 4.10: Output signal in the experiment at $\Delta_{S\text{-}TOP}/D = -5\%$

Anyway, above fact is preferable to distinguish the piercing condition. If the post-signal appears, we immediately know that the S-TOP has touched a droplet at the vicinity of its pole ($\Delta_{S\text{-}TOP}/D < 5\%$), and can calculate the droplet's velocity and diameter. Inversely, if no post-signal appears in an S-TOP signal, we can understand that the signal is insufficient for correct measurement due to an incomplete piercing condition and ignore the signal as null (post-signal threshold method, Figure 4.12).
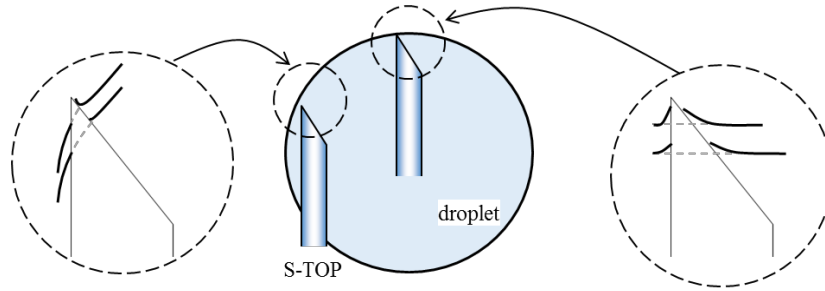
Figure 4.11: Sketch of the interface deformations during piercing. The interface deformation in left-region ($\Delta_{S\text{-}TOP} / D < 0\%$) is smaller than that in center region.
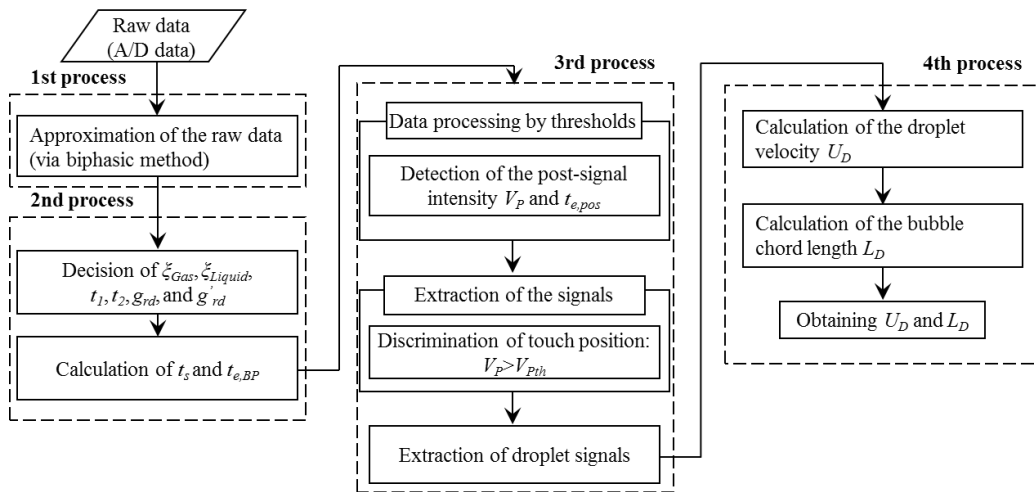
Figure 4.12: Flowchart of the post-signal threshold method.

4.3 Upcoming problem for the S-TOP

Spatial limit of the single-tip optical fiber probing Although measurement uncertainty due to the various piercing conditions are solved by the post-signal, the spatial resolution of the S-TOP approaches the limit in droplet measurement. It is usually no problem for the bubble measurement because the tip size of the S-TOP is sufficiently smaller than bubbles. However, the size of droplets from the spray nozzle, is distributed in a few dozen micrometers. This is a comparable size to the fine-drawn S-TOP tip. The spatial resolution of the S-TOP is evaluated in this section.

i) Sensor size L_{sensor}:   From a commonsence perspective, the S-TOP tip should be smaller than droplets. This is the simplest spatial limit of the S-TOP size. The sensor size can be defined by the tip diameter R_{tip},

$$L_{sensor} = R_{tip} / \sin \theta_w = 50\,[\mu m] \times 2 = 100\,[\mu m] \qquad (4.6)$$

ii) Latency length L^*:   To provide the validity of the optical fiber probe, a latency length, L^*, is first introduced by Cartellier (1990). In conformity to Cartellier's definition, L^* characterizes the length from the S-TOP tip inside liquid phase to ensure a signal decrease of the 20% of V'_{Gas}. If the sizes of droplets were less than L^*, the S-TOP could not detect the droplets clearly. This is very informative to think the spatial resolution of the S-TOP. Figure 4.13 graphically shows L^*, where I (the return light intensity distribution along the S-TOP tip in gas phase [Mizushima and Saito 2012]), V (the output value of the S-TOP), and h (the

76

distance from the S-TOP tip normalized by the wedge length).
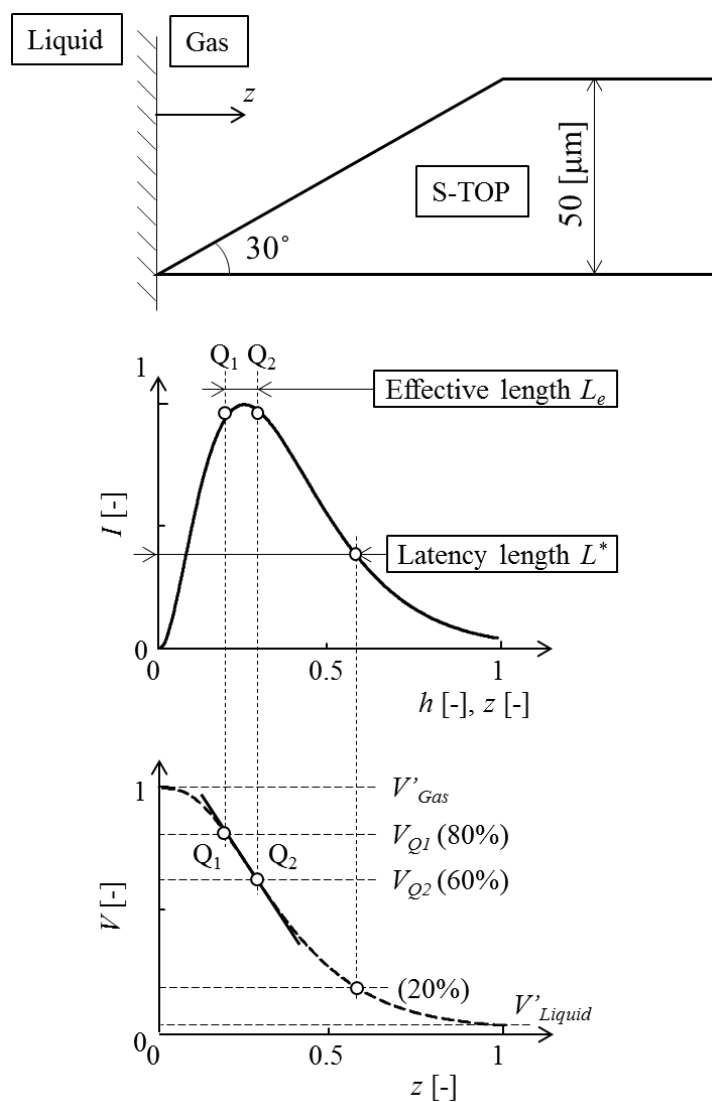
Figure 4.13: Schematic of a latency length L^* and an effective length L_s of the S-TOP.

x is the distance of the gas-liquid interface motion from the S-TOP tip. When *x* = 0, all over the tip is in the gas phase; hence the output value $V = V'_{Gas}$, where the V'_{Gas} is described as a sum of *I* in the *I-h* graph of Fig. 4.13,

$$V'_{Gas} = \int_0^1 I(h)\,dh \qquad (4.7)$$

When the interface moves through a distance of *x* from the S-TOP tip, the segment *x* along the tip is in the liquid phase; hence *V* is subtracted from V'_{Gas} as a function of *x*,

$$V(x) = V'_{Gas} - \int_0^x I(h)\,dh \qquad (4.8)$$

In Fig. 4.13, according to the definition of L^*, the signal decrease of the 20% of V'_{Gas} in the *V-x* graph corresponds to the 65% of the wedge length in the *I-h* graph; hence,

$$L^* = \left(50\,[\mu m] \times \sqrt{3}\right) \times 65\,[\%] \approx 56\,[\mu m] \qquad (4.9)$$

It indicates the spatial resolution of the S-TOP droplet measurement and must be smaller than the measurement object. In this study, L^* is small enough to measure the submillimetre droplets. L^* is also interpreted experimentally, through the coefficient α'_{Gas} (=56 [μm]). It means the length for detecting a gradient from V'_{Gas} to V'_{liquid}; therefore it equals to L^*.

iii) Effective length L_e: In addition to L^*, we newly introduce an effective length L_e. It

means the length over which the S-TOP provides most of the voltage change during the gas-to-liquid penetration. It is very important to determine g_{rd} and g'_{rd} for calculating the velocity accurately. In the *I-h* graph of Fig. 4.13, we consider a Q_1Q_2 segment that is the largest-*I* area (over 90% of I_{max}) in the S-TOP. In *V-x* graph of Fig. 4.13, the gradient from $V|_{Q1}$ to $V|_{Q2}$ (80% and 60% of V'_{Gas}) is exactly the largest in the output value. Here we define the Q_1Q_2 segment as an effective length L_e of the S-TOP.

Above limits are applicable to the 50-μm-tip, hence, one can see the limits can reduce more. However, the tip should be larger than 50 μm as long as the conventional optics is used. Figure 4.14 is the quasi-piercing experiment results of various tip sizes. According to this, α'_{Gas} of under 50-μm-tip becomes larger than that of the 50-μm-tip.
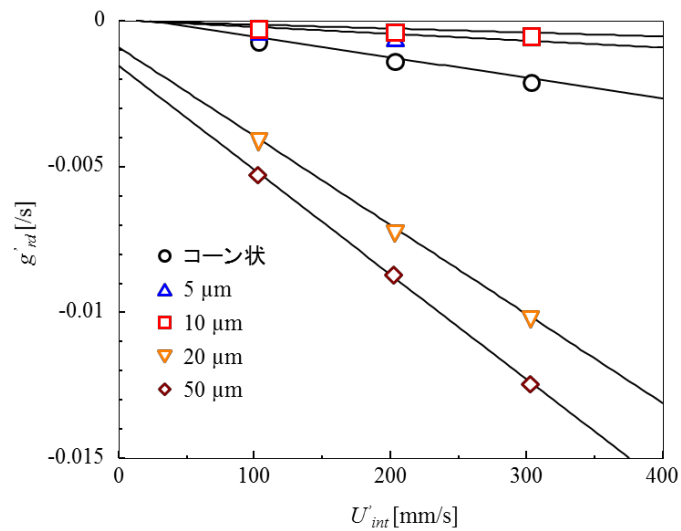
Figure 4.14: Quasi-piercing experiment by various tip size.
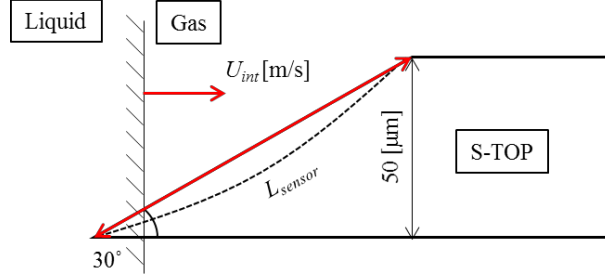
Figure 4.15: Quasi-piercing experiment by various tip size.

This is because of the lack of the sampling rate for the S-TOP's spatial resolution. As the tip size gets smaller, large sampling rate for photo-electric conversion is needed to obtain a true signal from the microscopic sensor (Figure 4.15). When the U_{int} is 10 [m/s] and representative length is L_{sensor}, required sampling rate N [Hz] is,

$$N \gg \left(U_{int} \times L_{sensor} \right) \Rightarrow N \gg 0.1\,[\text{MHz}] \tag{4.10}$$

In order to overcome this limit, Saito et al has invented a new type of the optical fiber probe micro-fabricated by the femtosecond pulse laser, Fs-TOP (Figure 4.16). It has two sensors on a single fiber, which is the tip of the S-TOP (sensor A) and micro-processed area near the tip (sensor B). When the Fs-TOP pierces the interface, a step-like signal is obtained. The time of the step is the interface velocity to pass from the sensor A across B. The Fs-TOP doesn't need to obtain its true signal, but we only have to detect the time at which the interface passes through the sensor A and B. In this context, the Fs-TOP measurement is free from the

optics-derived limitation, and hence the limit of the tip size can be reduced under 50 μm.

However, the processing mechanisms of the optical fiber through the femtosecond pulse laser is not clear. Therefore, the interaction of the water (transparent material) and femtosecond pulse laser is deeply studied in the next chapter.
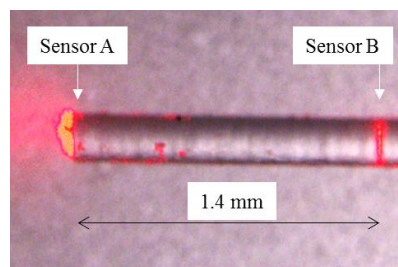
(a) Micrograph of the Fs-TOP with cylindrical tip. Light of LD (635 nm) is introduced from the other tip, then some of the light leaks at the sensor A and B.
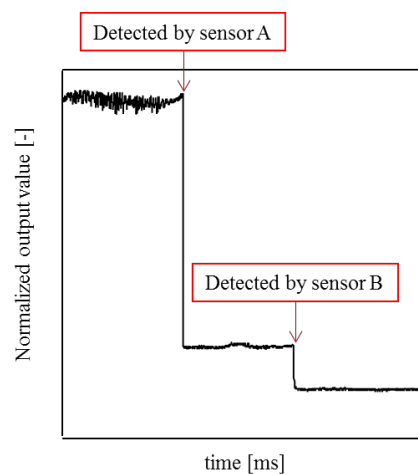
(b) Output signal from above Fs-TOP during gas-to-liquid penetration. The two declines are formed by the sensor A and B respectively.

Figure 4.16: Micrograph of the Fs-TOP and its typical signal.

5. Nonlinear bubble nucleation and growth following filament and white-light continuum generation induced by a single-shot femtosecond laser pulse into dielectrics based on consideration of the time scale

The inception, growth and dynamics of bubbles induced by short laser pulses, called optic cavitation, are very interesting targets for multiscale-ranging physics (e.g., Coulomb explosion, ablation and more) as well as advanced technologies (e.g., micromachining for metals and dielectrics, laser surgery, graphene production, etc.)[50–85]. Numerous reports of the laser processing of/in many substances (e.g., metal[50–56], dielectrics[57–68], biological tissues[69–78] and water[86–108]) under irradiation of various pulse durations from a few femtoseconds (fs) to nanoseconds (ns) have been published. Investigations focusing on bubble inception and growth with clear consideration for different time scales are still very rare even now. Lauterborn[86] observed the optic cavitation in water by optical breakdown induced by ns-laser pulses (pulse duration τ = 30–50 ns). Tomita and Shima[87] carefully visualized bubbles induced by 20-ns laser pulses in water in various pulse energy and boundary conditions (i.e., near a rigid/elastic boundary, convex rigid wall and free surface). Vogel et al.[100] extensively studied the dynamic processes of bubble formation in water induced by ns, picosecond (ps), and fs pulses. Although the laser-induced plasma and bubble collapse were discussed extensively, the nature and processes regarding bubble formation and growth in strict consideration of the time scale have not received adequate attention. Many researchers have reported fs-pulse-induced bubbles' formation and growth in water. First, extraordinary peak

power (larger than 10^{12} W/cm^2) invokes multiphoton ionization at the focal domain; second, the generated plasma expands quickly and results in the breakdown, followed by a shock wave; finally, the bubbles are formed by homogeneous nucleation when the temperature approaches the critical temperature. To clearly draw out the hidden characteristics of the fs-pulse-induced bubble and its physics, a comparison with ns-pulse-induced bubble formation is needed. This subject poses a question: "what is the dominant physics of fs-pulse-induced bubble formation?" In general, the interaction of the fs-pulse and a transparent material is well known as white-light continuum generation[109–115], which is invoked only by the nonlinear effects of the fs-pulse and must be a key difference from the ns-pulse.

In the present study, with close observation of the time scale, we propose an electron time scale and a molecular time scale. The electron time scale is simply indicated by the time order of τ of the fs-pulse, which directly contributes to the white-light continuum generation. The molecular time scale is described as on the order of a thermalization time[105] which promotes thermal/substance diffusion on the bubble interface dominantly. Thus, on the basis of the clear recognition of extremely wide time scales on the order of electrons (10^{-13} s) to the molecular order (10^{-6} s) through well-organized experiments, we scrutinized the time-evolution phenomena of the plasma, bubble nucleation, and bubble growth, which were induced by a single-shot fs-pulse into water, methanol and acetone. The fs-pulse-induced bubble is not ordinary optic cavitation; rather, it is nonlinear-optic cavitation. We present intrinsic differences in the dominant-time domain of the fs-pulse and ns-pulse excitation. Intriguingly, a mere hundred femtoseconds' excitation predetermines the size of the bubble appearing 100 nanoseconds after irradiation. In the fs-pulse excitation, the electron-timescale-physics completely determines the far-distant destiny of dielectrics.

83

5.1 Experimental setup

The experimental setup is shown in Figure 5.1 and 5.2. The fs-pulses (: 130 fs, mean wavelength: 810 nm; full width at half maximum [FWHM] of 10 nm) were generated from a laser system (Maitai and Spitfire, Spectra Physics) in 1-kHz repetition. An optical chopper (New Focus) and mechanical shutter (Vincent Associates) were synchronized with the laser system and a function generator (NF); thus a single-shot fs-pulse was exactly extracted. The pulse was always monitored on a photodetector (ET3500, Electro-Optics Technology) during every experiment. Being tightly focused via a focusing lens (EPI L Plan Apo 10x, NA = 0.28, f = 200 mm), the fs pulse was introduced into water (Milli-Q, Millipore), methanol and acetone (Wako Pure Chemical) in a quartz glass cell (Spectrophotometer Standard Cell, 1×1 cm^2, GL Science) that was degassed through the vacuum, reducing to less than 100 Pa. For the time-resolved visualization of the bubble formation and growth in the molecular-time domain, a spark-flash lamp (exposure time, 18 ns; NANOLITE, High-Speed Photo-System) was used for stroboscopic photography with a delay generator (DG645, Stanford Research Systems). Jitter-confirmed signals from a terminative photodetector and the lamp driver were recorded during the visualization and calculated for the estimation of the time delay after the fs-pulse irradiation. A well-known pump-probe method was also applied. The fs-pulse was split into a pump pulse and a probe pulse through a beam splitter. The pump pulse interacted with the liquid, and the probe pulse illuminated a side view of the interaction as background light. The difference in the light path lengths of the pump and probe pulses corresponded to the delay time of 1 ps per 300 μm. The difference was also monitored on the photodetectors during the visualization. The visualizations were achieved by using a CCD camera (pixel size 20 μm) and an objective lens (Z6APO with ×5.0 objective lens, Leica), giving the spatial

resolution of 2 μm. For the time-resolved measurements in the electron-time domain, the spatial distribution of continuum intensity was observed. Once an intense fs-pulse passes through any transparent medium, the pulse experiences a change (usually an increase) in the refractive index depending on the medium and pulse intensity ($\Delta n = n_2 \times I$, with the non-linear refractive index n_2 and intensity I), and it causes a lens-like effect that tends to focus the laser beam inside the medium by itself (self-focusing)[61]. At the same time, the spectrum is quickly expanded from the center wavelength (self-phase modulation). These nonlinear effects result in the generation of a white-light continuum, with micro-plasma channels formed along the optic axis as a wake (filamentation[115-122]). The continuum generation is driven by electron excitation during the fs-laser irradiation, which means that one can extract the interaction between the laser pulse and electrons in the electron-time domain through observation of the continuum. The continuum had never been verified with the bubble formation as beyond comparison in time scale, although the continuum generation is the most dominant event for the fs-pulse rather than the resultant shock wave generation. In order to clarify the continuum's contribution to the bubble formation, we measured its intensity distribution along the optic axis at which the bubble arises. Confocal optics (collecting lens: NA = 0.56, pinhole aperture: 10 μm in hole dia., Fig. 1) were newly developed and employed for this specific purpose. A 775-nm short-pass filter (Bright Line, Semrock) was inserted in front of a photomultiplier (R3809, Hamamatsu Photonics), detecting the continuum. This confocal system was moved in parallel to the optic axis of the fs-pulse.
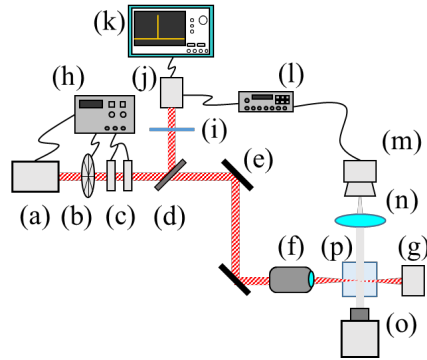
Figure 5.1: Schematic of the ns-flash photography. (a) fs-laser system, (b) optical chopper, (c) mechanical shutters, (d) half mirror, (e) mirror, (f) objective lens, (g) photo detector 1, (h) function generator, (i) ND filter, (j) photo detector 2, (k) oscilloscope, (l) delay generator, (m) flash lamp, (n) collecting lens, (o) camera, and (p) quartz cell.
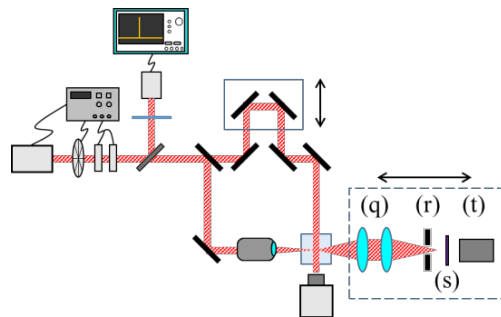
Figure 5.2: Schematic of the pump-probe method and confocal measurement. (q) objective lens, (r) pin-hole, (s) short-pass filter, and (t) photomultiplier.

5.2 Result and discussion

Figures 5.3 and 5.4 show visualized bubble and its axes generated in water/methanol/acetone with a laser pulse of 130-fs duration and 0.6-μJ pulse energy. The fs-pulse is irradiated from the left-hand side of the picture in Figure 5.3. Figure 5.5 is a dimensionless representation of Figure 5.4.
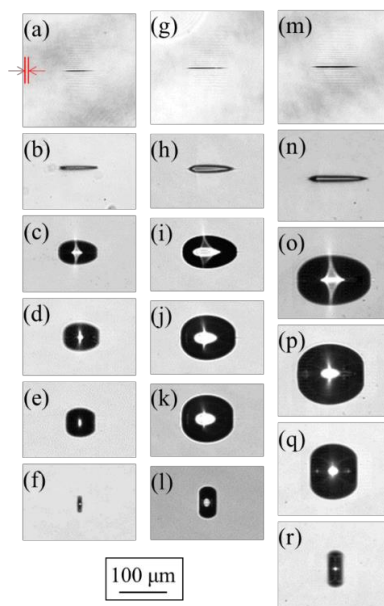
Figure 5.3: Images visualized via the pump-probe method and stroboscopic photography. The optical or electrical delay times were (a) 400 ps, (b) <0.1 μs, (c) 1.1 μs, (d) 2 μs, (e) 3 μs, and (f) 4.5 μs in water; (g) 400 ps, (h) <0.1 μs, (i) 1 μs, (j) 2.5 μs, (k) 3.4 μs, (l) 6.5 μs in methanol; (m) 400 ps, (n) <0.1 μs, (o) 2.2 μs, (p) 5 μs, (q) 8 μs, and (r) 10 μs in acetone. Arrows in (a) indicate the linear-focus and its depth of the objective lens.
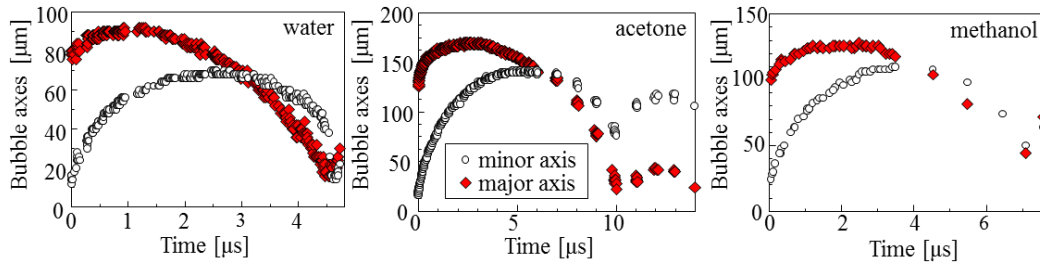
Figure 5.4: Time-series bubble axes generated in water, methanol and acetone.

During expansion, a photo-ionized portion of the liquids changed from non-equilibrium-plasma- to gas-phase. The ablation-derived phase transition dominated the bubble growth, although the surface tension and viscosity did not contribute much to this phenomenon[98]. The gas diffusion from the liquid into the bubble was negligibly small[92, 95, 101], and thus thermal and substance diffusion did not have any significant effect on the bubble growth. Consequently, only the number density of the molecule provided an essential difference in the water/methanol/acetone bubbles. This is also revealed in Figure 5.5 in a different manner; i.e., at $t^* < 5\times10^{-7}$ both of the time rates of change are quite similar; here, $t^* = t / \{R_{max} \times (\rho / p_\infty)^{0.5}\}$ with time t, maximum bubble axes of the bubble R_{max}, liquid density ρ, and atmospheric pressure p_∞ (= 1013 hPa). Despite this result, the maximum equivalent-diameter of the bubble in acetone is twofold larger than that in water by means of the same pulse energy. Interestingly, the ns-pulse-induced bubbles are quite spherical, and their diameters are almost the same under the same irradiation power[98]. Assuming that the bubble contents are almost vapor and the mole numbers and temperature are almost constant at this time scale the minus-third power of the maximum bubble size (volume) is proportional to the vapor pressure from the state equation. The vapor pressure ratio $P_{v,ratio}$ of acetone to water

and the radius ratio r_{ratio} of acetone to water are plotted in Figure 5.6 against the temperature; here $P_{v,ratio} = P_{v,acetone}/P_{v,water} \approx (1/[r_{acetone}/r_{water}])^3 = (1/r_{ratio})^3$. According to this, an $r_{ratio} > 2$ corresponds to room temperature and an $r_{ratio} \approx 1$ corresponds to >500 K. The temperature and vapor pressure of the acetone/water bubbles under the ns-pulse irradiation reach extremely large values because of intense thermalization during the ns-pulse irradiation[61, 101]. Thus, if anything, the thermalization effect reaches a saturation state against the bubble size in both acetone and water ($r_{ratio} \approx 1$). The temperature under the fs-pulse irradiation is small[104]; thus, as shown in Figure 5.6, the difference observed in the bubble size between acetone and water was large.
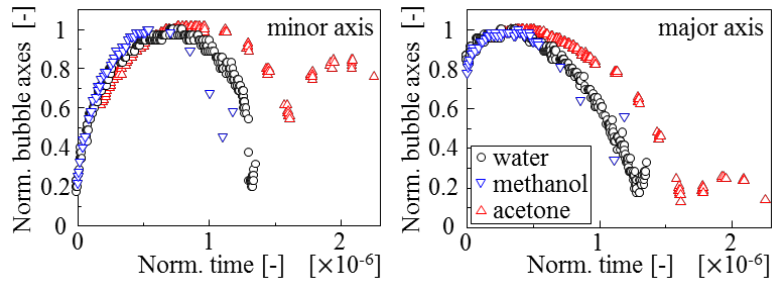
Figure 5.5: Normalized time-series bubble axes. $R^* = R/R_{max}$ with axes length R and maximum axes length R_{max}.
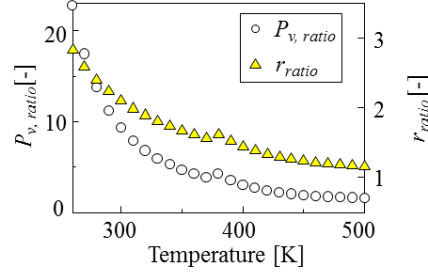
Figure 5.6: Ratio of vapor pressure of acetone[124]/water[125, 126] at arbitrary temperatures (left *y*-axis). The ratio of the equivalent bubble radii of acetone/water was estimated by the state equation (right *y*-axis).

Before the bubble is generated, non-linear effects (self-focusing and self-phase modulation), filamentation, and optical breakdown coexist from the femtosecond to sub-nanosecond domains. Once the intense fs-pulse over the critical threshold ($P_{cr} = 3.72 \, \lambda^2 / 8\pi n_0 n_2$, with the laser wavelength λ and the refractive index n_0) is involved in the self-focusing, the molecules or atoms in the irradiated area reaching 10^{13}–10^{14} W/cm^2 are excited and rapidly ionized (multiphoton ionization) due to its strong fluence, and some of the pulse energy is consumed[62]; increased electron density causes a decrease in the refractive index[123], and then the converging fs-pulse tends to diverge. If the pulse energy is high enough to cause the self-focusing, the fs-pulse converges by itself again; thus the plasma channel, i.e., filament, is formed as a wake and the spectrum of the fs-pulse largely changes into a white-light continuum[109-114]. Optical breakdown ($\rho_e \geq 10^{18}$ /cm^3) with electron density ρ_e[118]

then begins in the filament with the plasma expansion. Finally, the bubble is generated in the part of the filament within 100 ns from the fs-pulse irradiation[98].

At the initial state shown in Figure 5.3, the ratio of the length of the bubble along the optic axis (L_b) in the liquids is, $[L_{b,water}]$:$[L_{b,methanol}]$:$[L_{b,acetone}]$ = 1.0:1.3:1.6. Even the phase transition is of less importance in this time domain. The bubbles appear around the mid-point of the filament in which $\rho_e \geq 10^{18}$ /cm³; hence L_b elongation derives from the filament elongation. Figure 5.7 shows the blue-shift continuum intensity distribution along the optic axis of the fs-pulse. The peak-shifts coincided with the filament elongations because the confocal system effectively collected the fs-pulse at its diverging end-point (the edge of the filament). The difference in the linear index of refraction for the liquids are less than 3% (1.33 [water] and 1.36 [acetone])[127], hence; the shifts by the linear index are not so considerable. The filament elongation depends on the pulse energy and the bandgap of the medium[114]. The peaks exactly shift frontwards of the fs-pulse with the increase in the pulse energy. In addition, the peak in acetone is at a deeper position from the entrance compared to that in water because of the difference in bandgap. When the bandgap is low, the filament tends to be long because the low-bandgap material can be easily ionized by low fluence[114] along the optic axis. The high-ρ_e area in the filament of the low-bandgap materials, therefore, is elongated as well; hence, the ratio of the bandgap directly equals the ratio of L_b. In fact, the bandgaps of acetone[128, 129], methanol[114] and water[130] are 4.8, 6.0 and 7.8 eV, respectively. The continuum generation occurs during τ (= 130 fs) or less. That is, L_b is already determined in the electron-time domain, which is significantly earlier than the bubble appearance.
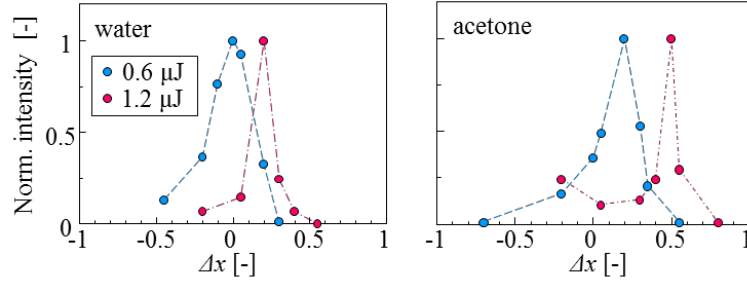
Figure 5.7: Blue-shift continuum intensity distribution along the optic axis of the fs-pulse in water and acetone. The position at which the intensity of 0.6-μJ fs-pulse peaks in water was set as $\varDelta x = 0$.

The fs- and ns-pulse excitations are different with each other, in terms of the ionization mechanism[57], the plasma temperature[63], and the bubble behavior including its inception. Different excitation processes surely make different bubble dynamics; in the ns-pulse irradiation, therefore, the bubble expands spherically due to its high excitation temperature confined to the linearly focused portion, which results from the strong ion excitation (which is called optic cavitation). On the other hand, in the fs-pulse irradiation, the bubble shape is oblong ellipsoidal, and it expands weakly due to the dominance of non-linear effects resulting from the intensive electron excitation; we call this nonlinear-optic cavitation. The ultra-short-pulse-induced bubble formation should be classified by the dominant physics. In the fs-pulse irradiation, electron-time domain physics completely characterizes the far-distant bubble generation and dynamics in dielectrics.

92

5.3 Concluding remarks for fs-pulse induced bubble formation

We investigated the very widely-ranging physics appearing in a nonlinear-optic cavitation based on carefully time-resolved experiments. The fs-pulse-induced bubble inception and its growth in water/methanol/acetone showed a shape and size that are clearly different from those created by the ns-pulse. We also directly measured the blue-shift continuum by using a confocal system. We observed that the fs-pulse elongation due to the differences in bandgap. This elongated trace of the fs-pulse makes the filament that confines high electron number-dense areas; thus an elongated bubble is formed. This elongation corresponds to the length of the bubble along the optic axis, L_b, and the ratio of L_b in the liquids is approximately equal to their bandgap ratio. These nonlinear effects occur because the electron-time domain is most featured through the dominant electron excitation by the fs-pulse. That is, in the fs-pulse irradiation, the electron-time-scale physics nucleate bubbles temporally beyond a six-order-of-magnitude difference.

Nomenclature of the femtosecond pulse laser part

f	focal length (mm)
I	intensity of the laser pulse (W)
L_b	length of the bubble along the optic axis
$L_{b,acetone}$	length of the bubble along the optic axis in acetone
$L_{b,methanol}$	length of the bubble along the optic axis in methanol
$L_{b,water}$	length of the bubble along the optic axis in water
n_0	linear refractive index (-)
n_2	nonlinear refractive index (-)
p_∞	atmosphere pressure (Pa)
P_{cr}	Critical power of self-focusing (Pa)
$P_{v,acetone}$	vapor pressure of acetone (Pa)
$P_{v,water}$	vapor pressure of water (Pa)
$P_{v,ratio}$	vapor pressure ratio (-)
$r_{acetone}$	bubble radius in acetone (mm)
r_{water}	bubble radius in water (mm)
r_{ratio}	radius ratio (-)
R	size of bubble (mm)
R^*	normalized size of bubble (mm)
R_{max}	maximum size of bubble (mm)
t	time (s)
t^*	normalized time (-)

Δn	amount of change in a refractive index (-)
Δt_{s2}	allowance of t_{s2} detection (s)
Δx	shift from the peak in water (-)
λ	wavelength (nm)
ρ	density (g/cm^3)
ρ_e	electron density (g/cm^3)
τ	duration of the laser pulse (s)

6. Extensive study of original micro-process by femtosecond laser for fine-droplet measurement via Fs-TOP

6.1 Droplet measurement by using the Fs-TOP

The S-TOP and Fs-TOP have different properties compared with the other conventional probes. Furthermore, these probes have different characteristics owing to the difference of measurement principles and the way of manufacturing. The S-TOP can be made very easily; the tip of the S-TOP is ground into the wedge-shape. Hence, the wedge-shaped tip is gradually covered with the other phase as shown in chapter 2. Micro-fabrication of the Fs-TOP is conducted through the femtosecond pulse (fs) laser (Figure 6.1). The width/depth of the groove is decided depending on the size of the measurement objectives. It is important to use intelligently the fs-laser based on understanding of the processing techniques. There are not so many reports for processing of the optical fiber by the fs-laser. In this chapter, therefore, the fs-laser processing is studied. Figure 6.2 shows the schematic diagram of measurement process by using the Fs-TOP. As is discussed in the chapter 5, the S-TOP measures the velocities of bubbles/droplets by very small tip. Hence, the S-TOP needs the fast A/D converter and fast amplifier for the measurements of tiny bubbles/droplets moving at high velocity. This is the limit of S-TOP measurement. Therefore, the measurement object of the S-TOP is the sub-mm droplet moving less than several m/s, at best. On the other hand, the Fs-TOP uses the signal from its tip and that from the groove. Hence, the time interval of the event time becomes larger than that of S-TOP. Thanks to this, the measurement object of Fs-

TOP can be the micro-droplet and sub-mm droplet moving at over 10 m/s or more.
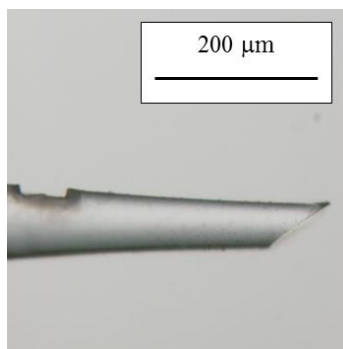
Figure 6.1: Micrograph of the Fs-TOP with wedge-shaped tip.
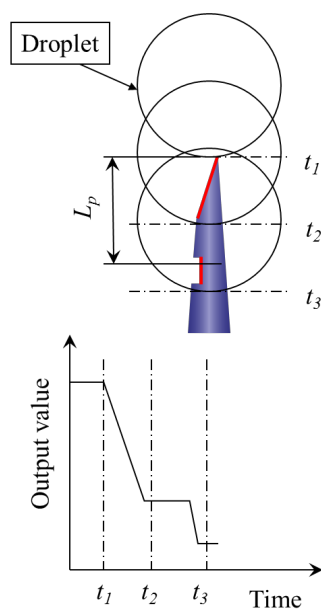
Figure 6.2: Schematic of the Fs-TOP measuring a single droplet.

The optics is shown in Figure 6.3. The beam from a laser diode (1) (wavelength 635 nm) is split by beam splitter (2), and focused on the fiber edge (4) by objective lens (3). A part of the laser beam propagated through the optical fiber is reflected at the other tip (sensing side) of the optical fiber probe, and propagated back again through the same fiber; then it is input into a photo multiplier (6) through a polarizer (5) cutting direct laser beam from the laser diode. The optical signal is converted into an electrical signal via photo multiplier (6). The electrical signal is stored in digital oscilloscope (8).
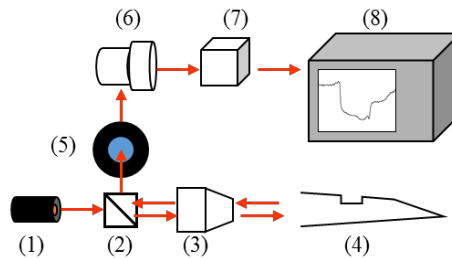
Figure 6.3: Optics for the Fs-TOP. (1) Laser diode, (2) Beam splitter, (3) Objective lens, (4) Fs-TOP, (5) Polarizer, (6) Photo multiplier, (7) Amplifier, and (8) Digital oscilloscope.

The typical output signal of the Fs-TOP measuring tiny droplet is indicated on Figure 6.4. At first, the end-tip is covered in the droplet, then the output signal decreases; second, the fabricated groove is also covered, then the signal decreases even further; and thus the step-like signal is formed. The end-tip shapes wedge, hence the post-signal can be clearly shown when the tip is exposed to the air (Fig. 6.4(2)). The droplet velocity U_D and pierced chord length L_D are obtained by each event time of t_s, t_{s2}, and $t_{e,pos}$,

98

$$U_D = \frac{L_P}{\left(t_{s2} - t_s\right)} \qquad (6.1)$$

$$L_D = U_D \times \left(t_{e,pos} - t_s\right) \qquad (6.2)$$
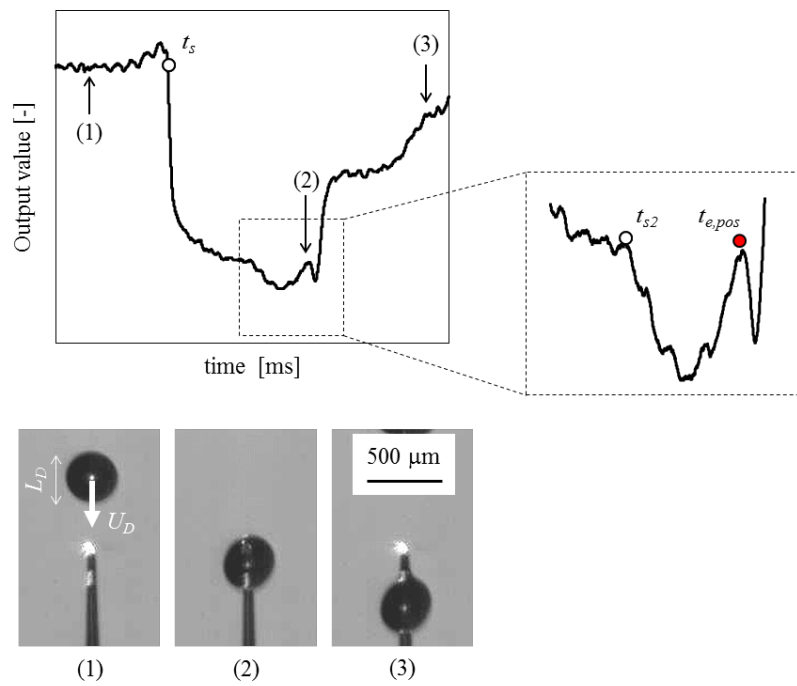
Figure 6.4: Typical output signal of the Fs-TOP of tiny droplet measurement.

6.2 **Laser-induced non-equilibrium plasma processing**

In this section, the procedures for fabricating the micro-groove and an experiment in terms of the processing atmosphere is introduced. The schematic of the femtosecond laser processing is shown in Figure 6.5. The power of the fs-laser is adjusted with ND filters beforehand. The beam splitter (c) splits evenly 2 ways, and the output of the power meter (h) indicates the power of the irradiation directed to the optical fiber (f) through the objective lens (e) (Mitutoyo Plan Apo Infinity Corrected Long WD Objective series). The beam splitter is also used for visualization at the focus position of the objective lens (e) by using CCD (i) and monitor (j). The focal position is observed by the He-Ne laser (k) as a light source, then the fs-laser is irradiated to the targets.
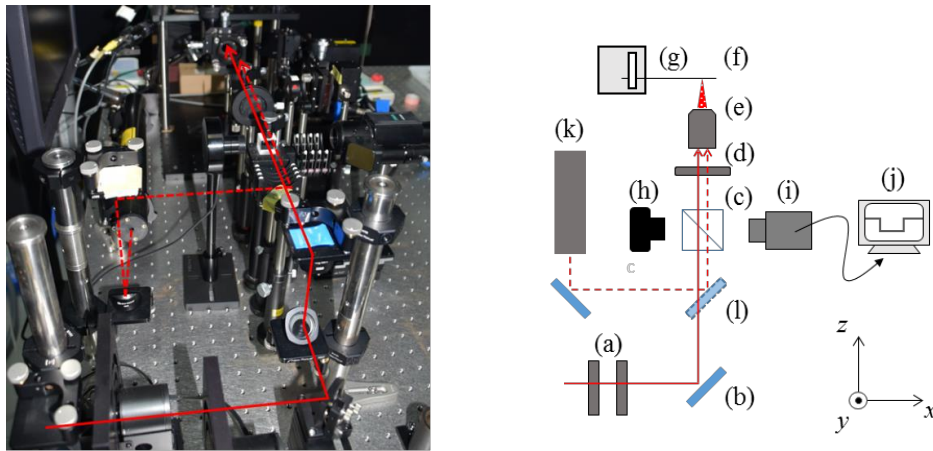
Figure 6.5: Fs-laser fabricating system. (a) shutters, (b) mirror, (c) beam splitter, (d) iris, (e) objective lens, (f) optical fiber, (g) 6-axis stage, (h) optical power meter, (i) CCD camera, (j) monitor, (k) He-Ne laser, and (l) removable mirror. The solid line and broken line are the light paths of the fs-laser and He-Ne laser.

Once the fs-laser beam (1 kHz) is focused, the focal point sequentially forms non-equilibrium plasma. An optical fiber is fixed by the fiber-base on the 6-axis stage, and we make it pass over the focal point as depicted in Figure 6.6. The fabrication procedure is only 2 steps: i) tip size decision, i.e., unnecessary portion of the fine-drawn tip of the optical fiber is removed (Fig. 6.6[b]); and ii) grooving. In terms of the grooving, the travel distances along *y*-axis and *x*-axis determines the depth and width of the processed area. The depth of the groove contributes to the output level of sensor B and the width affects water drainage (or wettability) on the sensor B (Matsuda 2010). These numbers deeply relate to the shape of the output signal and determine whether the event times can be found easily or not. The other parameters exist in a fabrication procedure.

When the fs-pulse at certain pulse energy is focused into the medium, micro-plasma channel (filament, in chapter 5) is quickly formed along its optic axis (*z*-axis of Fig. 6.5 and 6.6). The lateral body of the optical fiber is exposed to the filament, like a hot wire foam cutter. One can see its length indicates the depth of the processing. There are so many requirements for optimizing these processes; NA (numerical aperture) of the objective lens, pulse energy and repetition rate of the fs-laser, moving velocity of the stage, shape of the groove, material of the optical fiber, atmosphere of the processing and so on.

In this thesis, the atmosphere of the processing is focused. The nonlinear bubble formation in water, studied in the chapter 5, is driven by the plasma formation in liquid phase. This kind of plasma might newly process the fiber in different fashion from conventional processing that is conducted by the plasma in gas phase. The schematic of this experiment is shown in Figure 6.7 and its conditions are indicated in Table 6.1.
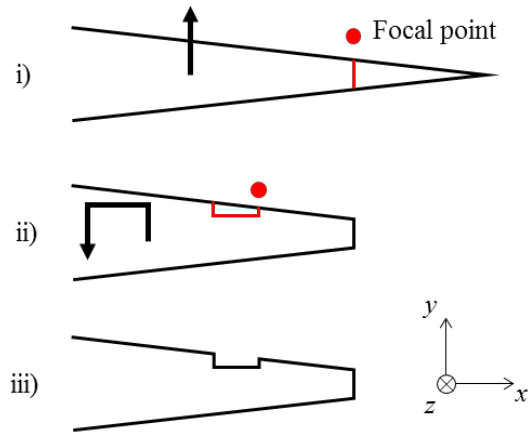
(a) Fabrication procedure.

(b) Monitored images from i) to ii) by the CCD camera (f)

Figure 6.6: Details of the processing and corresponding images.
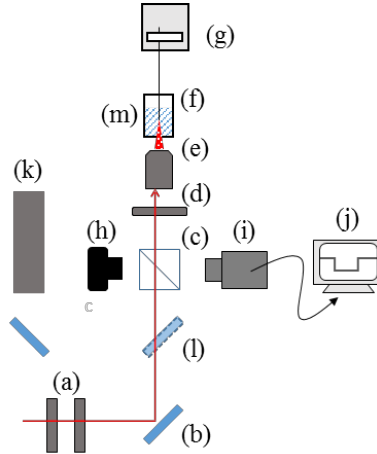
Figure 6.7: Experiment for fs-laser processing in water. (a) shutters, (b) mirror, (c) beam splitter, (d) iris, (e) objective lens, (f) optical fiber, (g) 6-axis stage, (h) optical power meter, (i) CCD camera, (j) monitor, (k) He-Ne laser, (l) removable mirror and (m) quartz cell filled with Milli-Q water.

Table 6.1: Conditions of fs-laser processes in air/water atmosphere.

NA	Pulse energy	Repetition rate	Processing velocity	Shape of the groove	Atmosphere
0.14, 0.28, 0.42, 0.55	34.7, 18.1, 9.3, 4.5, 1.5 mW	1 kHz	5 μm/s	depth: >10 μm, width: 50 μm	Air (1 atm) and water

6.3 **Result and discussion**

Visualization result by using SEM The SEM images at respective grooves are shown in Figure 6.8-15. Every groove is processed in accordance with Fig. 6.6(a), but there are incompletions in some conditions. In terms of the groove-shapes processed in air, the depth of processing highly depends on the pulse energy (the fs-laser cannot pass over the diameter of the fiber when the pulse energy becomes small). The edge near the laser directed surface shapes round, and the opposite surface has a lot of cracks. The round shape is caused by a trajectory of the fs-pulse focusing. In Fig. 6.11, this effect can be seen clearly in the conditions of the large pulse energy; the irradiated area is largely gouged and processed area narrows along the optic axis. After the neck position of the focal point, the radius of the focused pulse gradually expands, and the latter part of the processing is formed. This is an evidence of the nonlinear propagation of the fs-pulse in air, and the cracks apparently exists deeper than the focal positions. These cracks might be caused by local thermal effect, anyway, such defective part must contribute to undesired noises of the Fs-TOP.

The shape of the grooves processed in water, on the other hand, the cracks are not observed. In addition, the processing depths are not so different with each pulse energy. This is also the evidence of the nonlinearity of the fs-pulse studied in the previous chapter. The nonlinear refractive index of water is 6-times larger than that of air, that is, the filament in water can be longer than that in air because the filament formation is a function of the nonlinear refractive index. This is good for ensuring the processing depth. However, the processed area is like a ragged hollow. Considering the presence of the bubbles along the filament, their expanse and collapse must take a dominant role for processing. The parts of the edge seems to be peeled by some operations other than the fs-laser (between [2] and [3]

of Fig. 6.13).

In order to validate the grooves, the output signal of the interface piercing (Fig. 2.13) is compared. Figure 6.16 and 17 shows the result of the Fs-TOP under test. Both signals indicate the interface detection of sensor B (processed area) in a same temporal-axis. The velocity of the Fs-TOP is 1.5 mm/s (quasi-static), however, output signal of the Fs-TOP processed in water sharply decreases. This is remarkable advantage for signal processing to detect t_{s2}. The fall time of the slopes should be short otherwise t_{s2} might be decided within the long-allowance Δt_{s2}. Considering Δt_{s2} ratio of both probes, the Fs-TOP processed in water successfully shows an 85% improvement for this uncertainty. The optimization of the processing is halfway to the precise measurement for fine-droplets by using the Fs-TOP; however, the fs-laser processing must bring out possibilities of the optical fiber probing.
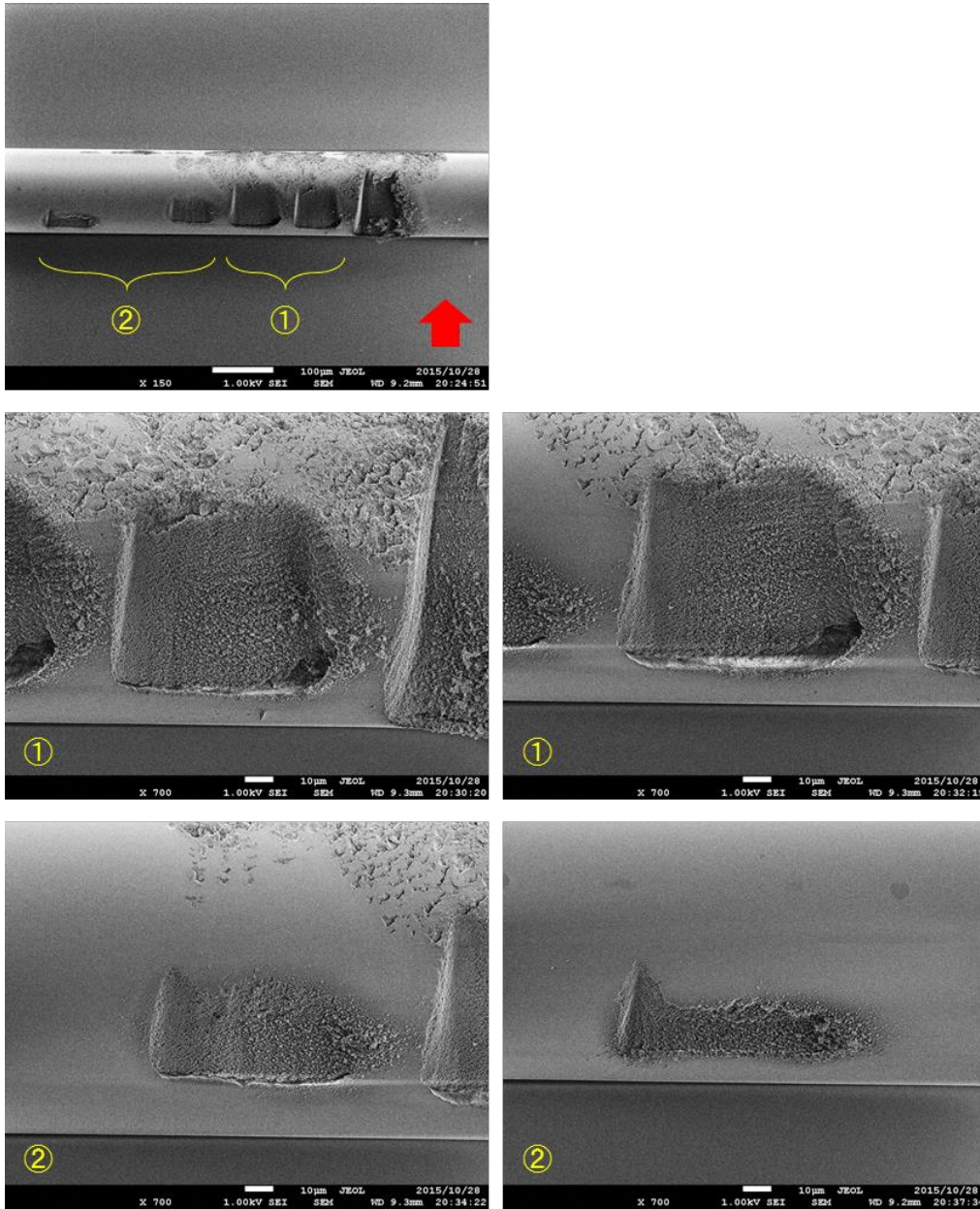
Figure 6.8: Processed in air, NA = 0.14, pulse energy: 1) 34.7 and 2) 18.1 mW,

respectively. The red arrow indicates the direction of the fs-laser.
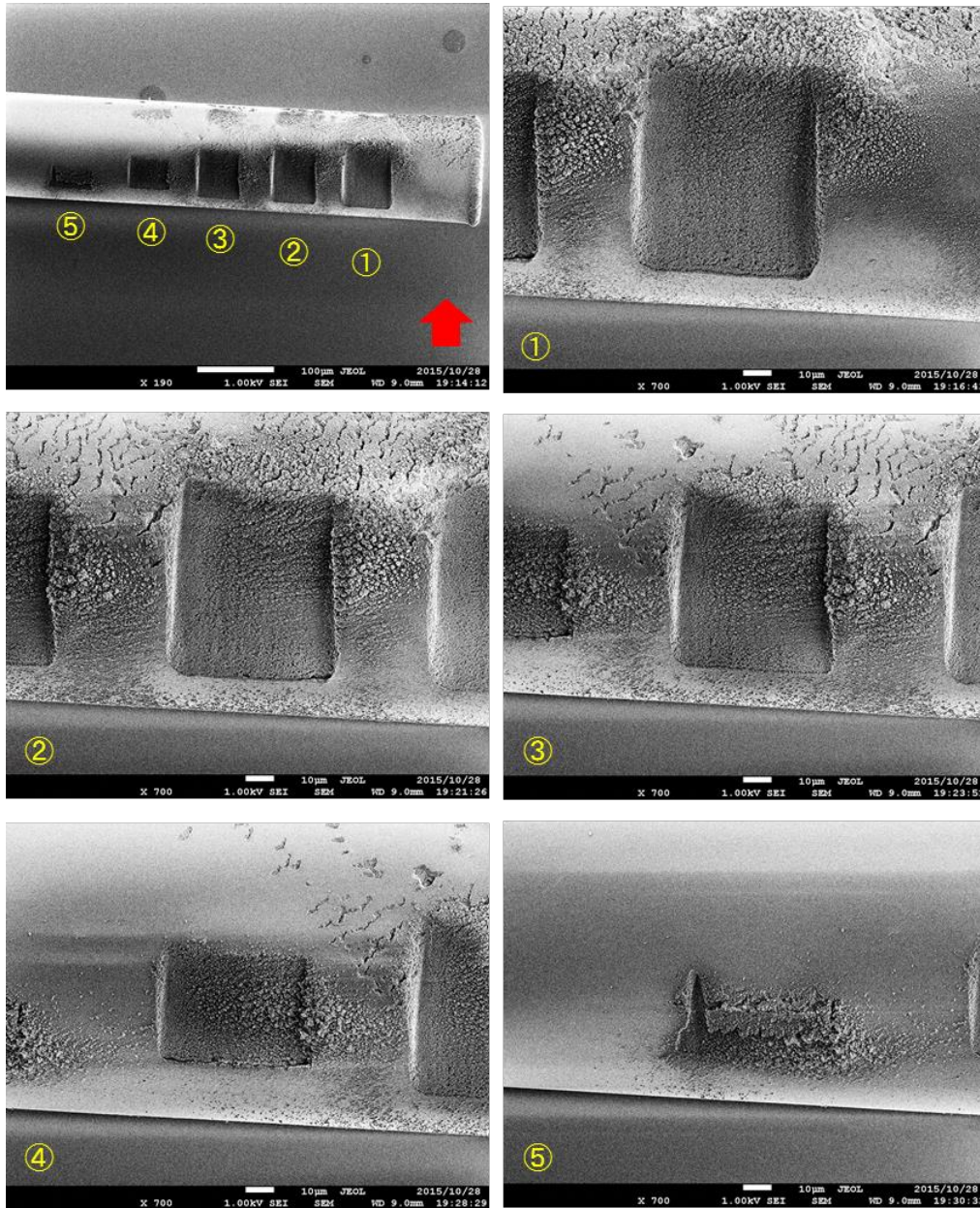
Figure 6.9: Processed in air, NA = 0.28, pulse energy: 1) 34.7, 2) 18.1, 3) 9.3, 4) 4.5, and

5) 1.5 mW, respectively. The red arrow indicates the direction of the fs-laser.
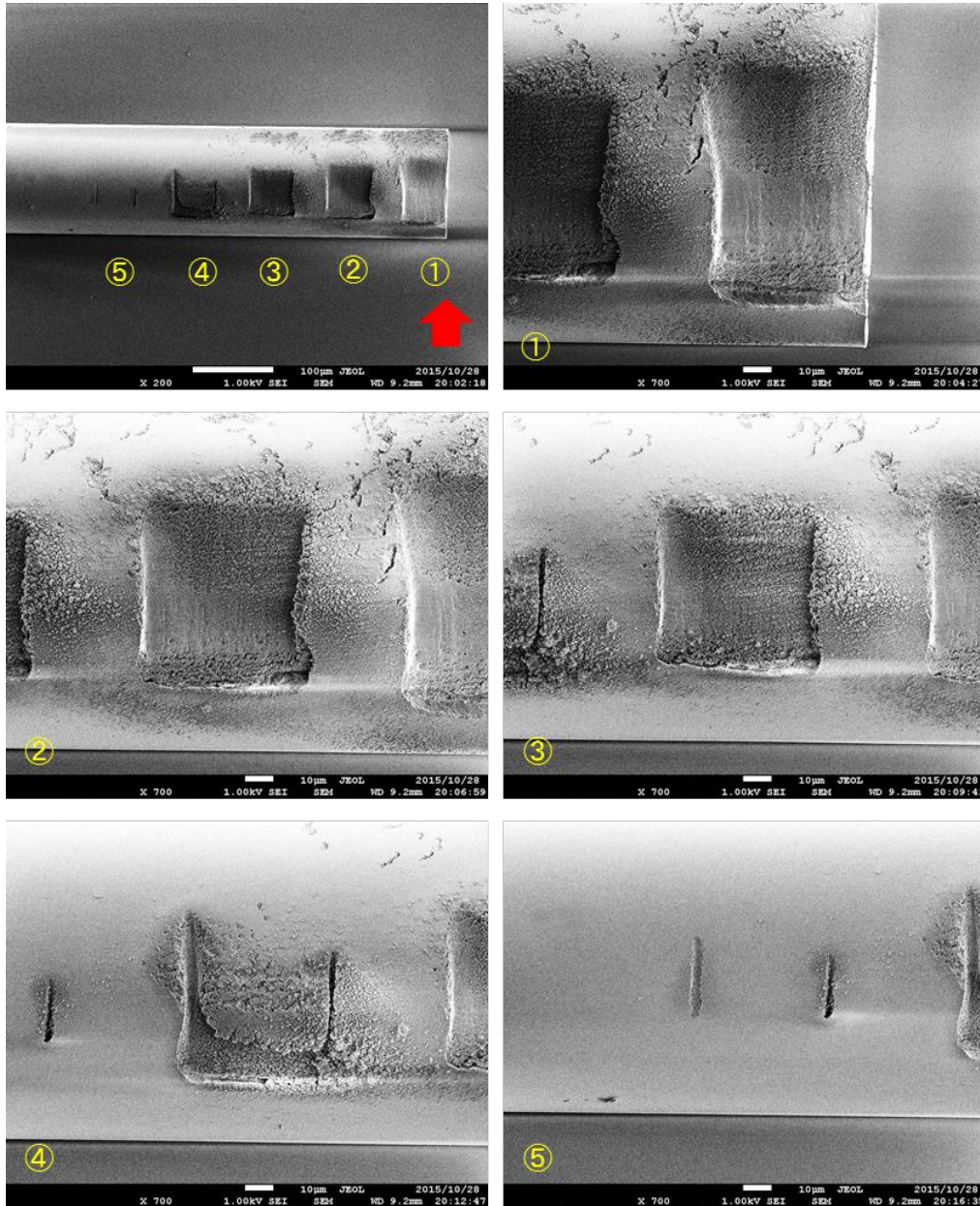
Figure 6.10: Processed in air, NA = 0.42, pulse energy: 1) 34.7 [broken], 2) 18.1, 3) 9.3, 4) 4.5, and 5) 1.5 mW, respectively. The red arrow indicates the direction of the fs-laser.
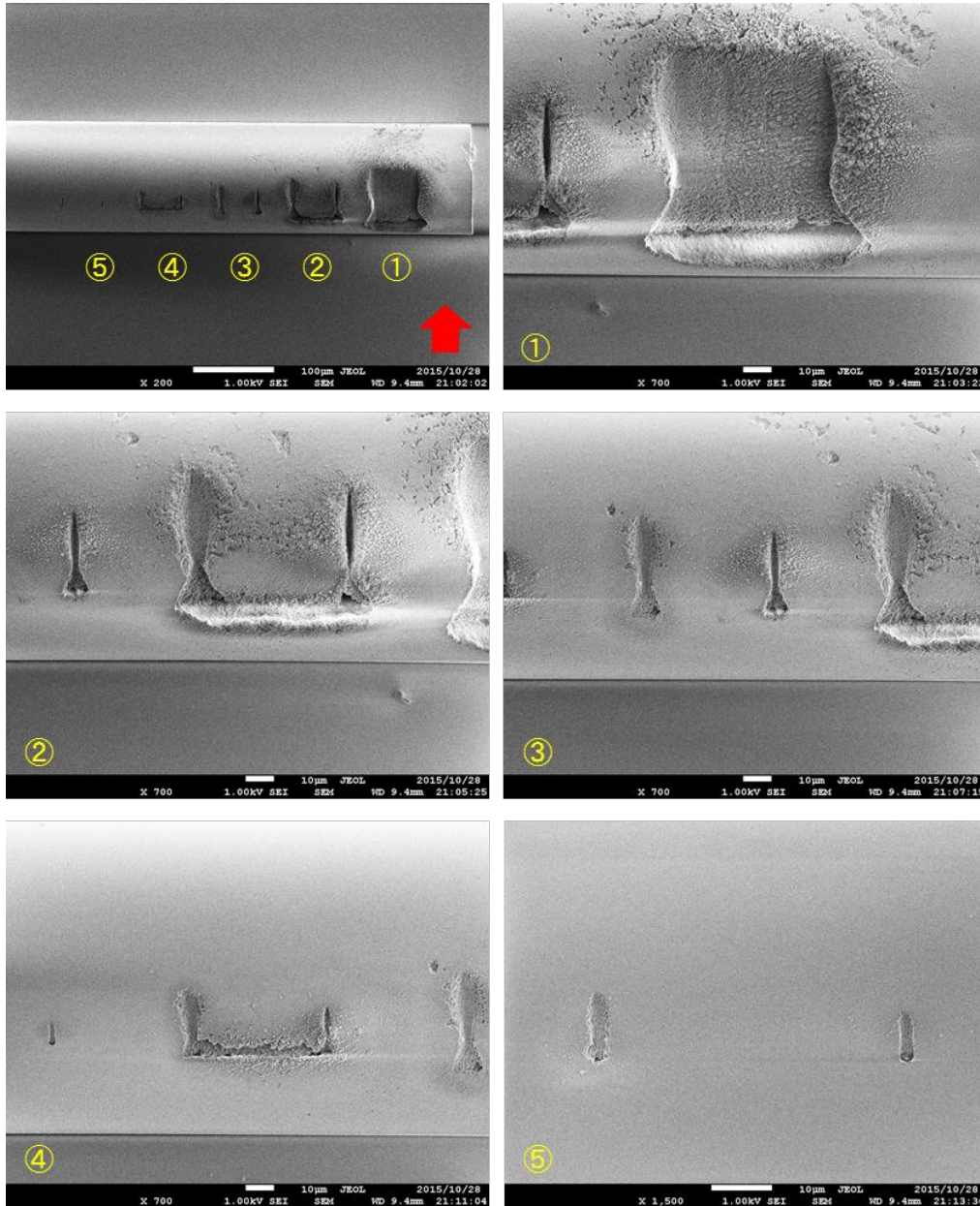
Figure 6.11: Processed in air, NA = 0.55, pulse energy: 1) 34.7, 2) 18.1, 3) 9.3, 4) 4.5, and

5) 1.5 mW, respectively. The red arrow indicates the direction of the fs-laser.
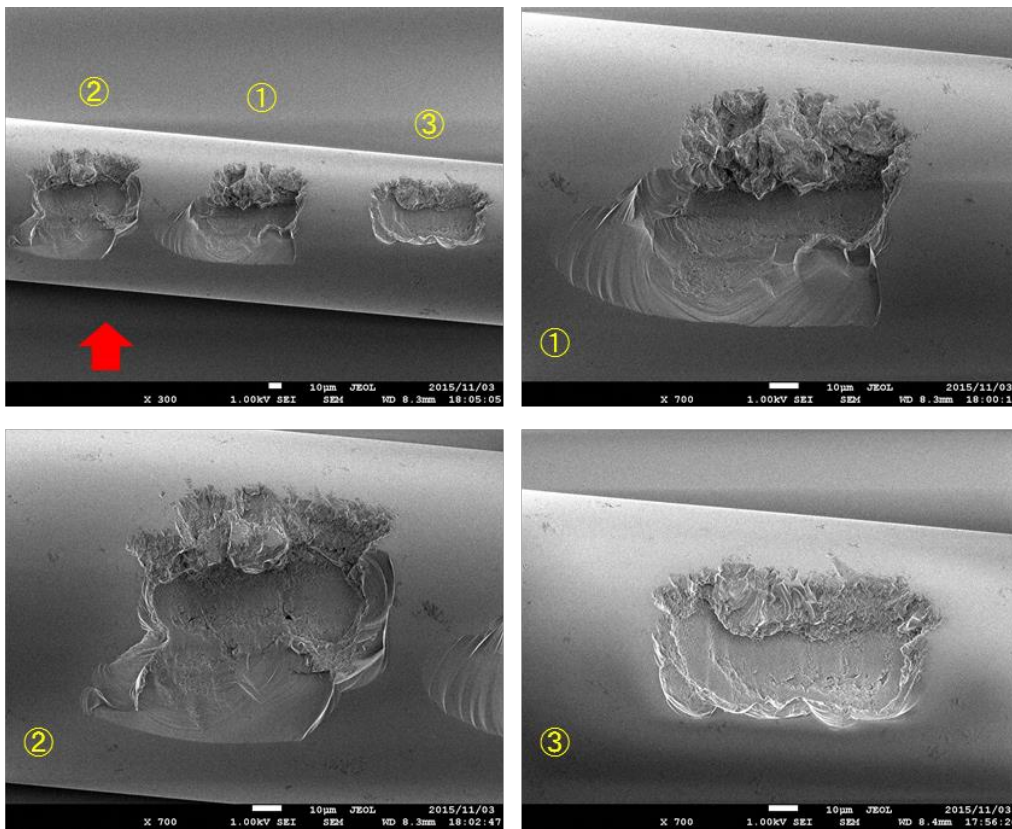
Figure 6.12: Processed in water, NA = 0.14, pulse energy: 1) 34.7, 2) 18.1, and 3) 9.3 mW, respectively. The red arrow indicates the direction of the fs-laser.
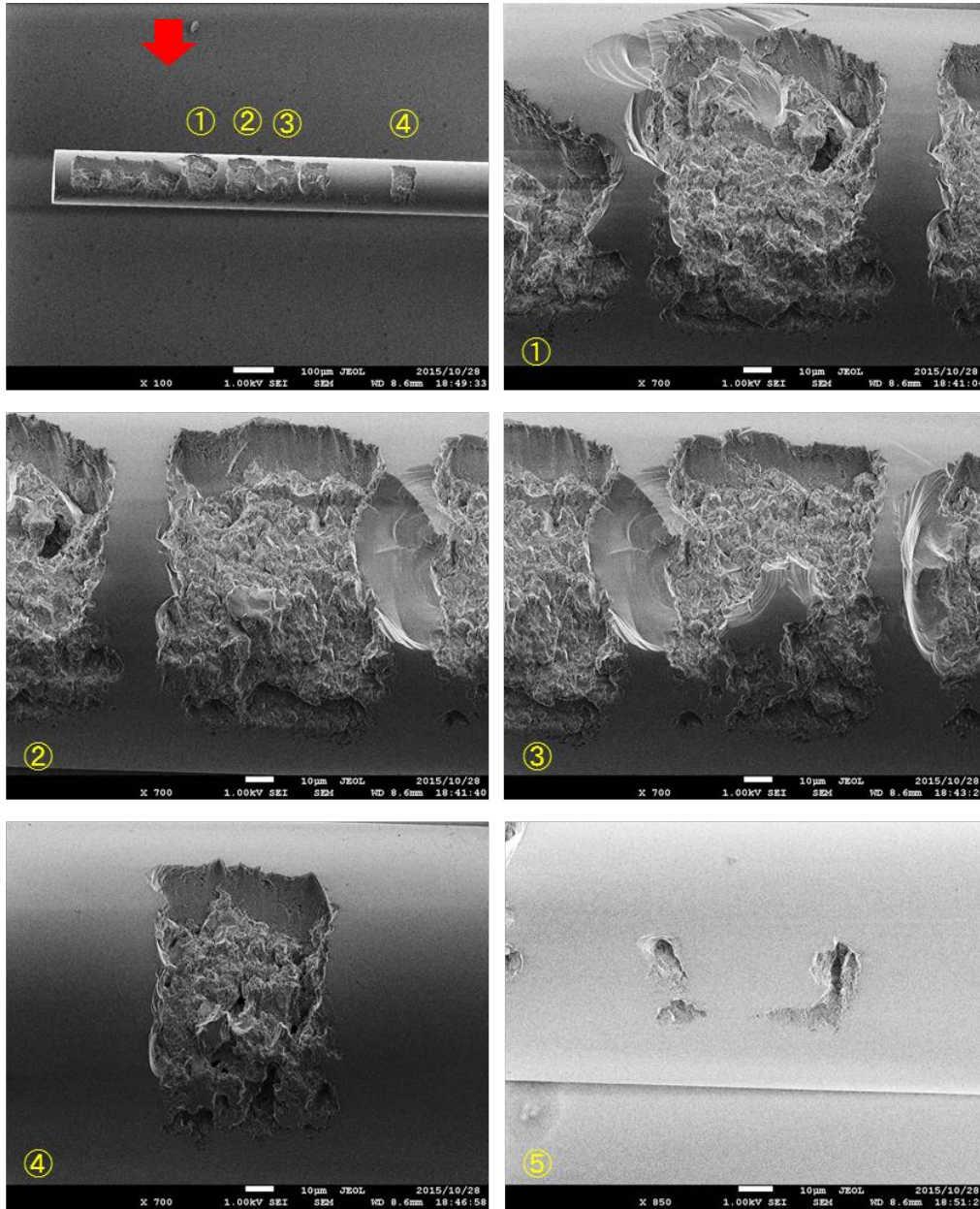
Figure 6.13: Processed in water, NA = 0.28, pulse energy: 1) 34.7, 2) 18.1, 3) 9.3, 4) 4.5, and 5) 1.5 mW, respectively. The red arrow indicates the direction of the fs-laser.
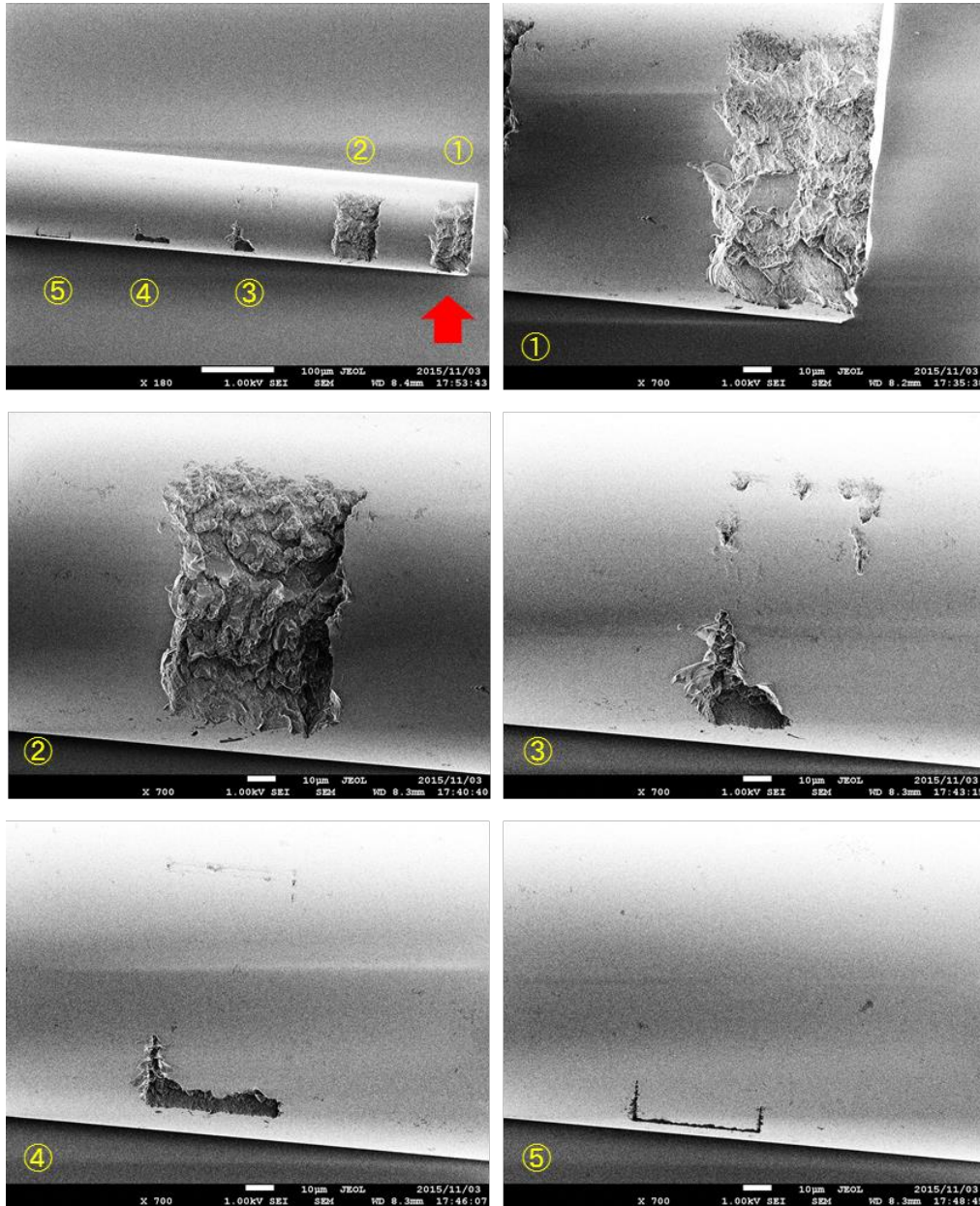
Figure 6.14: Processed in water, NA = 0.42, pulse energy: 1) 34.7, 2) 18.1, 3) 9.3, 4) 4.5, and 5) 1.5 mW, respectively. The red arrow indicates the direction of the fs-laser.
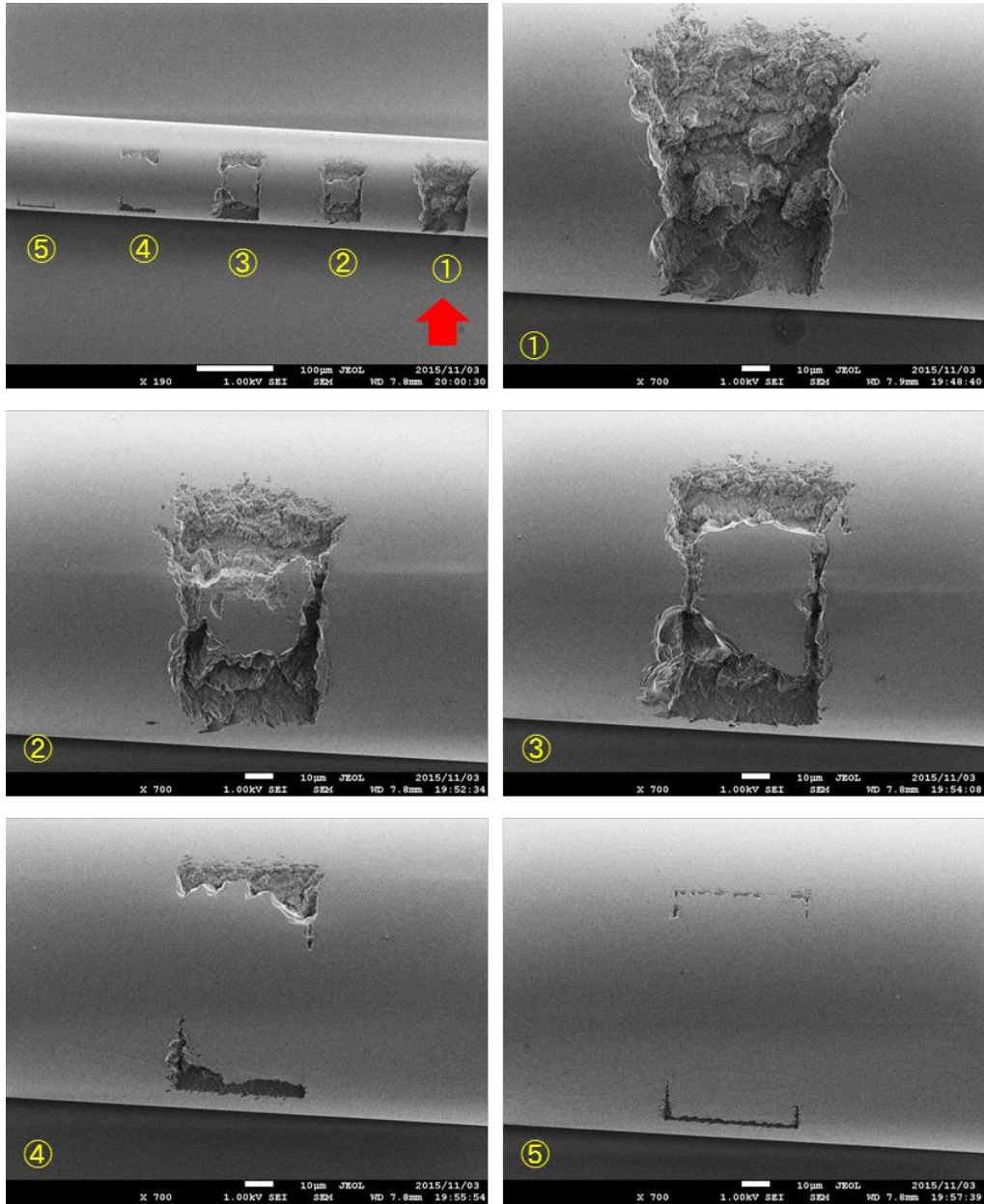
Figure 6.15: Processed in water, NA = 0.55, pulse energy: 1) 34.7, 2) 18.1, 3) 9.3, 4) 4.5, and 5) 1.5 mW, respectively. The red arrow indicates the direction of the fs-laser.
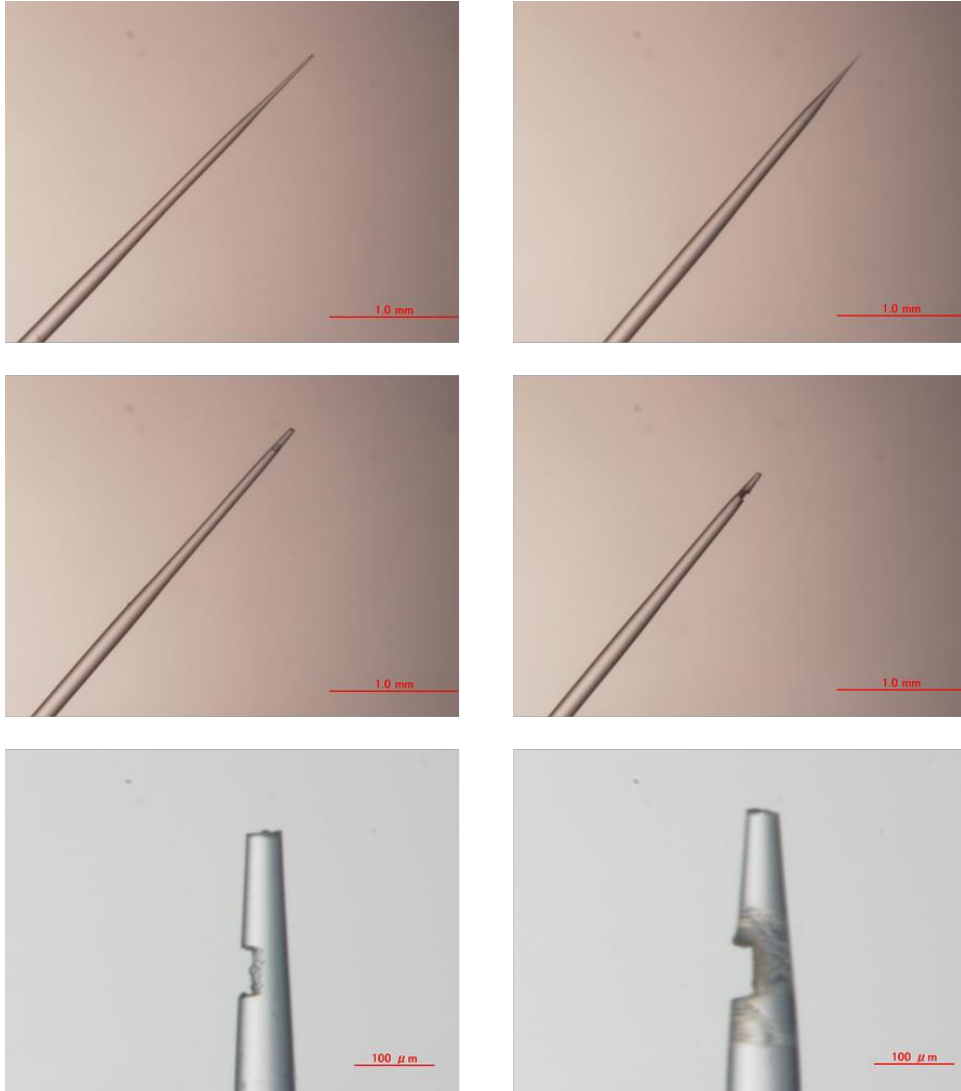
Figure 6.16: The Fs-TOPs of processed in water, NA = 0.55, pulse energy: 18.1 mW (left-hand-side column) and that of processed in air, NA = 0.28, pulse energy: 18.1 mW (right-hand-side column). The top, middle and bottom rows are before processing, after processing and magnified image of the groove.
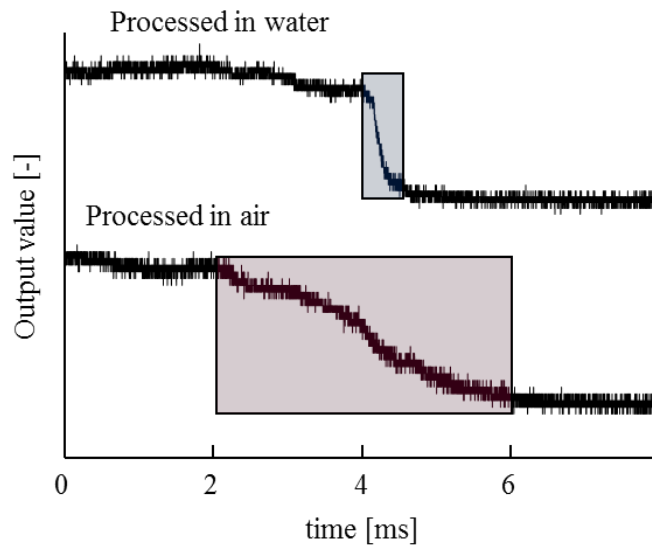
Figure 6.17: The signal of the sensor B of Fig. 6.16. The rectangle area is an uncertainty of

$\varDelta t_{s2}$.

7. Conclusion

In this thesis, I studied how the potentials of the optic signals of the single-tip optical fiber probe (S-TOP) could be brought out. From the signal-centric viewpoint, in the chapter 2, the output signal was deeply investigated theoretically, experimentally, and numerically. The phase detection principle was confirmed by the classic fashion, then it was applied to the S-TOP measurement. The qualitative discussion corresponded to the experimental results, however, more quantitative investigations were needed to analyze the S-TOP signal. According to the 3D raytracing simulator and various experiments, I found that the spike signal buried in the S-TOP signal was very informative "noise" to overcome the inevitable problems of the S-TOP measurement. Its important advantages were; i) its peak-time indicated a precise time of piercing the bubble/droplet and ii) its peak-intensity indicated piercing position on the bubble/droplet. These properties contributed to correct measurement for the size of the bubble/droplet, and were confirmed empirically in the chapter 3. Based on the results, the pre-signal threshold method was established for the S-TOP measurement in a bubbly flow. I extracted the signals which included the clear pre-signal above a threshold value, then the velocity and pierced length were calculated. Thus the signals when the S-TOP has touched the bubbles near their pole were extracted. I conducted the S-TOP measurement in the bubbly flow. By the application of the pre-signal threshold method, the S-TOP measurement was remarkably enhanced: the difference in the result of the axis-length measurement between the S-TOP and visualization decreased from 42% to 16%; and the

standard deviation also decreased from 0.8 mm to 0.04 mm. The residual uncertainty was categorized into the following types: type 1, deceleration of the bubble due to contact with the S-TOP; type 2, uncertainty owing to the bubble interface geometry; type 3, uncertainty owing to random touch positions restricted within an allowance of the pre-signal threshold method; type 4, uncertainty due to the randomness of the bubble motion. As for the droplet measurement, in the chapter 4, the post-signal threshold method was introduced. This method was also extracting the signals which included the clear post-signal above a threshold value, then the velocity and pierced length of the droplet were calculated. The velocity and size of the droplet could be measured with under 5% accuracy by using this method; however, the spatial limit of the S-TOP becomes remarkable in the measurements for tiny droplets (the droplets of few dozen micrometer in diameter).

Hence from the probe-centric viewpoint, the Fs-TOP was hopefully introduced, and fs-laser processing for optical fiber is studied in the chapter 5 for optimizing its processing. Bubble nucleation and growth following plasma channeling and white-light continuum in liquid irradiated by a single-shot fs-pulse were experimentally investigated with close observation of the time scale. Making full use of the new confocal system and time-resolved visualization techniques, I obtained evidence suggestive of a major/minor role of the non-linear/thermal effects during the fs-pulse-induced bubble's fountainhead (10^{-13} s) and growth (10^{-7} s), which was never observed with the use of the ns-pulse (i.e., optic cavitation). In this context, the fs-pulse-induced bubble was not ordinary optic cavitation but rather was nonlinear-optic cavitation. I presented the intrinsic differences in the dominant-time domain of the fs-pulse and ns-pulse excitation, and intriguingly, a mere hundred femtoseconds'

excitation predetermined the size of the bubble appearing several microseconds after irradiation. That is, the nucleation happened temporally beyond a six-order-of-magnitude difference.

At last, I used the results in a practical way, the different atmosphere for the Fs-TOP processing was examined in the chapter 6 because the nonlinear effect depended on the types of liquid. The filament length formed along the optic axis of the fs-laser was a depth for processing. According to the result of the chapter 5, the filament could be easily formed in water; hence I made the Fs-TOP in water. This practice served my purpose; the groove processed in water detected gas-liquid interface sensitively: the uncertainty of t_{s2} decision showed an 85% improvement compared to the previous Fs-TOP. There were many parameters including the processing atmosphere for making the Fs-TOP. More validations were still my due; however, my study provided enough evidence of effectiveness of the physical-mechanism-based optimization for bringing out the possibility of the S-TOP.

Appendix A: Biphasic method

A.1. Biphasic curve

"Biphasic method" is invented by Sakamoto to simplify the signal processing steps and assure the robustness and accuracy of the optical fiber probing. The main feature of the method is *biphasic-curve* fitting. This algorithm has been often applied in pharmacology, however, it also be applicable to fit the raw signal of optical fiber probing. The equation of a biphasic curve is a simple explicit formula,

$$V_{BP}(t) = \xi_2 + \frac{\xi_1 - \xi_2}{1 + \exp\{4g_{rd}(t - t_1)\}} + \frac{\xi_3 - \xi_2}{1 + \exp\{4g'_{rd}(t_2 - t)\}} \qquad \text{(A.1)}$$

where ξ_1 [-], ξ_2 [-], and ξ_3 [-] are normalized V_{Gas} [V] and V_{Liquid} [V] in the S-TOP signal; g_{rd} [/s] and g'_{rd} [-] are the gradients of upslope and downslope of the unitary signal; and t_1 [s] and t_2 [s] are midpoint of the slopes. Figure A.1 shows a sample biphasic curve for fitting a primary signal of a bubble and Figure A.2 of droplets. t_s is defined at the cross point of ξ_{Liquid} and the tangent at the inflection t_1-point,

$$t_e = t_2 - \frac{1}{2g'_{rd}} \qquad \text{(A.2)}$$

119

$$t_s = t_1 - \frac{1}{2g_{rd}}$$
(A.3)
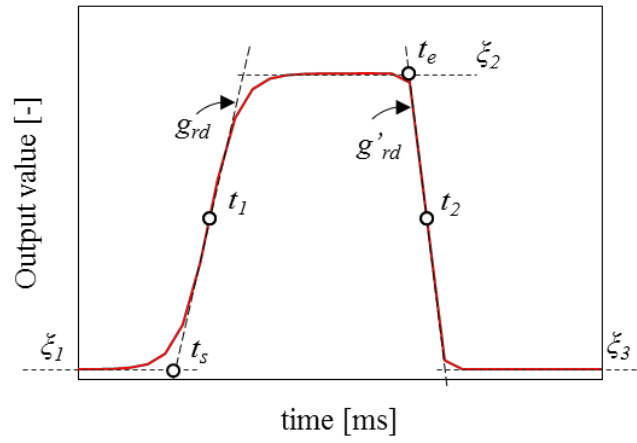
Figure. A.1: Biphasic curve for fitting a bubble primary signal
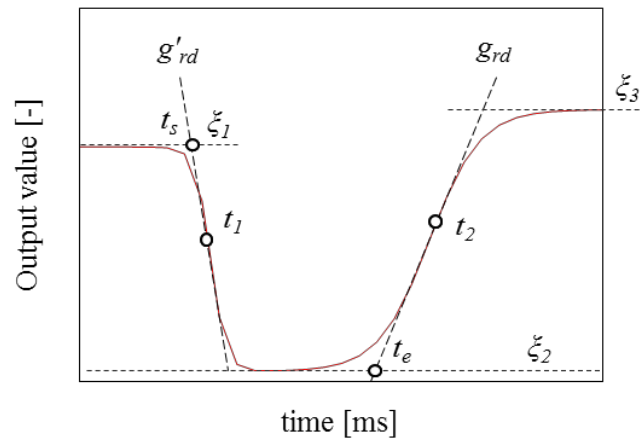
Figure A.2: Biphasic curves for fitting droplet primary signals

A.2. Signal processing procedure in biphasic method

Figure A.3 describes the biphasic method for signal processing of optical fiber probing. At first, the initial coefficients of a biphasic curve (ξ_1, ξ_2, ξ_3, g_{rd}, g'_{rd}, t_1, t_2) are set. At second, fitting calculation starts. In this step, an optimization algorithm minimizes the least-square error function:

$$E^2\left(\xi_1, \xi_2, \xi_3, g_{rd}, g'_{rd}, t_1, t_2\right) = \sum_t \left(V_{BP} - V_{\text{Raw}}\right)^2 \tag{A.4}$$

where V_{BP} is the biphasic curve and V_{Raw} is the raw probing signal.

There are several algorithms to solve the 7-dimensional nonlinear optimization; e.g., Newton method, conjugate gradient method, steepest descent method, simulated annealing method, downhill simplex method, and so on. I implemented the downhill simplex method because it requires only function evaluations (not derivatives) and therefore it is considered to be the most simple and robust.
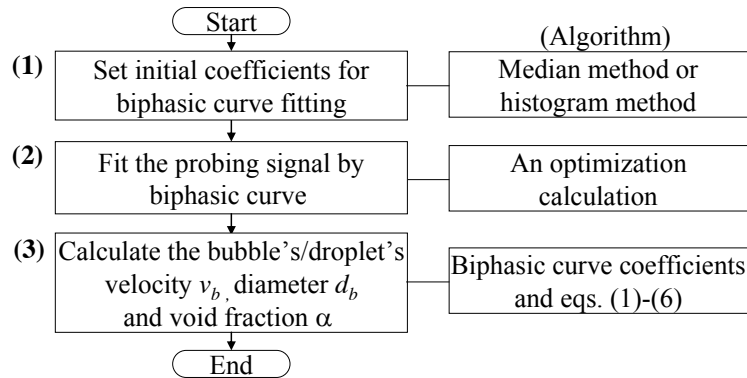
Figure A.3: Flowchart of the signal processing procedure based on biphasic method.

The biphasic method solves all problems of the conventional method,

(a) It does not require any smoothing procedures.

(b) It fits the whole a raw probing signal data by a biphasic curve. This feature is especially suitable for detecting the gradients g_{rd} and g'_{rd}. Because usual method fits only a few of signal data by a line.

(c) The biphasic curve's coefficients directly link to the bubble/droplet properties. The source code of the signal processing procedure is therefore simpler, more robust and more precise than the conventional method.

(d) Furthermore, spike signals will be detected easier from the difference of the raw probing signal and the fit biphasic curve (shown in Figure A.4). Various residual analysis enables to detect spike signals, noises, and genuine phase detection signal. This hopeful detection is very important for advanced measurement, therefore this advantage will improve the performance of optical fiber probing.
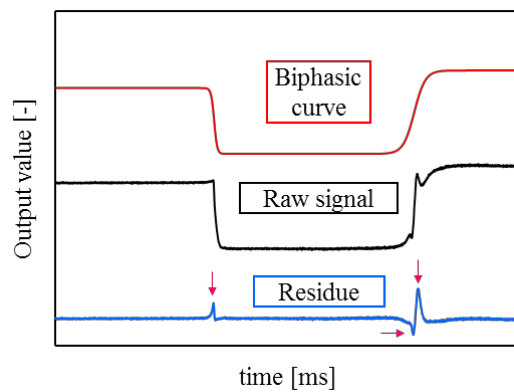
Figure A.4: Extraction primary signal and accessory signals by biphasic method.

Nomenclature of the optical fiber probe part

A	void fraction (-)
CL_{MC}	chord length of the S-TOP obtained by the Monte Carlo method (mm)
d_{RAY}	diameter defining area where the RAYs are introduced (mm)
d_{core}	diameter defining area of the fiber core (mm)
D_{eq}	volume-equivalent diameter (mm)
D	diameter of droplet (mm)
f	fiber core
g_{rd}	gradient from water to air in the S-TOP signals (s^{-1})
g'_{rd}	gradient from air to water in the S-TOP signals (s^{-1})
h	length from the S-TOP tip to the interface on the S-TOP tip surface (-)
H	length of the wedge (mm)
H'	length from the S-TOP tip to the interface on the S-TOP tip surface (mm)
i	incident angle (deg.)
i_{crit}	critical angle (deg.)
I	light energy of the beams returned from the S-TOP tip (-)
I_{gas}	light energy of the beams returned from the S-TOP positioned in gas phase (-)
I_{Liquid}	light energy of the beams returned from the S-TOP positioned in liquid phase (-)
I_{water}	light energy of the beams discharged into the water (-)
I_{spike}	light energy of the beams returned from the S-TOP detecting interface (-)
k	phase parameter, gas or liquid
l	the distance from probe A to B (mm)

L	pierced chord length (mm)
L^*	latency length (mm)
L_B	pierced chord length of bubble measurement (mm)
L_D	pierced chord length of droplet measurement (mm)
L_e	effective length (mm)
L_m	half length of the major axis of the bubble (mm)
L_{minor}	length of the minor axis of the bubble (mm)
L_{MC1}	distance from a bubble minor axis in the X-Z plane (mm)
L_{MC2}	distance from a bubble minor axis in the Y-Z plane (mm)
L_P	distance from the tip to groove of the Fs-TOP (mm)
L_{sensor}	geometrical size of the sensor area of the S-TOP (mm)
n	refractive index (-)
NA	numerical aperture (-)
r	refraction angle (deg.)
x	probe position (mm)
R	ratio of signal intensities from the probe, gas per liquid (-)
R_P	reflectivity of parallel polarization (-)
R_S	reflectivity of perpendicular polarization (-)
R_{tip}	diameter of the S-TOP tip (mm)
S	area covered by gas phase (mm^2)
t	time (s)
t_1	time at midpoint of g_{rd} (s)
t_2	time at midpoint of g'_{rd} (s)

t_s	time at which the S-TOP starts to touch the bubble/droplet surface (s)
t_{s2}	time at which the sensor B of the Fs-TOP detect the interface (s)
$t_{s,BP}$	t_s predicted by biphasic method (s)
$t_{s,pre}$	t_s predicted by pre-signal (s)
t_e	time at which the S-TOP is in contact with rear surface of the bubble/droplet (s)
$t_{e,pos}$	t_e predicted by post-signal (s)
T	time (s)
T_P	transmissivity of parallel polarization (-)
T_S	transmissivity of perpendicular polarization (-)
U_B	bubble velocity (m/s)
U_D	droplet velocity (m/s)
U_{int}	interface velocity in theory (m/s)
U'_{int}	interface velocity in experiment (m/s)
$\bar{U}_{int}$	averaged interface velocity (m/s)
V	output voltage of a photomultiplier (V)
V_{BP}	output value by biphasic method (-)
V_{Gas}	output level of the S-TOP positioned in gas phase (V)
V'_{Gas}	output level of the S-TOP positioned in gas phase (-)
V_{Liquid}	output level of the S-TOP positioned in liquid phase (V)
V'_{Liquid}	output level of the S-TOP positioned in liquid phase (-)
V_{pf}	calculated output voltage (-)
V_{pm}	experimentally obtained output voltage (-)

V_P normalized value of the pre-signal/post-signal (-)

V_{Pmax} output value of the pre-signal (-)

V_{Pth} threshold value for the pre-signal/post-signal threshold method (-)

z interface position (mm)

α theoretical proportionality coefficient (mm V^{-1})

α'_k proportionality coefficient in experiment (mm)

β proportionality coefficient (V)

$\Delta_{S\text{-}TOP}$ the distance between the bubble's/droplet's pole and the S-TOP (mm)

Δt_{s2} allowance of t_{s2} detection (s)

ϕ impact angle of the local interface (deg.)

Φ impact angle of the interface in y-z axis (deg.)

ξ_{Gas} normalized output voltage of V_{Gas} for biphasic method in bubble signal (-)

ξ_{Gas1} normalized output voltage used for biphasic method in droplet signal (-)

ξ_{Gas2} normalized output voltage used for biphasic method in droplet signal (-)

ξ_{Liquid} normalized output voltage of V_{Liquid} (-)for biphasic method in droplet signal (-)

$\xi_{Liquid1}$ normalized output voltage used for biphasic method in bubble signal (-)

$\xi_{Liquid2}$ normalized output voltage used for biphasic method in bubble signal (-)

θ fixed angle of the S-TOP (deg.)

θ_{cone} angle of the cone tip (deg.)

θ_{MC1} piercing angle in the X-Z plane (degree)

θ_{MC2} piercing angle in the Y-Z plane (degree)

θ_t refracting angle (deg.)

θ_i incident angle (deg.)

θ_{RAY} angle at which the RAYs are introduced (deg.)

θ_w wedge-angle of the S-TOP (deg.)

Θ impact angle of the interface in x-z axis (deg.)

τ the difference in the detection time of probe A and B (s)

τ_{probe} actual dwelling time of the probe in a droplet (s)

τ_{camera} predicted τ_{probe} by captured images (s)

Ψ phase indicator (-)

References

◆ **Optical fiber probe part**

1. M. Sommerfeld and H.H. Qiu, *Int. J. Multiph. Flow* **19** 1093-1127 (1993).

2. C.F. Hess, *9th. Int. Symp. Applications of Laser Techniques to Fluid Mechanics, Lisbon-Portugal* 18.1 (1998).

3. T. Kawaguchi, Y. Akasaka, and M. Maeda *Meas. Sci. Technol.* **13** 308-316 (2002).

4. G.P. Nassos, *Rep. ANL-6738* (1963).

5. V.W. Goldsmith, *J. Colloid Sci.* **20** 617-635 (1965).

6. N. Miller and R.E. Mitchie, *J. Brit. Nucl. Energy Soc.* **2** 94 (1970).

7. N. Abuaf, O.C. Jones Jr, and A. Zimmer, *Rev. Sci. Instrum.* **49** 1090-1094 (1978).

8. L. Aprin, P. Mercier, and L. Tadrist, *Int. J. Multiph. Flow* **33** 371-393 (2007).

9. E. Barrau, N, Riviere, C. Poupot, and A. Cartellier, *Int. J. Multiph. Flow* **25** 229-256 (1999).

10. W.K. Harteveld, *PhD thesis of TU Delft* (2005)

11. M. Higuchi and T. Saito, *Chem. Eng. J.* **160** 284-292 (2010).

12. J. Vejražka, M. Večeř, S. Orvalho, P. Sechet, M.C. Ruzicka, and A. Cartellier, *Int. J. Multiph. Flow* **36** 533-54 (2010).

13. J. Xue, *PhD thesis of Washington University* (2004).

14. T. Saito, *Japanese Patent* No. 3,018,178 (2000).

15. R.F. Mudde and T. Saito *J. Fluid Mech.* **437** 203-228 (2001).

16. T. Saito and R.F. Mudde, *Proc. Int. Conf. on Multiphase Flow 2001* Paper no. 111, in CD-ROM (2001).

17. T. Saito, Y. Ishigaki, and Y. Mizuno, *Proc. Int. Conf. on Multiphase Flow 2004* Paper no. 113, in CD-ROM (2004).

18. K. Hanyu and T. Saito, *Canad. J. Chem. Eng.* **88** 551-560 (2010).

128

19. T. Saito, K. Matsuda, Y. Ozawa, S. Oishi, and S. Aoshima, *Measure. Sci. Tech.* **20** 114,002 (2009).

20. Y. Mizushima and T. Saito, *Meas. Sci. Technol.* **23** 085308 (2012).

21. Y. Mizushima and T. Saito, *Chem. Eng. Trans.* **32** 1513-1518 (2013).

22. Y. Mizushima, A. Sakamoto, and T. Saito, *Chem. Eng. Sci.* **100** 98-104 (2013).

23. M. Yamada and T. Saito, *Flow Meas. Instrum.* **27** 8-19 (2012).

24. N.N. Clark and R. Turton, *Int. J. Multiph. Flow* **14** 413-424 (1988).

25. N.N. Clark, W. Liu, and R. Turton, *Powder Technol.* **88** 179-188 (1996).

26. A. Cartellier, *Rev. Sci. Instrum.* **63** 5442-5452 (1992).

27. A. Cartellier and E. Barrau, *Int. J. Multiph. Flow* **24** 1265-1294 (1998).

28. A. Cartellier and E. Barrau *Int. J. Multiph. Flow* **24** 1295-1315 (1998).

29. A. Cartellier, *Rev. Sci. Instrum.* **62** 279-303 (1991).

30. F. Danel and J. M. Delhaye, *Mesures, Regulation, Automatismes* **36** 99 (1971).

31. Ph. Graindorge, G. Le Boudec, D. Meyet, and H.J. Arditty, *Proc. SPIE, Int. Soc. Opt. Eng.* **586** 211 (1985).

32. D. Morris, A. Teyssedou, J. Lapierre, and A. Tapucu, Appl. Opt. **26** 4660 (1987).

33. A. Cartellier, *Rev. Sci. Instrum.* **61** 874-886 (1990).

34. A. Sakamoto and T. Saito, *Proc. 15th Int. Symp. on Appl. Laser Techniques to Fluid Mechanics* Paper no. 4.6.5 (2010).

35. A. Sakamoto and T. Saito *Int. J. Multiph. Flow* **41** 77-90 (2011).

36. A. Sakamoto and T. Saito, *Rev. Sci. Instrum.* **83** 075107 (2012).

37. A. Sakamoto, *PhD thesis of Shizuoka University* (2012).

38. S. Hinata, *Bull. JSME* **15** 1228-1235 (1972).

39. A. Schmitt, K. Hoffmann, and R. Loth, *Rev. Sci. Instrum.* **66** 5045-5049 (1995).

40. J. Vejražka, M. Večeř, S. Orvalho, P. Sechet, M.C. Ruzicka, and A. Cartellier, *Int. J. Multiph. Flow* **36** 533-548 (2010).

41. Y. Miyamoto and T. Saito, *Trans. Japan Soc. Mech. Eng.* B **71** 1307–1313 (in Japanese) (2005).

42. D. Sone, K. Sakakibara, M. Yamada, T. Sanada, and T. Saito, *J. Power and Energy Systems* **2** 306-317 (2008).

43. T. Saito, K. Sakakibara, Y. Miyamoto, and M. Yamada, *Chem. Eng. J.* **158** 39-50 (2010).

44. Y. Nagami and T. Saito, *Flow Turbulence Combust.* **92** 147-174 (2014).

45. T. Saito and M. Toriu, *Chem. Eng. J.* **265** 164-175 (2015).

46. J. Huang and T. Saito, *Chem. Eng. Tech.* **38** 1947-1954 (2015).

47. M. Andreotti, *Ph.D. Thesis, Institut National Polytechnique de Grenoble* (2009).

48. D. Bhaga and M.E. Weber, *J. Fluid Mech.* **105** 61-85 (1981).

49. M. Hong, A. Cartellier, and E.J. Hopfinger, *Int. J. Multiph. Flow* **30** 615-648 (2004).

◆ Femtosecond pulse laser part

50. B. N. Chichkov, C. Momma, S. Nolte, F. von Alvensleben, and A. Tunnermann, *Appl. Phys. A* **63**, 109 (1996).

51. S. Nolte, C. Momma, H. Jacobs, A. Tunnermann, B. N. Chichkov, B. Wellegehausen, and H. Welling, *J. Opt. Soc. Am. B* **14**, 2716 (1997).

52. T. Brabec and F. Krausz, *Rev. Mod. Phys.* **72**, 545 (2000).

53. N. M. Bulgakova, R. Stoian, A. Rosenfeld, I. V. Hertel, and E. E. B. Campbell, *Phys. Rev. B* **69**, 054102 (2004).

54. A. De Giacomoa, M. Dell'Aglioa, F. Colaob, and R. Fantoni, *Spectrochim. Acta B* **59**, 1431 (2004).

55. U. Saalmann, C. Siedschlag, and J. M. Rost, *J. Phys. B* **39**, R39 (2006).

56. A. Y. Vorobyev and C. L. Guo, *Laser Photon. Rev.* **7**, 385 (2013).

57. M.V. Allmen, Laser-beam Interactions with Materials (Springer-Verlag, New York 1987).

58. B. C. Stuart, M. D. Feit, A. M. Rubenchik, B. W. Shore, and M. D. Perry, *Phys. Rev. Lett.* **74**, 2248 (1995).

59. M. Lenzner, J. Kruger, S. Sartania, Z. Cheng, C. Spielmann, G. Mourou, W. Kautek, and F. Krausz, *Phys. Rev. Lett.* **80**, 4076 (1998).

60. R. E. Russo, X. L. Mao, H. C. Liu, J. Gonzalez, and S. S. Mao, *TALANTA* **57**, 425 (2002).

61. Q. Lu, S. S. Mao, X. Mao, and R. E. Russo, *Appl. Phys. Lett.* **80**, 3072 (2002).

62. S. S. Mao, F. Quere, S. Guizard, X. Mao, R. E. Russo, G. Petite, and P. Martin, *Appl. Phys. A* **79**, 1695 (2004).

63. X. Zeng, X. L. Mao, R. Greif, and R. E. Russo, *Appl. Phys.* A **80**, 237 (2005).

64. S. J. Pearton, D. P. Norton, K. Ip, Y. W. Heo, and T. Steiner, Prog. *Mater. Sci.* **50**, 293 (2005).

65. U. Ozgur, Y. I. Alivov, C. Liu, A. Teke, M. A. Reshchikov, S. Dogan, V. Avrutin, S. J. Cho, and H. Morkoc, *J. Appl. Phys.* **98**, 041301 (2005).

66. L. Berge, S. Skupin, R. Nuter, J. Kasparian, and J. P. Wolf, *Rep. Prog. Phys.* **70**, 1663 (2007).

67. A. Kirilyuk, A. V. Kimel, and T. Rasing, *Rev. Mod. Phys.* **82**, 2731 (2010).

68. F. Chen, and J. R. V. de Aldana, *Laser Photon. Rev.* **8**, 251 (2014).

69. S. L. Trokel, R. Srinivasan, and B. Braren, *Am. J. Ophthalmol.* **96**, 710-5 (1983).

70. R. Srinivasan, *Science* **234**, 559 (1986).

71. M. R. EmmertBuck, R. F. Bonner, P. D. Smith, R. F. Chuaqui, Z. P. Zhuang, S. R. Goldstein, R. A. Weiss, and L. A. Liotta, *Science* **274**, 998 (1996).

72. K. Konig, I. Riemann, P. Fischer, and K. H. Halbhuber, *Cell. Mol. Biol.* **45**, 195 (1999)

73. A. Vogel and V. Venugopalan, *Chem. Rev.* **103**, 577 (2003).

74. M. Wojtkowski, V. J. Srinivasan, T. H. Ko, J. G. Fujimoto, A. Kowalczyk, and J. S. Duker, *Opt. Express* **12**, 2404 (2004).

75. C. P. Cain, R. J. Thomas, G. D. Noojin, D. J. Stolarski, P. K. Kennedy, G. D. Buffington, and B. A. Rockwell, *Graefe's Arch. Clin. Exp. Ophthalmol.* **243**, 101 (2005).

76. C. L. Arnold, A. Heisterkamp, W. Ertmer, and H. Lubatschowski, *Opt. Express* **15**, 10303 (2007).

77. D. Kobat, M. E. Durst, N. Nishimura, A. W. Wong, C. B. Schaffer, and C. Xu, *Opt. Express* **17**, 13354 (2009).

78. A. Trost, F. Schroedl, C. A. Strohmaier, B. Bogner, C. Runge, A. Kaser-Eichberger, K. A. Krefft, A. Vogel, N. Linz, S. Freidank, A. Hilpert, I. Zimmermann, G. Grabner, and H. A. Reitsamer, *Invest. Ophthalmol. Vis. Sci.* **54**, 7854 (2013).

79. Y. Miyamoto, A. Rubio, and D. Tomanek, *Phys, Rev. Lett.* **97**, 126104 (2006).

80. K. Ishioka, M. Hase, M. Kitajima, L. Wirtz, A. Rubio, and H. Petek, *Phys. Rev. Lett.* **77**, 121402 (2008).

81. Y. Miyamoto, H. Zhang, and D. Tománek, *Phys. Rev. Lett.* **104**, 208302 (2010).

82. F. Carbone, G. Aubock, A. Cannizzo, F. Van Mourik, R. R. Nair, A. K. Geim, K. S. Novoselov, and M. Chergui, *Chem. Phys. Lett.* **504**, 37 (2011).

83. P. Russo, A. M. Hu, G. Compagnini, W. W. Duley, and N. Y. Zhou, *Nanoscale* **6**, 2381 (2014).

84. M. Reininghaus, C. Kalupka, O. Faley, T. Holtum, J. Finger, and C. Stampfer, *Appl. Phys. A* **117**, 1873 (2014).

85. Y. Miyamoto, H. Zhang, T. Miyazaki, and A. Rubio, *Phys. Rev. Lett.* **114**, 116102 (2015).

86. W. Lauterborn, *Acustica* **31**, 51 (1974).

87. Y. Tomita and A. Shima, *Acustica* **71**, 161 (1990).

88. P. K. Kennedy, *IEEE J. Quant. Electron.* **31**, 2241 (1995).

89. P. K. Kennedy, S. A. Boppart, D. X. Hammer, B. A. Rockwell, G. D. Noojin, and W. P. Roach, *IEEE J. Quant. Electron.* **31**, 2250 (1995).

90. D. X. Hammer, R. J. Thomas, G. D. Noojin, B. A. Rockwell, P. K. Kennedy, and W. P. Roach, *IEEE J. Quant. Electron.* **32**, 670 (1996).

91. C. D. Ohl, O. Lindau, and W. Lauterborn, *Phys. Rev. Lett.* **80**, 393 (1998).

92. O. Baghdassarian, B. Tabbert, and G. A. Williams, *Phys. Rev. Lett.* **83**, 2437 (1999).

93. E. Abraham, K. Minoshima, and H. Matsumoto, *Opt. Commun.* **176**, 441 (2000).

94. B. Wolfrum, T. Kurz, O. Lindau, and W. Lauterborn, *Phys. Rev. E* **64**, 046306 (2001).

95. I. Akhatov, O. Lindau, A. Topolnikov, R. Mettin, N. Vakhitova, and W. Lauterborn, Phys. Fluids 13, 2805 (2001).

96. C. B. Schaffer, N. Nishimura, E. N. Glezer, A. Kim, and E. Mazur, *Opt. Express* 10, 196 (2002).

97. C. D. Ohl, *Phys. Fluids* **14**, 2700 (2002).

98. R. Geisler, Untersuchungen zur laserinduzierten Kavitation mit Nanosekunden- und Femtosekundenlasern (Universitätsverlag Göttingen, Göttingen, 2004).

99. K. Tsiglifis and N. A. Pelekasis, *Phys. Fluids* 17, 102101 (2005).

100. A. Vogel, J. Noack, G. Hüttman, and G. Paltauf, *Appl. Phys. B* **81**, 1015 (2005)

101. T. Kurz, D. Kröninger, R. Geisler, and W. Lauterborn, *Phys. Rev. E* **74**, 066307 (2006).

102. K. Tsiglifis and N. A. Pelekasis, *Ultrason. Sonochem.* **14**, 456 (2007).

103. A. De Giacomo, M. Dell'Aglio, O. De Pascale, and M. Capitelli, *Spectrochim. Acta B* **62**, 721

(2007).

104. A. Vogel, N. Linz, S. Freidank, and G. Paltauf, *Phys. Rev. Lett.* **100**, 038102 (2008).

105. K. Franjic, Studies of laser ablation of liquid water under conditions of impulsive heat deposition through vibrational excitations (IHDVE) (University of Toronto, 2010).

106. D. Faccio, G. Tamošauskas, E. Rubino, J. Darginavičius, D. G. Papazoglou, S. Tzortzakis, A. Couairon, and A. Dubietis, *Phys. Rev. E* **86**, 036304 (2012).

107. W. Lauterborn and A. Vogel, Shock wave emission by laser generated bubbles, Bubble Dynamics & Shock Waves (Springer, Berlin, 2013).

108. A. Han, K. Köhler, K. Jungnickel, R. Mettin, W. Lauterborn, and A. Vogel, *J. Fluid Mech.* **771**, 706 (2015).

109. R. R. Alfano and S. L. Shapiro, *Phys. Rev. Lett.* **24**, 592 (1970).

110. R. R. Alfano, The Supercontinuum Laser Source (Springer-Verlag, New York, 1989).

111. A. H. Reitze, H. Ahn, and M. C. Downer, *Phys. Rev. B* **45**, 2677 (1992).

112. J. C. Diels and W. Rudolph, Ultrashort Laser Pulse Phenomena (Academic, New York, 1996).

113. Q. Feng, J. V. Moloney, A. C. Newell, E. M. Wright, K. Cook, P. K. Kennedy, D. X. Hammer, B. A. Rockwell, and C. R. Thompson, *IEEE J. Quant. Electron.* **33**, 127 (1997).

114. A. Brodeur and S. L. Chin, *J. Opt. Soc. Am. B* **16**, 637 (1999).

115. G. S. He, L. S. Tan, Q. Zheng, and P. N. Prasad, *Chem. Rev.* **108**, 1245 (2008).

116. W. Liu, O. Kosareva, I. S. Golubtsov, A. Iwasaki, A. Becker, V. P. Kandidov, and S. L. Chin, *Appl. Phys. B* **75**, 595 (2002).

117. W. Liu, S. Petit, A. Beckera, N. Aközbekb, C. M. Bowdenb, and S. L. Chin, *Opt. Commun.* **202**, 189 (2002).

118. W. Liu, O. Kosareva, I. S. Golubtsov, A. Iwasaki, A. Becker, V. P. Kandidov, and S. L. Chin, *Appl. Phys. B* **76**, 215 (2003).

119. C. P. Hauri, W. Kornelis, F. W. Helbing, A. Heinrich, A. Couairon, A. Mysyrowicz, J. Biegert, and U. Keller, *Appl. Phys. B* **79**, 673 (2004).

120. C. D'Amico, A. Houard, M. Franco, B. Prade, A. Mysyrowicz, A. Couairon, and V. T. Tikhonchuk, *Phys. Rev. Lett.* **98**, 235002 (2007).

121. A. Couairon and A. Mysyrowics, *Phys. Rep.* **441**, 47 (2007).

122. Y. H. Chen, S. Varma, T. M. Antonsen, and H. M. Milchberg, *Phys. Rev. Lett.* **105**, 215005 (2010).

123. M. D. Feit and J. A. Fleck Jr., *Appl. Phys. Lett.* **24**, 169 (1974).

124. A. Ambrose, C. H. S. Sprake, and R. Townsend, *J. Chem. Thermodyn.* **6**, 693 (1974).

125. D. R. Stull, *Ind. Eng. Chem.* **39**, 517 (1947).

126. C. T. Liu and W. T. Lindsay Jr., *J. Chem. Eng. Data* **15**, 510 (1970).

127. C-B Kim and C. B. Su, *Meas. Sci. Technol.* **15**, 1683 (2004).

128. J. D. Koch, J. Gronki, and R. K. Hanson, *J. Quant. Spectrosc. Radiat. Transfer* **109**, 2037 (2008).

129. V. Feigenbrugel, C. Loew, S. Le Calvé, and P. Mirabel, *J. Photochem. Photobiol. A* **174**, 76 (2005).

130. A. Ikehata, M. Mitsuoka, Y. Morisawa, N. Kariyama, N. Higashi, and Y. Ozaki, *J. Phys. Chem. A* **114**, 8319 (2010).